Università degli Studi di Modena e Reggio Emilia

Dipartimento di Scienze Fisiche Informatiche e Matematiche
Physics and Nanosciences - School of Graduate Studies

III-V SEMICONDUCTOR NANOSTRUCTURES FOR MICROWAVE DETECTION

Tutor:

Prof. Marco Affronte

PhD candidate:

Samuele Cornia

Co-Tutor:

Dr. Alberto Ghirri

School Coordinator:

Prof. Marco Affronte

Cycle XXXIV

ABSTRACT

The detection of microwave (MW) radiation is essential for a wide range of applications, such as telecommunication, cosmology and quantum technologies. In certain regimes, no prevailing technology for the detection of this radiation has clearly emerged yet, although different solutions have been tested in different contexts.

As an example, the Square Kilometre Array is a large scale international project for the construction of a next generation radio telescope. [1] It will provide continuous coverage in the 50 MHz-13.8 GHz frequency range and comprise of $\sim$ 100 000 antennas in two continents. The massive scale of this infrastructure requires low cost, scalable, efficient and broadband detectors.

In the field of quantum technologies, microwave radiation plays a fundamental role in the manipulation and coupling of qbits. [2] The implementation of single photon detectors could push the field to new extremes. But the realization of a detector that works continuously, is fast, low noise and with high efficiency is still an open problem. This is due to the small energy quanta of MW radiation $\hbar\omega$, which is $10^4 - 10^5$ times smaller than its optical counterpart, for which high efficiency single photon detectors already exist.

The regimes of operation in these two applications greatly differ: quantum devices involving microwave radiation are typically operated at few mK temperature in shielded, low noise, cryogenic environments. The Square Kilometre Array employs ground based telescopes and is affected by background radiation such as the cosmic background radiation and other sources. Evidently, these applications require drastically different solutions to the same fundamental problem: the detection of microwave radiation.

This thesis focuses on the experimental study of III-V nanowire (NW) based devices as detectors in the 1-10 GHz range. These devices consist of both bare and heterostructured NWs; the latter were used in order to define Quantum Dots (QD) and Double Quantum Dots (DQD). On a fundamental level, the interplay of radiation with these systems depends drastically on type of nanostructure considered, with different effects that can take place. Classical MW radiation can lead to electrical phenomena, such as modulation of carrier density, but also to a distinct set of effects due to MW induced heating. This is most evident in bare NWs, where several mechanisms of interaction can lead to an ac to dc rectification. Since these phenomena leads to similar effects, their distinction is extremely challenging. In quantum system the interplay of the discrete energy states with either classical radiation or individual MW photons might lead to radically different effects. In this systems MW radiation is of particular interest since the

photon energies (40 μeV at 10 GHz, equivalent to a thermal energy of $\sim$ 0.5 K) are comparable to the typical energy scales of quantum devices (μeV to meV).

The following chapters describe the work I performed, consisting of the whole fabrication and characterization process: from the device design to the data analysis. The device fabrication began with the choice of the most suitable NW batch, as grown at the NEST laboratories in Pisa. Depending on the device design, different configuration of substrates and patters were realized by optical lithography. In this step most of the $\mu m - mm$ sized components were defined: DC contacts, superconducting resonators and microstrips. The final step of the fabrication process was the integration of the NWs by electron beam lithography. The electrical characterization of the devices was carried out either at room temperature in a probe station, or at low temperatures (0.3-300 K) in two cryostats that I wired for low level, low noise DC magneto-transport measurements and microwave spectroscopy. Finally, the measurement data were acquired using the Python framework QCoDeS and their analysis performed with Igor Pro. Out of a total of 367 NW devices, $\sim$200 were fabricated by me in Modena and $\sim$160 in Pisa. Of the $\sim$ 300 which were successfully fabricated, about 150 worked properly, with a success rate that increased in time as a results of improvements in the fabrication process.

The results section is split in three parts. In part one I shall present the potential application of NW Field Effect Transistors (FET) as detectors of MW radiation, in a regime where the classical rectification doesn't work because of the intrinsic cut-off frequency in the device response. The impact on the detection efficiency of different parameters (such as gate voltage, temperature and microwave frequency) is investigated and the detection mechanism discussed. These detector show good performance and stable operation in a wide temperature range (20-300 K) with two detection modes: measuring current or voltage response. In part two, I present the effect of MW radiation on a QD.[3] This was obtained starting from a InAs NWs, in which two InP layers were epitaxially defined along the axial direction during the growth process. These two materials have different band gaps and the right band alignment to provide robust electron confinement and, therefore, well-defined quantum dots. The microwave radiation is in this case fed to the system though a superconducting (YBCO) coplanar microwave resonator which enhances the electric field in the proximity of the device, providing a "focusing" effect. This greatly enhances the coupling of the MW radiation to the QD, at the cost restricting the device use to a single frequency.

Finally, in part three, the impact of microwave radiation in the 1-10 GHz range on the transport features of a DQD is presented. Zero and finite bias results are used to gain complementary information about the device response, which allows to operate it as a calibration-free

detector of MW power. These results can be rationalized invoking an effective AC bias to model the classical radiation interacting with the quantum mechanical states in the DQD. This systems shows the highest potential in terms of the figures of merit among the three presented here, but requires more stringent conditions in terms of gate voltages and operation temperature.

La detezione della radiazione a microonde (MW) è essenziale per un'ampia gamma di applicazioni, come le telecomunicazioni, la cosmologia e le tecnologie quantistiche. In alcuni regimi, non è ancora emersa chiaramente una tecnologia prevalente a questo scopo, sebbene siano state sperimentate soluzioni distinte in contesti diversi.

Ad esempio, lo Square Kilometer Array è un progetto internazionale su larga scala per la costruzione di un radiotelescopio di prossima generazione. [1] Fornirà una copertura continua nella gamma di frequenze 50 MHz-13,8 GHz e comprenderà $\sim$ 100 000 antenne in due continenti. L'enorme scala di questa infrastruttura richiederà rilevatori a basso costo, scalabili, efficienti e a banda larga.

Nel campo delle tecnologie quantistiche, la radiazione a microonde gioca un ruolo fondamentale nella manipolazione e nell'accoppiamento dei qbit. [2] L'implementazione di rivelatori di singoli fotoni potrebbe spingere il settore a nuovi risultati. Ma la realizzazione di un rivelatore che funzioni in maniera continua, veloce, a basso rumore e con elevata efficienza è ancora un problema aperto. Ciò è dovuto alla piccola energia dei fotoni alle MW $\hbar\omega$, $10^4 - 10^5$ volte più piccola della controparte ottica per la quale esistono già rivelatori di singoli fotoni ad alta efficienza.

I regimi di funzionamento in queste due applicazioni differiscono notevolmente: i dispositivi quantistici che coinvolgono la radiazione a microonde vengono generalmente utilizzati a una temperatura di pochi mK in ambienti criogenici schermati, a basso rumore. Lo Square Kilometre Array utilizza telescopi terrestri ed è influenzato da rumore di fondo come la radiazione cosmica di fondo e altre sorgenti di MW. Evidentemente, queste applicazioni richiedono soluzioni drasticamente diverse allo stesso problema fondamentale: il rilevamento della radiazione a microonde.

Questa tesi si concentra sullo studio sperimentale di dispositivi a base di nanostrutture III-V come rivelatori nella gamma 1-10 GHz. Questi dispositivi sono costituiti a partire da NW sia semplici che eterostrutturati; questi ultimi sono stati utilizzati per definire Quantum Dot (QD) e Doppi Quantum Dot (DQD). Ad un livello fondamentale, l'interazione della radiazione con questi sistemi dipende dal tipo di nanostruttura considerata. La radiazione alle MW classica può portare a fenomeni elettrici, come la modulazione della densità di portatori dentro il nanofilo, ma anche a una serie di effetti dovuti al riscaldamento indotto dalle MW. Ciò è più evidente nei NW semplici, dove diversi meccanismi di interazione possono portare a una rettifica da ac a dc. Poiché questi fenomeni sono qualitativamente simili, distinguerli è estremamente complesso. Nei sistemi quantistico invece,

l'interazione degli stati energetici discreti con la radiazione classica o con i singoli fotoni alle MW può portare a effetti radicalmente diversi. In questi sistemi la radiazione alle MW è di particolare interesse in quanto le energie dei fotoni (40
mueV a 10 GHz, equivalenti a un'energia termica di $\sim$ 0,5 K) sono confrontabili con le tipiche scale energetiche dei quanti dispositivi (da μeV a meV).

I prossimi capitoli descrivono il lavoro che ho svolto, il quale consiste nell'intero processo di fabbricazione e caratterizzazione: dal disegno del dispositivo all'analisi dati. La fabbricazione cominciava con la scelta del campione di nanofili più adatto, fra quelli cresciuti ai laboratori NEST a Pisa. A seconda del dispositivo che si voleva realizzare, diverse configurazioni di substrati e pattern sono stati fabbricati tramite litografia ottica. In questo step venivano definite la maggior parte delle strutture aventi dimensioni di $\mu m - mm$: contatti DC, risonatori superconduttori e microstriscie. L'ultimo step di fabbricazione consisteva nell'integrazione dei nanofili tramite litografia elettronica. La caratterizzazione elettrica dei dispositivi è stata effettuata o a temperatura ambiente in una probe station, o a bassa temperatura (0.3-300K) in due criostati che ho cablato per misure a bassi livelli per misure di magneto-trasporto in dc. Per finire, i dati venivano acquisiti utilizzando il framework Python QcoDeS, e la loro analisi svolta in Igor Pro. Su un totale di 367 dispositivi a nanofilo, $\sim$200 sono stati fabbricati da me a Modena, $\sim$160 a Pisa. Dei circa 300 fabbricati con successo, 150 funzionavano correttamente, con una percentuale di successo che è cresciuta nel tempo, come risultato di migliorie effettuate nel processo di fabbricazione.

La sezione dei risultati è suddivisa in tre parti. Nella prima parte presento la potenziale applicazione dei transistori ad effetto di campo (FET) NW come rivelatori di radiazione MW, in un regime in cui la rettifica classica non funziona a causa della frequenza di taglio intrinseca nella risposta del dispositivo. Viene studiato l'impatto sull'efficienza di rilevamento di diversi parametri (come la tensione di gate, la temperatura e la frequenza delle microonde) e viene discusso il meccanismo di rilevamento. Questi rivelatori mostrano buone prestazioni e funzionamento stabile in un ampio intervallo di temperatue (20-300 K) con due modalità di rilevamento: misurazione di corrente o di tensione. Nella seconda parte, presento l'effetto della radiazione MW su un QD.[3] Questo è stato ottenuto partendo da un InAs NWs, in cui due strati InP sono stati definiti epitassialmente lungo la direzione assiale durante il processo di crescita. Questi due materiali hanno diversi band gap e allineamento di banda adatto a fornire un robusto confinamento degli elettroni, e quindi QD ben definiti. La radiazione a microonde viene in questo caso fornita al sistema attraverso un risonatore a microonde coplanare superconduttore (in YBCO) che amplifica il campo elettrico in prossimità del

dispositivo, fornendo un effetto di “focalizzazione”. Ciò migliora notevolmente l’accoppiamento della radiazione MW al QD, a costo di limitare l’uso del dispositivo a una singola frequenza. Infine, nella terza parte, viene presentato l’impatto della radiazione a microonde nella gamma 1-10 GHz sulle caratteristiche di trasporto di un DQD. I risultati con voltaggio di bias zero e finito vengono utilizzati per ottenere informazioni complementari sulla risposta del dispositivo. Ciò consente di utilizzarlo come rilevatore di potenza MW senza dover prima effettuare una calibrazione con un riferimento esterno. Questi risultati possono essere razionalizzati invocando un bias efficace AC, il quale per fornisce un modello semplificato della interazione della radiazione classica con gli stati quantistici discreti nel DQD. Questo sistema mostra il potenziale più alto in termini di figure di merito tra i tre qui presentati, ma richiede condizioni più stringenti in termini di tensioni di gate e temperatura di funzionamento.

CONTENTS

ACRONYMS

AR	Active Rectification
BE	Bolometric Effect
BG	Back Gate
DQD	Double Quantum Dot
DS	Drain-Source
FEG	Field Emission Gun
FET	Field Effect Transistor
G1	Side Gate 1
G2	Side Gate 2
MW	Microwave
NEP	Noise Equivalent Power
NW	Nanowire
PAT	Photon Assisted Tunneling
PSB	Pauli Spin Blockade
PTE	Photo Thermoelectric Effect
QD	Quantum Dot
QDR	Read out Quantum Dot
QPC	Quantum Point Contact
RIE	Reactive-Ion Etching
SEM	Scanning Electron Microscope
SG	Side Gate
SNR	Signal to Noise Ratio
TEM	Transmission Electron Microscopy
YBCO	$YBa_2Cu_3O_7$
ac	Alternating Current
cQED	circuit Quantum Electrodynamics
dc	Direct Current

Part I

STATE OF THE ART

1 INTRODUCTION

Detectors of microwave photons find applications in different fields ranging from security to cosmology. Due to the intrinsic difficulties related to the detection of vanishingly small energy quanta $\hbar\omega$, significant portions of the microwave electromagnetic spectrum are still uncovered by suitable techniques. To better appreciate the energy scales at play, we consider frequencies in the 1 GHz $< \omega/2\pi <$ 300 GHz range, which in vacuum correspond to wavelengths 300 mm $> \lambda >$ 1 mm, the equivalent energy results 4 μeV $< \hbar\omega <$ 1.2 meV. Such small values require low temperatures ($k_B T \ll \hbar\omega$) to suppress the thermal background: the energy of a photon at 10 GHz corresponds to a temperature of 480 mK, while at 300 GHz to 14.4 K.

For example, single-photon detectors find potential applications in several areas of physics and constitute relevant tools in the context of quantum technologies. In circuit Quantum Electrodynamics (cQED), microwave photon detectors may allow the remote entanglement of distant qubits or the development of quantum computation with photonic qubits [2]. Microwave photon detectors find application also in the search of dark matter particles for which the development of suitable detection techniques in the 5 to 500 GHz range is strongly demanded [4–7]. Despite this strong interest and while in the visible range single-photon detection techniques are relatively well established [8], microwave photon counters have been reported only recently [9–16].

In this work I systematically study semiconductor nanowire based devices such as bare nanowires, quantum dots and double quantum dots. In these chapter I will introduce the relevant properties of these systems . In the first part I briefly introduce semiconductor nanowires and their mechanisms of interaction with microwave radiation. I will discuss possible pathways for the development of microwave photon detectors based on photon-assisted tunnelling in semiconducting quantum dot first and double quantum dots second. With what concerns the latter I consider implementations based on either broadband transmission lines or resonant cavities and how developments in charge sensing techniques and hybrid architectures may be beneficial for the development of efficient photon detectors in the microwave range.

FIG. 1.1: Transmission Electron Microscopy Image of a single nanowire.

1.1 NANOWIRES

Nanowires (NW) are a class of nanomaterials characterized by a quasi 1D structure. They have strong aspect ratios, with lengths that go from ~ 1 μm to tens of μm and diameters that typically range from few to hundreds of nm. They can be realized from different material - such as oxides, metals and superconductor - but the focus here is on semiconductor nanowires. These are of great interest because, similarly to their bulk counterpart, they offer good control over the electrical properties through doping, the possibility of creating junctions and field effect tuning of the carrier density. Yet additional, non trivial, features emerge as a result of reduced dimensionality.

A key feature of NWs is that they are electrically active. A nanowire contacted with source, drain and gate contacts can be electrically characterized, showing features typical of Field Effect Transistors (FET): by applying a voltage on the gate contact we can control the resistance of the nanowire and tune it in off (high resistance) and on (low resistance) configurations.

A common feature of all nanostructures is their high surface-to-volume ratio, which makes them extremely sensitive to the environment they are embedded in. This is also true for semiconductor nanowires, where it is reflected on the electrical properties such as the resistance. This serves as a convenient and attractive sensing modality. [17] Furthermore the size of the nanowires can be comparable to the biological and chemical species sensed, which intuitively explains why they can be so sensitive.

The optical properties of nanowires also present an unique opportunity for sensing of chemical species, for detection of radiation and for its manipulation. For example InAs nanowires integrated in appropriate antennas have been used for polarized detection of THz radiation [18, 19], and can be used for polarization control when integrated on Silicon waveguides. [20]

Finally, the low dimensionality introduces new opportunities in the control of the electrical, photonic and phononic properties of the semiconductors through material engineering. By epitaxially growing different materials with the appropriate band gap alignment it is possible to realize diodes, quantum dots, double quantum dots and superlattices. By covering the nanowire with different materials core-shell structures can be realized.

Nanowire fabrication techniques can be split in two categories: bottom-up and top-down. Molecular or chemical beam epitaxy are used for bottom up, self assembled growth. While top down processes typically define nanowires through etching processes. Figure 1.1 shows a single InAs nanowire grown bottom up through chemical beam epitaxy.

The focus of this work is on InAs (a III-V semiconductor) nanowires. III-V bottom up grown nanowires are of particular interest because of their high mobility [21–23], high g factor [24, 25], strong spin-orbit interaction [26–28], and the possibility of forming quantum dots. [29]

1.1.1 *MW detection with nanowires*

In this chapter I will introduce some of the mechanisms of interaction between radiation in the GHz range and semiconductor nanostructures. They can be broadly split into thermally and electrically driven. Among the thermally driven I consider the bolometric effect and the photo thermoelectric effect. Among the electrically mediated I will discuss the active rectification in FETs and plasma waves. Another mechanism, photon assisted tunnelling, is described in chapter 1.2.1.1 because it pertains only to systems with discrete energy levels.

1.1.1.1 *Bolometric effect*

Bolometry is one of the most established radiation sensing techniques. It was discovered more than a century ago[30] but is still widespread. [31] This is due to its flexibility in terms of bandwidth and dynamic range, as well as the possibility of performing energy-resolving calorimetric operations. [32] In a bolometer an absorbing element converts the impinging radiation into heat. A resistive thermometer, whose electrical resistance varies as a function of temperature, senses the temperature change in the absorbing element. If the device is biased with a current I, a voltage drop which depends on the device resistance is produced $V = IR(T)$. The bolometric effect (BE) has been discussed in the literature for nanowires coupled to antennas, operated as detectors at THz frequencies [18], where it was found that it leads to a voltage response at low carrier densities ($n \sim 10^{16}$ cm^{-3}), while at higher carrier densities other effects dominate.

1.1.1.2 *Photo thermoelectric effect*

The photo thermoelectric effect (PTE) emerges as a result of asymmetric heating of the device due to radiation. The standard thermoelectric effect describes the emergence of a voltage across a conducting material when a temperature gradient is present at the device extremes. The voltage gradient is given by $\nabla V = -S\nabla T$ or equivalently the thermoelectric current is given by $I_{TE} = -\sigma S \nabla T$, where T is the temperature, S is the Seeback coefficient and σ is the electrical conductivity. In the PTE the temperature gradient is generated by the impinging radiation. The heating must be asymmetric, meaning that it must affect the two extremes of the device differently in order for a temperature gradient to emerge. The efficiency of a thermoelectric material is captured by the figure of merit $ZT = \frac{S^2\sigma}{k}T$ where

k is the thermal conductivity which typically includes electron and phonon contributions: $k = k_{electron} + k_{phonon}$. The thermoelectric effect in semiconductor nanowires [33, 34], Quantum Dots [35] and Double quantum dots [36] has attracted increasing attention in the last decade; low dimensionality semiconductors can combine good electrical conductivity and low thermal conductivity. In particular the k_{phonon} term can be drastically reduced through reduced sizes, interface scattering and phonon dispersion engineering.

Nanowire based devices have been used to demonstrate radiation detection mediated by this effect at THz frequencies [18, 37]. PTE is most effective at high carrier densities $n > 10^{17}$, which is consistent with the requirement of good conductivity and the observation in bulk semiconductors that highest ZT values are obtained for high doping levels.

1.1.1.3 *Active rectification*

Active rectification (AR) is the most commonly used technique for ac to dc rectification in FETs. Classical ac to dc rectifiers can employ diodes thanks to their intrinsic asymmetry in conductivity. FETs can similarly be used through AR, although they lack intrinsic asymmetry in the response: the variable resistance of the FET is used to selectively allow the current flow only in one direction. This is typically archived through comparators that sense the incoming radiation and apply a voltage on the gate electrode with the right timing in order to open the channel only in a portion of the oscillating ac voltage. While active rectification is not an intrinsic effect, since it requires external control in order to be archived, we discuss it here because it is the most widely used technique for rectification in FETs. Because of the small scale of our devices we cannot exclude a crosstalk between source-drain and gate contacts, which might lead to unexpected modulation of the nanowire conductance. The applicability of this approach is limited at high frequencies by the RC cut-off of any device. The value of the cut-off frequency can be estimated for our nanowire devices starting from the DC parameters in the quasi-static approximation: [38, 39]

$$f_T = \frac{g}{2\pi C} \tag{1.1}$$

Where g is the maximum of the transconductance and C is the total gate capacitance of the device.

1.1.1.4 *Plasma waves*

The theory of Plasma Waves in Field Effect Transistors was initially formulated for 2D electron gas devices at the THz frequencies,[40, 41] but has since then been shown to work also in nanowire devices[42] and at GHz frequencies.[43] The shallow water analogy of the plasma

modes applies when the field effect transistor is small enough that electrons experience no collisions with phonons or impurities during the transit time (such a device is typically said to be ballistic), but the electron concentration is so high that electron-electron collisions are frequent. In such condition the single electron is not ballistic, but collective plasma modes are possible. An asymmetry between the source and drain contacts is needed, which can have several origins: external parasitic capacitances, asymmetry in the radiation feeding mechanism or by passing a dc current in the device, creating a depletion region in the electron density on the drain side. Figure 1.2 shows the schematic model used here. A simplifying hypothesis is made: the radiation creates an ac voltage with amplitude U_a only between source and gate contacts. The main components of this system are the gate to channel capacitance and the channel resistance:[44]

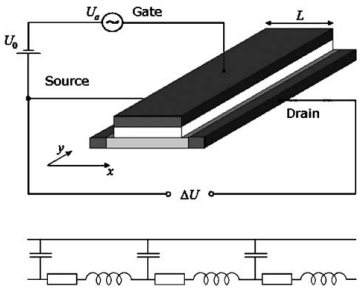

FIG. 1.2: Schematics of a FET detector and the equivalent circuit. Reproduced from [44].

$$en = CU \tag{1.2}$$

where e and n are the electrons' charge and concentration respectively, C is the gate-to-channel capacitance per unit area and U is the gate to channel voltage. Under static conditions and in the absence of a drain current $U = U_0 = V_g - V_{th}$, where V_{th} is the threshold voltage at which the channel is depleted. A key quantity in this picture, which determines the time-scales in the system, is the electron momentum relaxation time τ, determined by the conductivity in the channel $\sigma = \frac{ne^2\tau}{m}$. Depending on the frequency ω and the channel length L (defined by the source-drain electrode distance) different regimes can be identified:

- High frequency regime: when $\omega\tau > 1$ the kinetic inductances are relevant and plasma waves analogous to waves in an RLC transmission lined are excited. The plasma waves' velocity is $s = \sqrt{\frac{eU}{m}}$ and they have relaxation time τ. The propagation distance $s\tau$ marks two sub regimes.
  - Short gate $L < s\tau$. The plasma waves reach the drain side, reflect and form standing waves with a resonant frequency $\sim s/L$
  - Long gate $L \gg s\tau$. The waves decay before reaching the drain side.
- Low frequency regime: $\omega\tau \ll 1$, also called the overdamped regime. The plasma waves cannot exist, the inductances are not significant and the circuit behaves like an RC line. A characteristic τ_{RC} is then defined as the RC time constant of the line. $\tau_{RC} = L^2\rho C$ since total channel resistance and capacitance are respectively $R = L\rho/W$ and $C_{tot} = CWL$, where W is the gate width. Once again, two sub regimes can be identified depending on the length L.

- Short gate $L < \sqrt{\rho C \omega}$. Therefore $\omega \tau_{RC} < 1$ and the ac current goes through the gate-channel capacitance uniformly.
- Long gate $L \gg \sqrt{\rho C \omega}$. $\omega \tau_{RC} \gg 1$ and the ac current leaks to the gate at a distance lower than L. No ac signal will be present at the drain side.

If the gate length is sufficiently small two distinct regimes of rectification are possible: resonant at plasma oscillation frequencies, broad-band at low frequencies.

Rectification mechanism

The rectification of the signal happens because of the electron density modulation by the local ac field. The electric current $j = env$ is affected through both the density n and the drift velocity v. As a result a dc current $j_{DC} = e\langle n_1(t) v_1(t) \rangle$ energies, where n_1 and v_1 are the modulated components of n and v. The brackets denote the averaging of these quantities over an oscillation period $2\pi/\omega$. Equivalently, if the circuit is open, a source-drain voltage will be induced.[45]

$$\Delta U = \frac{U_a^2}{4U_0} \left(1 + \frac{2\omega\tau}{\sqrt{1 + (\omega\tau)^2}} \right) \tag{1.3}$$

1.2 QUANTUM DOTS

Single (few) electron transistors based on semiconductor quantum dots (QDs) are flexible solid-state components characterised by extensive control of charge, orbital and spin degrees of freedom. Electrons fill the dot in a shell structure in analogy with artificial three dimensional atoms and their wavefunctions depend on the shape and size of the system [46–48]. Orbital properties, in turn, determine the tunnelling current and more in general the QD response to external stimuli.

A quantum dot is a zero-dimensional system, that can be modelled as a three dimensional potential box. The discrete energy states can be found by solving for the eigenstates ψ_n of the time independent Schrödinger equation:

$$H\phi_n = \epsilon_n \psi_n \tag{1.4}$$

If we consider one-dimensional well with infinite potential walls, its eigenenergies are:

$$\epsilon_n = \frac{\hbar^2 k_n^2}{2m} \tag{1.5}$$

$$k_n = \frac{\pi}{L} n \tag{1.6}$$

Where k_n are the wave-vectors of the states, m is the mass of the electrons, L is the distance of the two walls, n is the quantum number

that defines the eigenstate and $\hbar$ is the reduced Planck constant. This problem can be readily generalized to a three dimensional problem. This picture works extremely well for hard wall devices, where the potential barrier originates from the sharp heterostructure interface, but fails in gate defined QD, where the potentials are applied through external gates, leading to broader potential profiles.

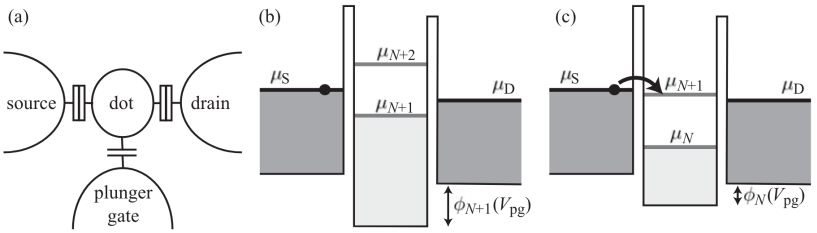

FIG. 1.3: (a) Classical model of a Quantum Dot: a metallic island is connected through tunnelling barriers (which contain a resistive and a capacitive component in parallel) so a source and a drain contact. In addition a plunger gate is capacitively coupled to the island. (b) Addition energies of the system in a non conductive configuration: no addition energy of the QD μ_{N+1}, μ_{N+2} is aligned with μ_S and μ_D. (c) Conductive configuration of the QD. All of the addition energies are aligned in such a way that successive tunnelling events can lead to electron transport.

A classical picture of a quantum dot (shown in figure 1.3) is useful in order to understand the peculiar features of these systems. In this model the quantum mechanical discrete energy states are ignored, and the system is simply modelled in terms of capacitances. Intuitively, if the dot is small enough, the addition of a single electron leads to significant charging. In order to add a new electron to the QD a charging energy must be provided in order to overcome the electronic repulsion. A formal description of this intuitive picture is given by the constant interaction model [49]. Two main assumptions are made: [50]

- the QD can be described as a capacitor, with a capacitance C that has several contributions due respectively to the source (C_S), the drain (C_D) and the gates (C_G): $C = C_S + C_D + C_G$.
- the original, single particle energy levels of the QD are not perturbed by the presence of other electrons in the QD.

The addition energy for the N-th electron is then given by:[51]

$$\mu_N = E_k + \frac{Ne^2}{C} - |e|\alpha_{avg}V_G + c \tag{1.7}$$

Where E_k are the single particle QD energy levels, $\frac{Ne^2}{C}$ is the charging term and α_{avg} is the lever arm that takes into account how the gate voltage V_G affects the QD energy. c is a constant.

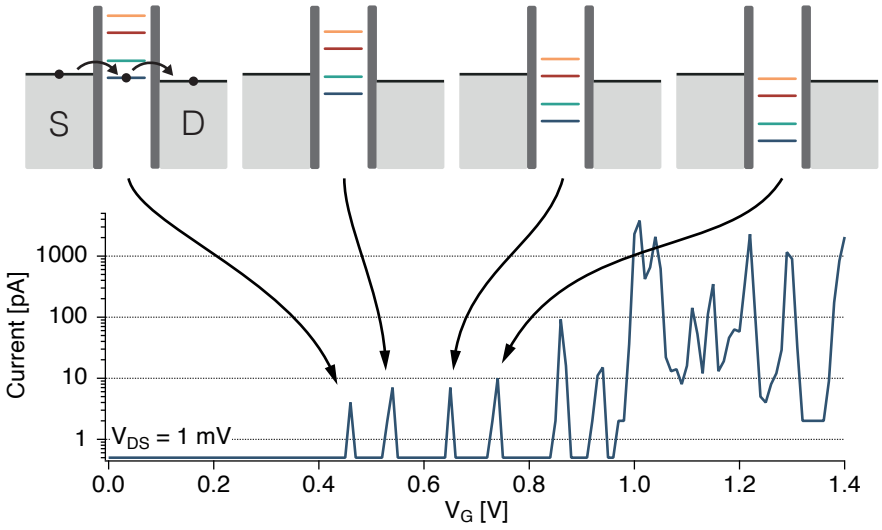

FIG. 1.4: Schematic representation of the current as a function of the gate voltage for a fixed, small V_{SD} (typically few mV). The diagrams illustrate the successive level alignments from which each current peak emerges.

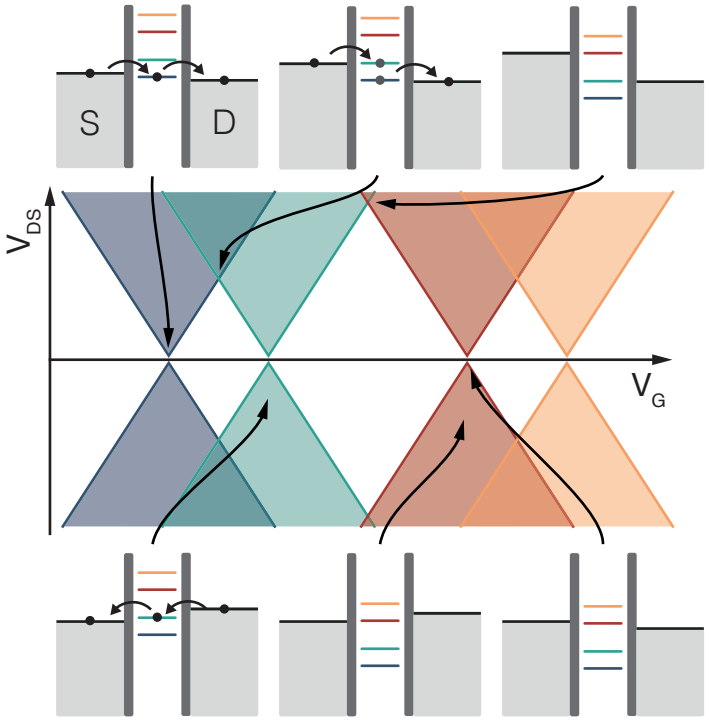

FIG. 1.5: Coulomb blockade diagram. The shaded regions mark non-zero current regions in the space of V_{SD}-V_{Gate} voltages. The alignments of the electrochemical potentials of source, drain and QD are highlighted in some special cases. The color of the shaded regions match the color of the energy level in the QD from which such current is originated.

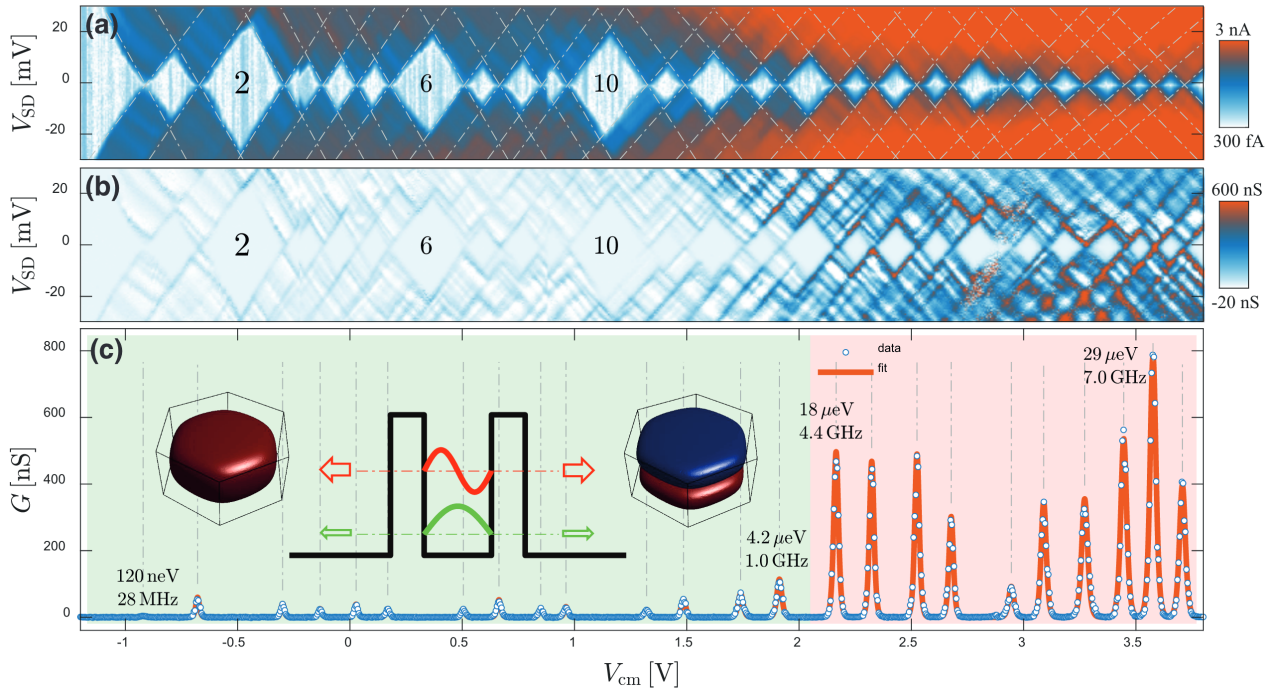

FIG. 1.6: (a) Current map as a function of bias V_{SD} and gate voltage V_{cm} of an InAs/InP quantum dot. (b) Differential conductance dI/dV map of the same device. (c) Zero-bias differential conductance G Green and orange regions mark two different regimes with significant difference in conductance values. The inset shows the waveform of states having different axial components, which is reflected in distinct conductance regimes. Reproduced from [52].

The gate voltage separation between two addition energies ΔV is given by:

$$|e|\alpha\Delta V = \frac{e^2}{C} + \Delta E \tag{1.8}$$

This contains a term that is due to charging and one due to the intrinsic separation of the energy level. All of the states are degenerate due to spin, with possible additional degeneration depending on the orbital configurations. In these cases $\Delta E = 0$ and the separation ΔV provides direct information about the charging energy.

Conduction through the QD is only allowed under precise conditions: the energy levels in the dot and the electrochemical potential μ in the source and drain must be aligned in such a way to allow successive tunnelling events. This is verified at $V_{DS} \sim 0$ only when all levels are aligned, as shown in figure 1.4. If instead a finite bias is applied, a window of configurations opens where the electron can tunnel across the device though dissipative processes. This situation is depicted schematically in figure 1.5.

The mapping of the current as a function of the bias and gate voltages allows the study of a variety of second order process. As an example, figure 1.7 shows the current features due to excited states in the QD. These states cannot contribute to the current at low V_{SD}

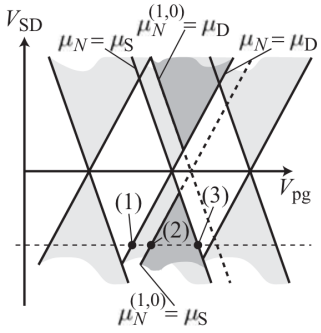

FIG. 1.7: Schematic representation of the current in the coulomb diamonds when excited states are taken into account. The dark shaded region represent the higher current expected thanks to the contribution of the excited state to the total current.

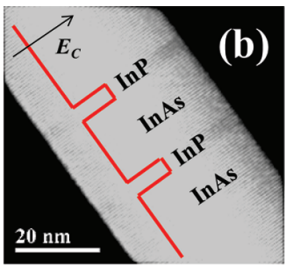

FIG. 1.8: Scanning Transmission Electron Microscopy image of a nanowire InAs/InP QD. Inset showing conduction band alignment with the material change. Reproduced from [53].

because they are too high in energy. But if V_{SD} is higher than the energy separation of the excited state, it too falls within the bias window and can contribute to the total current, leading to regions with higher tunnelling rates.

Bottom-up grown InAs nanowires (NWs) recently emerged as a reliable platform to produce single [48, 51, 53, 54] and double [55, 56] QDs with strong electron confinement. In the case of high aspect ratio NW QDs, lowest lying states have dominant radial character while an axial component can characterise their excited states [48].

Typically, the separation of their energy levels can be controlled between few tenths to tens of meV during growth [29], while further tuning of NW QD energy levels can be obtained by (multi) gating. [53] Heterostructured InAs/InP NW QDs are characterised by hard-wall confinement potential and large single-particle energy spacing with Coulomb and Pauli blockade detectable up 50 and 10 K, respectively. [53, 56] Thanks to their large spin-orbit coupling, InAs NW QDs have been proposed as spin qubits with electric control of the spin degree of freedom. [57, 58]

1.2.1 *MW detection with Quantum Dots and photon assisted tunnelling*

QDs coupled to microwave (MW) transmission lines and resonators have been also proposed and developed for electronics and quantum technology applications. [59–64] When the photon energy $\hbar\omega$ matches the level spacing, coherent and/or resonant phenomena may occur and NW QDs may function either as single-atom maser sources [65–67] or as photon detectors in the MW range [68]. Non-resonant MW excitation may assist tunnelling process thus affecting the charge transport characteristics, as observed on other semiconductor quantum well[69] and QD systems: effects of electromagnetic radiation on Coulomb blockade peaks were reported for electrostatically defined GaAs QDs [70–72] and single-walled carbon nanotubes [73, 74]. The lifting of Coulomb blockade in the presence of MW radiation can be described in terms of photon-assisted tunnelling (PAT) [75] that, in the quantum limit ($\hbar\omega > k_B T$), gives rise to inelastic single-electron tunnelling [71]. In the high MW power regime, sidebands of the main Coulomb peaks appear and excited states within the QD can contribute to assist the tunnelling process [71]. This situation was not explored so far in heterostructured InAs/InP NW QDs despite their significant technological potentials.

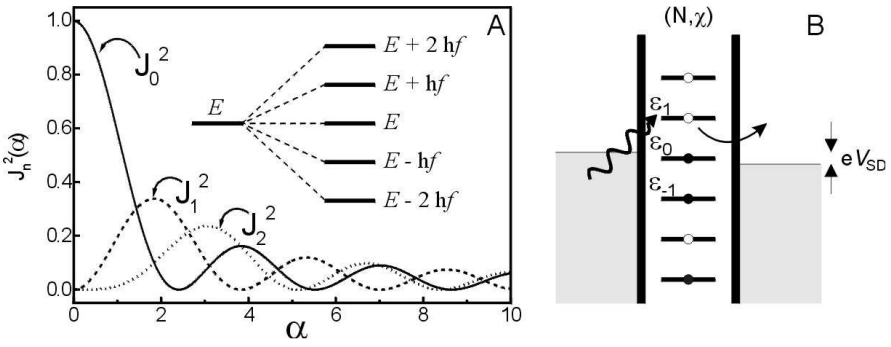

FIG. 1.9: A: squared Bessel function of the first kind. The inset shows the splitting of the initial energy state into sidebands with hf spacing. B: Schematic energy diagram of a single quantum dot. The presence of the MW radiation allows tunnelling to the state ϵ_1. Reproduced from [71].

1.2.1.1 *Photon assisted tunnelling*

Photon Assisted Tunnelling is a well known phenomena of discrete energy systems such as Quantum Dots and Double Quantum Dots. It provides a picture for the transport features of low power MW illumination on these devices. The power regimes explored in the results sections are higher than those described here, but the low power is a useful reference since certain features of the two regimes are similar. By increasing the power one can shift continuously from the low power, particle like nature of radiation to the high power, wave like one. The MW radiation leads to the formation of sidebands starting from every discrete energy state E, with energies $E + nhf$, where f is the radiation frequency and $n = 0, \pm1, \pm2....$ These correspond to absorption ($n > 0$) or emission($n < 0$) of n microwave photons. The theoretical description of this phenomena was adapted from the Tien-Gordon theory [75] for tunnelling through a single barrier. The MW are modelled by an oscillating potential $V\cos(2\pi f)$ on the QD.[76] The voltage drop across the barriers is written in two terms $\alpha_i = eV_i/hf$ where i marks the source or drain side. The tunnelling rate $\tilde{\Gamma}_i$ perturbed by the MW radiation is written in terms of the unperturbed one Γ_i:

$$\tilde{\Gamma}_i(\epsilon_i) = \sum_{n=-\infty}^{n=\infty} J_n^2(\alpha_i)\Gamma_i(\epsilon_i + nhf) \tag{1.9}$$

where J_n are the Bessel functions of the first kind, shown in figure 1.9. The tunnelling rate without microwaves is given by the expression:

$$\Gamma_i(\epsilon) = \frac{G_i}{e^2}\frac{\epsilon_i}{1 - e^{-\frac{\epsilon_i}{k_B T}}} \tag{1.10}$$

where G_i is the conductance of the junction and ϵ_i is the energy difference between the initial and final states. The Bessel functions determine therefore the occupation probability of each side-band. This corresponds directly to the formation of photocurrent bands to the sides of the unperturbed current peak. The population probability of each current side-band $n = 0, \pm1, \pm2...$ is $P(n) = J_n^2\left(\frac{eV}{hf}\right)$. Therefore the Bessel functions describe the evolution of the current peaks as a function of the MW power, as shown in figure 1.11.

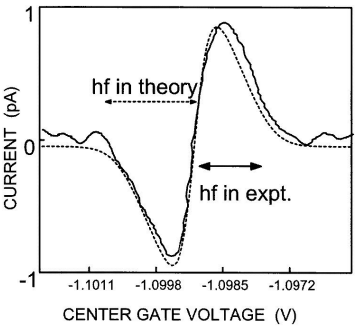

FIG. 1.10: Measured (solid) and calculated (dashed) photocurrent at zero bias. Reproduced from [70].

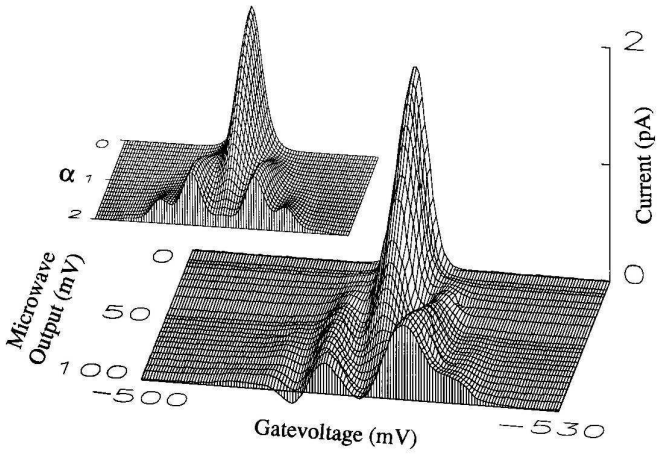

FIG. 1.11: Current through a QD as a function of the gate voltage and the output voltage of the microwave source. Inset: theoretical calculation of the current under the same conditions. Reproduced from [71]

1.3 DOUBLE QUANTUM DOTS

Double Quantum Dots are realized by fabricating two QDs so close that a partial overlap of the respective wavefunctions is possible. Under the right conditions, hybridization of the quantum states in the two systems can happen, leading to the formation of bonding and antibonding states. These devices show a rich phenomenology and are widely studied because they enable manipulation of the charge and spin energy levels to a degree which is otherwise impossible in single quantum dots.

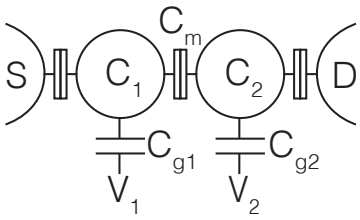

FIG. 1.12: Classical capacitance model of a DQD

1.3.1 *Capacitance model*

In this section we provide a model of DQD, describe their transport features and show how they can be used to gain information about the energetics of these systems. All of this is treated in detail by Van der Wiel et al. [77], here we provide just the main points needed in order to discuss our results. The classical model of a Double Quantum Dot is extremely useful in order to understand most if its features. Figure 1.12 sketches said model: each quantum dot is a capacitor connected to the other one and one source/drain contact by tunnelling barriers, consisting of a resistance and a capacitance in parallel. The two dots are individually controlled by capacitively coupled electrodes. Whenever an electron is added to a QD, charging it, an additional charging energy ($E_{C1(2)}$) is required to add the next one. An electrostatic coupling energy E_{C_m} is also present: this is the

energy shift of each dot when an electron is added to the other. These energies can be written as follows:

$$E_{C1} = \frac{e^2}{C_1}\left(\frac{1}{1-\frac{C_m^2}{C_1 C_2}}\right) \tag{1.11}$$

$$E_{C2} = \frac{e^2}{C_2}\left(\frac{1}{1-\frac{C_m^2}{C_1 C_2}}\right) \tag{1.12}$$

$$E_{C_m} = \frac{e^2}{C_m}\left(\frac{1}{\frac{C_1 C_2}{C_m^2}-1}\right) \tag{1.13}$$

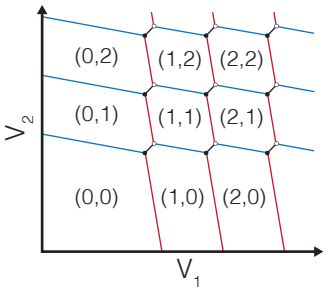

FIG. 1.13: Stability diagram of a double quantum dot with finite interdot coupling. The lines correspond to the condition of having $\mu_{1(2)}(N_1, N_2)$ aligned to the respective lead contact.

Where $C_{1(2)}$ is the total capacitance of the dot. The electrochemical potential $\mu_{1(2)}(N_1, N_2)$ is the energy needed to add the $N_{1(2)}$ electron to the 1(2) QD, while $N_{2(1)}$ electrons are trapped in the other one. The gate voltages can shift the electrochemical potential, leading to the addition of electrons to the device. Figure 1.13 shows the corresponding stability diagram with occupation numbers. The characteristic honeycomb patter emerges as a result of the finite interdot coupling. The intersection between the [(0,0),(0,1),(1,0)] regions and [(0,1),(1,0),(1,1)] are separated by the coupling energy E_{C_m}; the addition energies are not parallel to the axes because of the finite capacitive coupling between the QDs: the voltage of one shifts also the energy of the other.

In a zero bias configuration, in which the source and drain addition energies are the same, conduction is permitted only when all the levels are aligned, as shown in figure 1.14(a). This condition is verified in the triple points, marked in black and white in figure 1.14(c) in the DQD stability diagram. By measuring the positions of the triple points in the (V_{g1}, V_{g2}) parameter per la space, one can measure the following quantities, depicted in figure 1.14:

$$\Delta V_{g1} = \frac{|e|}{C_{g1}} \tag{1.14}$$

$$\Delta V_{g2} = \frac{|e|}{C_{g2}} \tag{1.15}$$

$$\Delta V_{g1}^m = \frac{|e|C_m}{C_{g1}C_2} = \Delta V_{g1}\frac{C_m}{C_2} \tag{1.16}$$

$$\Delta V_{g2}^m = \frac{|e|C_m}{C_{g2}C_1} = \Delta V_{g2}\frac{C_m}{C_1} \tag{1.17}$$

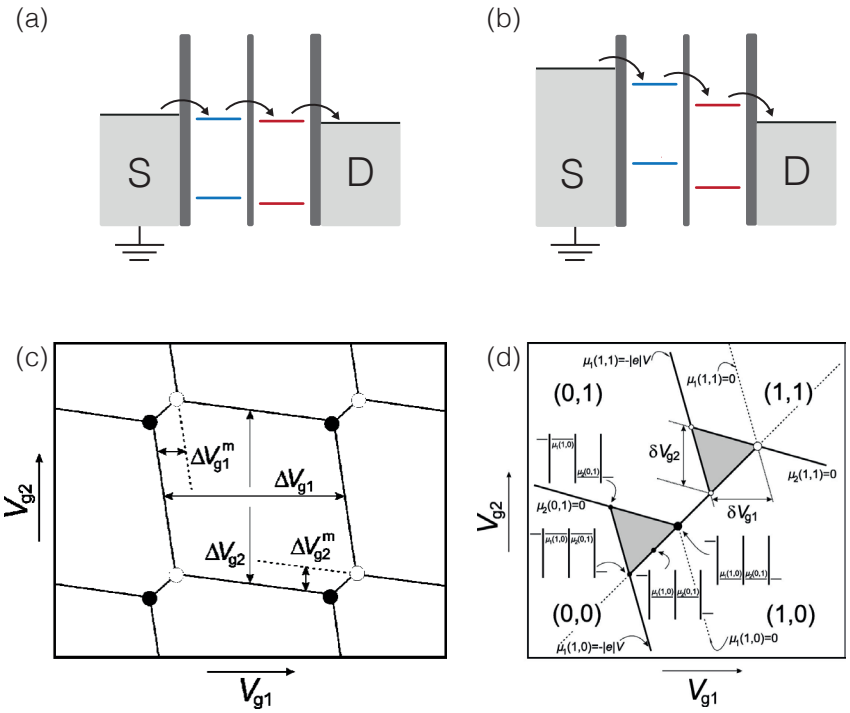

FIG. 1.14: (a) Sequential tunnelling at zero bias $V_{DS} = 0$. (b) Inelastic tunnelling for finite bias. The color marks distinct chemical potentials in the two dots. (c) Stability diagram of a DQD, with triple points marked in white and black. The quantities $\Delta V_{g1(2)}$ and $\Delta V_{g1(2)}^m$ can be determined from this map. (d) Finite bias map, showing the current triangles and selected chemical potential configurations leading charge transport. (c,d) taken from [77]

If a finite bias is applied, typically in the range $V_{DS} = \pm 1 - 15$ mV, a window of configurations which allow sequential tunnelling is opened. In a simplified picture, the electron must relax to an energetically favourable level in every tunnelling event, as shown in figure 1.14(b). This leads to the formation of current triangles in place of the triple points: a finite current is measured when the level alignment allows sequential tunnelling. From voltage differences between the triangle edges and from the knowledge of the bias applied in order to map said triangles, additional informations on the charging energetics can be obtained:

$$\alpha_{G1}\delta V_{g1} = \frac{C_{g1}}{C_1}|e|\delta V_{g1} = |eV_{DS}| \tag{1.18}$$

$$\alpha_{G2}\delta V_{g2} = \frac{C_{g2}}{C_2}|e|\delta V_{g2} = |eV_{DS}| \tag{1.19}$$

Where $\alpha_{G1(G2)}$ are the lever arms of the QD 1(2): this is the ratio of how much the QD energy shifts for a given voltage change in the respective gate. In other words these quantities provide a conversion between the applied voltages and the DQD energetics. From these quantities the charging energies of the devices are fully characterized.

The picture provided until now is fully classical. The quantum nature of the states involved does not change drastically the features described. One effect emerges when the levels in the two QD are energetically close: the orbital overlap in this case leads to the formation of new superposition states. If the tunnelling coupling is ignored,

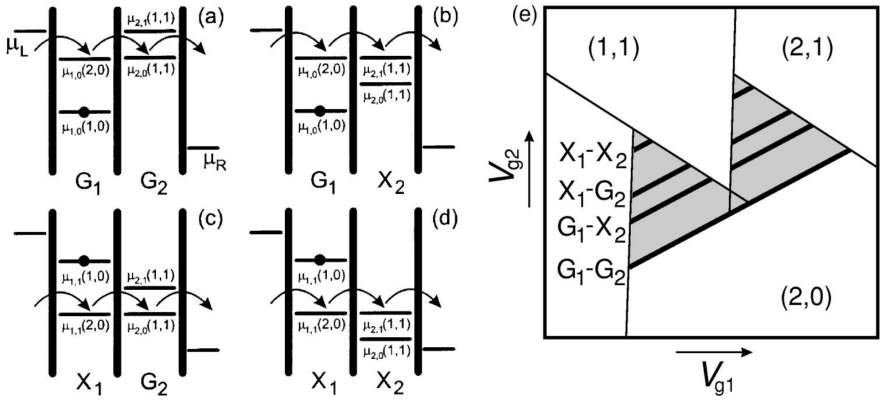

FIG. 1.15: Schematic diagram showing 2 energy levels for each quantum dot. All the configurations shown in (a,d) result in chemical potential alignment within a given bias window, allowing electron transport. In (e) the schematic finite bias stability diagram is shown. The black lines inside the triangles mark the position of current lines emerging each thanks to one of the alignments shown in (a-d). Reproduced from [77].

the total system Hamiltonian has two distinct eigenstates $|\phi_{1(2)}\rangle$ and eigenenergies $E_{1(2)}$ that correspond to the two QDs.

$$H_0|\phi_1\rangle = E_1|\phi_1\rangle \tag{1.20}$$

$$H_0|\phi_2\rangle = E_2|\phi_2\rangle \tag{1.21}$$

The finite tunnel coupling is introduced as a purely non diagonal matrix T with elements t_c. The total Hamiltonian becomes:

$$H = H_0 + T = \begin{bmatrix} E_1 & t_c \\ t_c & E_2 \end{bmatrix} \tag{1.22}$$

Which has two new eigenstates $|\psi_{B(A)}\rangle$ that have bonding and antibonding character. It is interesting to notice here how this resembles the formation of an "artificial molecule" with bonding and antibonding levels. Figure 1.16 shows the anti-crossing of the combined states as a function of the level detuning $\varepsilon = E_1 - E_2$. The energy difference between the two states reads:

$$\Delta E = E_A - E_B = \sqrt{\varepsilon^2 + 4|t_c|^2} \tag{1.23}$$

The stability diagram is almost unaffected by the anti-crossing: the triple points separation contains also a $2|t_c|$ contribution, which is typically much smaller than the electrostatic coupling energy E_{C_m}. Spectroscopic techniques can instead map the bending of the energy levels due to anti-crossing.

Another effect is the presence of excited energy levels in the QDs, which can be observed inside the current triangles: if the bias applied is wide enough, several combinations of excited and ground states can lead to sequential tunnelling as shown in figure 1.15. This is measured in the form of current lines that run perpendicular to the filling direction inside the current triangles, corresponding to each combination of energy levels. The width of these lines is set by the thermal broadening $k_B T$.

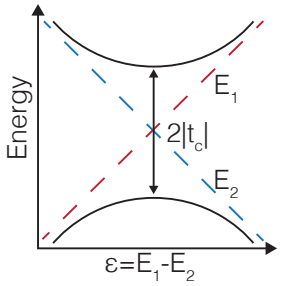

FIG. 1.16: Level anti-crossing for two tunnelling coupled QDs.

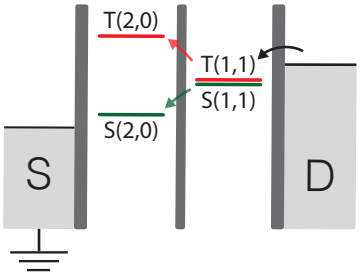

FIG. 1.17: Spin blockade tunnelling diagram.

1.3.2 *Spin Blockade*

Pauli Spin Blockade (PSB) emerges at transitions like $(1,1) \rightarrow (2,0)$. Figure 1.17 shows the mechanism of PSB, which requires to consider the spin states. In this configuration, at zero magnetic field, the ground state is typically a singlet state $|S\rangle = (|\uparrow\downarrow\rangle - |\downarrow\uparrow\rangle)/\sqrt{2}$. A singlet state of $|S(1,1)\rangle$ occupation can tunnel to a state of $|S(2,0)\rangle$ character since the spins are aligned differently: Pauli exclusion principle does not come at play. Triplet states $|T_0\rangle = (|\uparrow\downarrow\rangle + |\downarrow\uparrow\rangle)/\sqrt{2}$, $|T_+\rangle = |\uparrow\uparrow\rangle$, $|T_-\rangle = |\downarrow\downarrow\rangle$ have a zero magnetic field separation of J, the exchange energy, from the singlet states. The exchange energy depends on the wavefunction overlap of the two electron in the DQD, therefore $J(1,1) < J(2,0)$: the wavefunction overlap is much greater when the two electrons occupy the same QD. Typically a triplet state $|T(1,1)\rangle$ is energetically accessible and might be occupied, but the $|T(1,1)\rangle \rightarrow |T(2,0)\rangle$ is prohibited. This stops the flow of current until a spin flip event happens, which brings back the system to a singlet state. The spin relaxation is typically long, and therefore the measured current is very low. Only along the current triangle's edges, where one of the two energy levels is aligned with the respective lead, dissipative processes increase the spin flip rate. PSB is one of the most striking features of DQD both for spintronic applications, where they can be used as spin filters [56, 78], and in spin qubits, since it provides a spin to charge conversion for singlet-triplet DQD qubits, which is a precious tool for the readout of the spin state.[79, 80]

1.3.3 *MW detection with Double Quantum Dots*

Results discussed in this chapter were published in Sensors.[81]

Here, we draw our attention to the use of semiconductor double quantum dots as microwave photon detectors. These can be integrated in electronic circuits and scalable architectures as required for multipixel detection. The high tunability of simple Double Quantum Dot (DQD) structures by external gate potentials allows continuous tuning of energy levels spacings from GHz to THz frequencies. This is a remarkable feature that makes these systems complementary with respect to other quantum devices such as superconducting qubits. In DQDs, the absorption of a single photon drives electron transitions between the dots' levels, resulting in net variations of the DQD conductivity that can be measured with high sensitivity and large bandwidth by means of suitable charge sensors. On the other hand, DQDs are prone to coupling with phonons and charge noise, thus relaxation and coherence times are shorter than those of superconducting qubits. An additional characteristic of DQD devices is their large electric dipole moment, which leads to large coupling strengths with the electric field component of a microwave resonator. Thanks

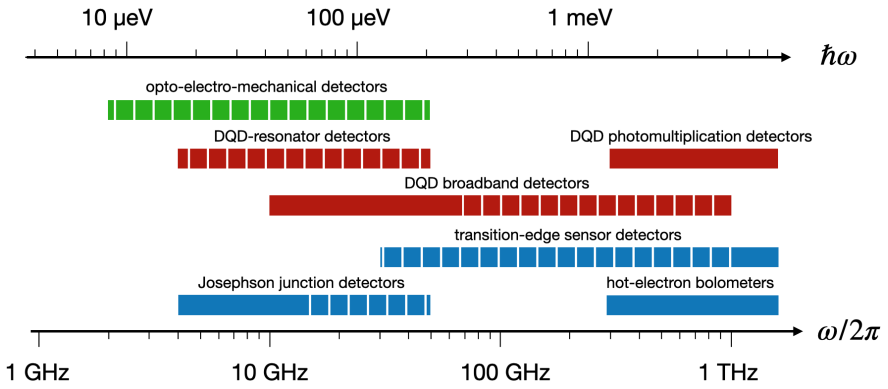

FIG. 1.18: Schematic diagram showing the frequency working range of different photon detectors based on quantum dots (red), superconducting circuits (cyan), and opto-electro-mechanical systems (green). Solid regions show the frequency range of experimentally tested detectors, whereas striped regions indicate possible developments and theoretical proposals. From reference [81].

to this feature, DQDs can be efficiently embedded in circuit quantum electrodynamics (cQED) architectures enabling fast manipulation and readout of charge or spin states by microwave fields. Based on these recent achievements, we discuss possible pathways to overcome limits and define next steps for the implementation of DQD-based microwave photon detectors.

State of the art

Broadly speaking, the working principle of photon detectors is based on the conversion of the impinging electromagnetic radiation into an electrical signal. Superconducting devices certainly represent a mature platform for the development of different types of photon detectors. Their working range in frequency is summarized in Figure 1.18. Superconducting qubits detectors have been successfully employed in the 4 to 20 GHz frequency range [2, 9–16, 82–91], which is in part related to the typical level spacing in superconducting quantum devices based on Josephson junctions [92], but also to the range in which control electronics are readily available. Future implementations will probably allow the extension of the maximum frequency up to ~50 GHz [93]. Worth mentioning is the development of quantum non-demolition detectors for either cavity [10, 94] or itinerant [15, 16] photons, which require no absorption and preserve the photon number [2]. Superconducting transition-edge sensors operating as bolometers show sharp resistance increase upon the absorption of photons [95]. These devices typically work at frequencies above THz, but extensions at frequencies down to 90 GHz are in progress [93]. Additionally, superconducting hot electron bolometers are operated above 300 GHz [95]. Detection schemes based on opto-electro-mechanical systems using mechanical resonators with coupled microwave and optical cavities have also been theoretically proposed [96–98].

Photon detectors based on semiconductor quantum dots (QDs) have been proposed and realized for a wide range of frequencies (Figure 1.18). Single-photon detectors based on photomultiplication work at frequencies above 300 GHz (Section 1.3.3.1). Detectors based

on photon-assisted tunnelling have been reported for lower frequencies. Noise detectors were developed to investigate quantum noise excitations in quantum point contacts and they work in the 10 to 80 GHz frequency range. Given the single particle energy spacing in specific DQD devices, this upper bound can be significantly extended up to THz. In order to increase the sensitivity, it has been proposed to couple the DQD with a high-quality factor resonator (Section 1.3.3.5). In this case, the frequency range of the detector is determined by the characteristics of the resonator. Superconducting coplanar resonators are usually fabricated with fundamental frequency ranging between $\approx$ 100 MHz and 20 GHz. By employing shorter resonators, higher-order harmonics, or three-dimensional waveguide cavities, an extension of the maximum working frequency up to ~50 GHz can be envisaged.

1.3.3.1 *Detection of Sub-Millimetre Wave Photons by DQDs*

Semiconductor QDs have been tested as photon detectors at submillimetre wavelengths [99]. The first demonstration of single photon sensitivity has been achieved in the 300 to 600 GHz range by exploiting the transitions between Landau levels in GaAs/AlGaAs QDs in the presence of a high magnetic field [100]. Further experiments focused on devices in which a first dot is coupled to a planar submillimetre wave antenna and the second dot, capacitively coupled to the first, is electrically connected to external leads in order to work as single-electron transistor (SET) [101] (see Figure 1.19). The device essentially works as a photomultiplier. The absorption of photons at frequency ~500 GHz by the first dot determines telegraph-like switches of the conductance peaks of the DQD, which are acquired by dc conductivity measurements with timing resolution in the millisecond range, thus much lower than the response time of the DQD. The current responsivity of such a photon detector, being defined as the ratio between the measured current signal and the incident microwave power, results as $R = eG_{PC}\eta/\hbar\omega$, where G_{PC} is the photoconductive gain, i.e., the number of photoelectrons generated by each impinging photon, and $\eta < 1$ is the quantum efficiency [99]. Values of G_{PC} in the 10^5 to 10^{12} range have been reported for frequencies above 500 GHz, giving rise to values of R similar to what is obtained by conventional phototubes in optics [99]. To our knowledge, photomultiplication effects have not been reported below 300 GHz as in this range G_{PC} has typically unit value.

1.3.3.2 *DQD Noise Detectors*

The absorption of microwave photons in a QD gives rise to inelastic electron transitions that occur either between the electronic reservoirs in the leads and the energy levels in the single dot, or between the

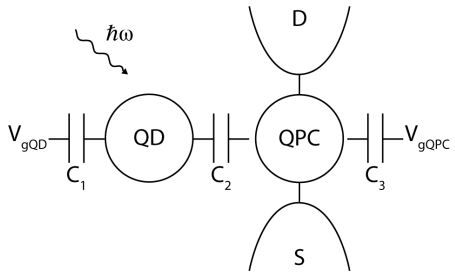

FIG. 1.19: Capacitively coupled systems made by two quantum dots (QDs)—or a QD and a quantum point contact (QPC)—are used to detect photon absorption events. In this scheme, the two systems are individually tuned by external gates. The left dot works as the absorber, the second device is tuned in a configuration where its conductance is strongly dependent on the electrostatic environment. The transition induced by the absorption of the photon results in a conductance change for the sensing (QPC) device. From reference [81].

DQD's discrete energy levels themselves. In general, these processes are reported as photon-assisted tunnelling (PAT) [77, 102–104]. PAT in QDs can be used to develop frequency-selective detectors of quantum noise, as demonstrated by means of quantum point contact (QPC) charge detectors [105–109]. These experiments showed the possibility to measure the photon absorption rate in a frequency range between 10 and 80 GHz with time-resolved measurements of the DQD conductivity [108, 109]. The working principle is sketched in Figure 1.20. The left and right dot levels are detuned in such a way that their energy separation (ε) matches the frequency of the incoming photons, while source-drain bias voltage (V_{SD}) is set to zero. When the QPC is polarized, it emits microwave photons by shot noise that are subsequently absorbed by the DQD, giving rise to PAT transitions from the left to the right dot with characteristic rate Γ_{abs}. The electron then relaxes back to the initial state with typical relaxation rate $\Gamma_{rel} = 1/T_1 \sim 60$ MHz. These "internal" transitions are too fast to be directly detected by the nearby QPCs (bandwidth 30 kHz), thus they are not visible in the measured time trace. However, as lead-dot tunnel coupling can be $\Gamma_l = 1$ kHz $\ll \Gamma_{rel}$ as in [108], an additional electron can occasionally enter and leave the DQD at a slower rate. In this case, such "external" transitions can be effectively detected by the QPC and the measured rates can be related to the internal DQD transitions, allowing the estimation of the photon absorption rate Γ_{abs} [108, 109]. With this protocol, the detector efficiency is proportional to the Γ_l/Γ_{rel} ratio and amounts to $\eta \sim 10^{-5}$ [109]. Fast detection circuits and improved DQD relaxation times are thus required in order to improve the efficiency of the detector.

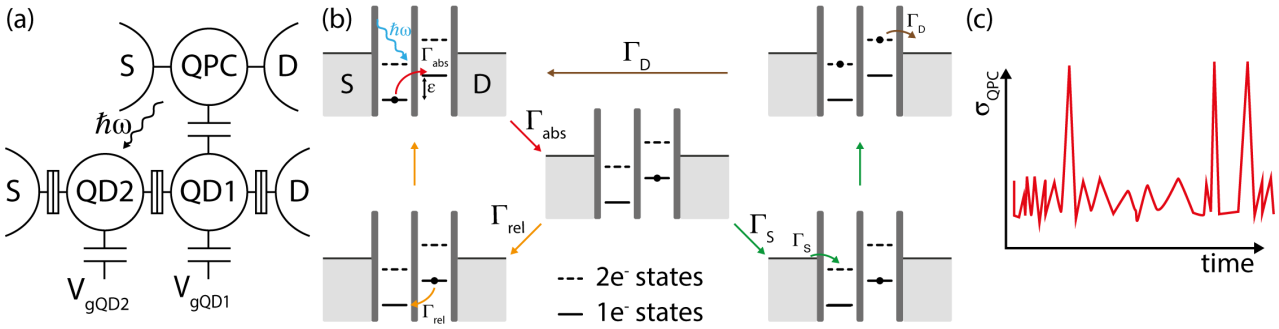

FIG. 1.20: (**a**) Noise detection scheme based on quantum dots (QDs). The quantum point contact (QPC), which is capacitively coupled to the double quantum dot, acts both as a source of microwave photons and as a charge sensor that probes the configuration of the DQD. (**b**) Scheme of the different paths that the DQD system can take after photon absorption. Γ_{rel} shows the relaxation path, where the electron returns to the ground state, emitting a phonon/photon in the process. Γ_S followed by Γ_D shows the charging with an additional electron through tunnelling from the source contact. In the two-electron state, tunnelling out of the device is permitted: this returns the system to the initial configuration. (**c**) Typical time trace of the detector signal. The peaks correspond to entering and leaving of the additional electron in the DQD. From reference [81].

1.3.3.3 *Charge Sensing of DQDs*

A fundamental aspect for the development of semiconductor detectors is the realization of fast charge sensors. A QPC or a SET capacitively coupled to the DQD can provide highly sensitive measurements of the source-drain conductivity [104, 110–112]. However, the measurement bandwidth of these devices typically has a high-frequency cut-off of less than 100 kHz due to the RC time constant of the cryogenic wiring and to the limited bandwidth of the current-to-voltage converter. To overcome these limitations, radio-frequency (rf) SET reflectometry was developed [113–118]. Fast and high-fidelity readout of the DQD is obtained by incorporating the charge sensor into an impedance matching tank circuit: changes to the electrostatic potential of the charge sensor alter its conductance and therefore generate measurable changes to the reflection coefficient of the circuit (Figure 1.21). As an example, charge transitions in few-electrons GaAs DQDs were resolved in single-shot measurements with an integration time of 100 ns and signal-to-noise ratio equal to 3 [80]. Rf reflectometry has been applied also on InAs nanowire [119–121] and Si/SiGe DQDs [122, 123].

As a possible alternative, gate reflectometry bridges the gap between cQED and rf reflectometry [124–127]. It makes use of lumped element sub-GHz resonators to probe changes in the tunnelling capacitance due to device configuration. These resonators are typically formed by an off-chip inductance (L) and a total capacitance (C) that is the result of parasitic and QD contributions. The dot tunnelling-dependent quantum capacitance [128] leads to a shift in the resonance frequency ($\omega_0 = 1/\sqrt{LC}$). The resonator is usually probed in the

dispersive regime, where the reflected signal experiences a phase shift, consistently with a cQED input–output approach. While being currently less performant than rf-SET in terms of fidelities and bandwidth [129], this technique has the advantage of requiring a simpler device design, as the resonator is connected directly to one of the gates defining the QD (with the highest lever arm possible in order to maximize the shift) instead of requiring an additional SET/QPC nearby.

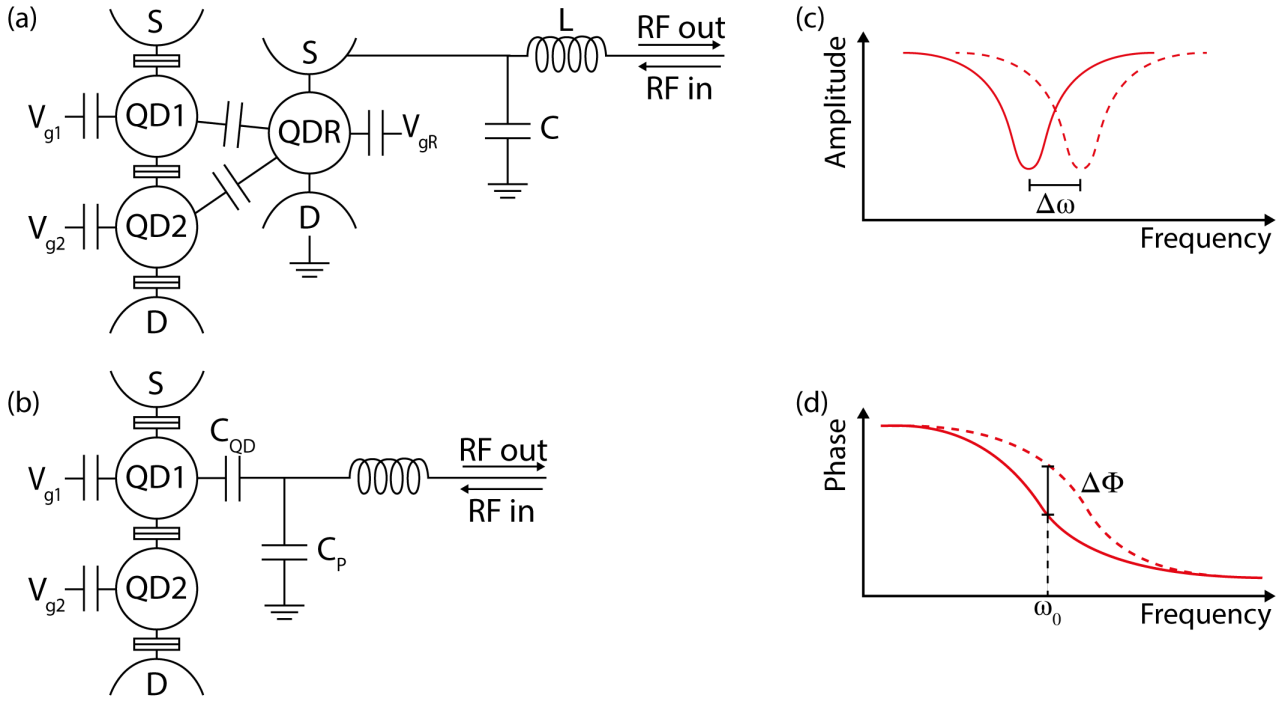

FIG. 1.21: Schematics of two different reflectometry techniques. Panel (**a**) shows the rf-SET setup. A read-out quantum dot (QDR) is capacitively coupled to the double quantum dot, with different couplings to each dot. The single-electron transistor (SET) is highly sensitive to the charge configuration of the DQD thanks to the sharpness of the tunnelling resonances. Configuration changes due to DQD tunnelling events result in a strong change in the SET conductance. This can be observed by monitoring the signal reflected by the resonating circuit. Panel (**b**) shows the gate reflectometry configuration. In this case, the resonating circuit is directly connected to one of the gates controlling the DQD. Tunnel coupling between the QDs determine a change of the quantum capacitance that can be resolved as a frequency shift of the resonating circuit. This approach results in a simplified and more compact device, but is less performant as a readout technique. In both approaches a bias tee can be used to dc bias the rf lines, so that they can provide a source-drain bias or configure the QD (substituting V_{gQD1} in this case). Panels (**c**,**d**) show the expected change in the reflected signal amplitude and phase in different configurations (dashed and non-dashed lines) for these readout schemes. From reference [81].

Full cQED approaches employing a superconducting resonator have been used, in a similar fashion to what is done with superconducting qubits, to perform dispersive readout of charge and spin states. In the dispersive regime, the phase response of the resonator is sensitive to the DQD configuration. When the DQD is far from transitions between (M, N) charge states, its characteristic energy is

typically orders of magnitude higher than the resonator frequencies and the two are far detuned. When the DQD is close to an inter-dot charge transition with energy slightly detuned from the cavity frequency, the dispersive interaction leads to a state-dependent frequency and phase shift. The same is true for spin states in presence of a magnetic field, when the resonator is detuned from a spin transition. More quantitatively, we consider a transition between DQD levels with frequency splitting ω_σ. When the DQD-resonator detuning $\Delta\omega = \omega_\sigma - \omega_0$ is $\Delta\omega > g_{c(s)}$, where $g_{c(s)}$ is the photon-charge (photon-spin) coupling strength, the phase shift at bare cavity frequency is $\Delta\phi = -\arctan\left(2g_{c(s)}^2/\kappa\,\Delta\omega\right)$, where κ is the cavity decay rate. This approach can be used to map the DQD stability diagram even if no bias is applied [130, 131], and therefore the leads do not need to be connected to an electron reservoir, similarly to gate-reflectometry. This technique was successfully used to perform qubit state read-out for charge qubits [132], spin qubits [63], singlet-triplet qubits [130], and exchange qubits [133].

1.3.3.4 *Detection of Microwave Photons by Conductivity Measurements*

The noise detectors described above can potentially be implemented also for the detection of itinerant microwave photons. For this purpose, DQDs are coupled to a transmission line providing the flux of impinging photons. In microwave spectroscopy of DQDs [77], this has been carried out by introducing a capacitor between one of the gate electrodes and the coaxial line. This approach can be considered widely tunable as the coaxial line allows broadband transmission of photons, whereas the DQD can be tuned in the selected detection window. For these applications, DQD devices with large single-particle excitation energies, such as those implemented in InAs nanowires [3, 56, 134, 135], appear particularly interesting for the possibility they offer to continuously tune the DQD levels from few GHz to THz frequencies.

Time-resolved detection of single PAT transitions requires sensitive and fast detection. QPCs would play this role but they are themselves source of microwave photons [106, 108]; in a photon detector this would increase dark counts unless the detection frequency is set beyond the cut-off frequency of the QPC noise generator [106]. Moreover, QPCs typically show a response much slower than the relaxation rate of DQDs. In this respect, rf reflectometry would perform better, given that charge sensing with bandwidth up to ~1.5 MHz [80] has been reported for GaAs and gate sensing with 1 μs integration time has been reported for InAs DQDs [127]. The reflectometry technique has been recently implemented also for Si/SiGe DQDs, demonstrating single-shot singlet-triplet readout with an integration time of 0.8 μs [123]. For Si/SiGe DQDs, the charge relaxation time was shown to vary over four orders of magnitude as a function of

detuning and interdot tunnelling parameters, with a maximum value $T_1 = 45\ \mu$s [136]. These results indicate that rf reflectometry can be implemented to sense the DQD at rates faster than the charge relaxation times, thus opening a way to the realization of efficient DQD based microwave photon detectors.

Coupling with acoustic phonons is strong in DQDs and represents the primary source of dark counts of the detector [137]. This effect is more pronounced in nanostructured DQDs, where strong electron–phonon coupling follows as a consequence of tight electronic confinement and characteristic phonon environment of the nanostructures [138, 139].

Due to the small size of dots (10–500 nm) compared to typical wavelength of MW photons (1–300 mm), their quantum yield, i.e., the efficiency to transduce MW photons to electrical signal, is generally low for bare QDs. To improve this figure of merit, coupling with resonators is a valid solution as we discuss in the following.

1.3.3.5 *Photon Detectors Based on DQDs Coupled to a Microwave Cavity*

Coupling to a Single Mode Resonator

cQED architectures with DQD devices embedded in a high-quality factor resonator have been investigated for the coherent manipulation of DQD charge and spin states [140]. Superconducting coplanar waveguide resonators have demonstrated high versatility for coupling two-level quantum systems to confined microwave fields [141]. They show fundamental frequency (ω_0) in the GHz range and internal quality factor (Q_{int}) reaching values above 10^6 for bare resonators fabricated with optimized procedures [142, 143]. The capacitive coupling to external transmission lines (Figure 1.22) gives rise to the external quality factor Q_{ext}. The loaded quality factor is given by $1/Q_L = 1/Q_{int} + 1/Q_{ext}$ and the photon decay rate is $\kappa = \omega_0/2\pi Q_L$ [144].

Experimental realization

Experimentally, the coupling between resonator and DQD is obtained by connecting the central conductor of the coplanar resonator to one of the DQD electrodes. Lumped-element low-pass filters can be introduced between the central conductor of the resonator and the dc voltage source in order to implement dc bias of the dot gate used for the coupling [145]. Values of DQD-resonator coupling (g_c) from a few MHz up to 200 MHz have been reported for different hybrid DQD-resonator devices. g_c is typically maximum for $\varepsilon = 0$ due to the strong electric dipole moment of the DQD at the charge degeneracy point. In order to maximize g_c, the resonator can be designed to achieve large zero-point electric field fluctuations ($\mathcal{E}_{rms}$). Being $\mathcal{E}_{rms} \propto \omega_0\sqrt{Z_0}$, different approaches have been reported to increase Z_0, including higher-impedance coplanar resonators [63], high-impedance resonators with SQUID arrays [61], or high-kinetic inductance NbTiN nanowire resonators [62, 133, 146]. The coupling of the spin degree of freedom requires presence of either spin orbit

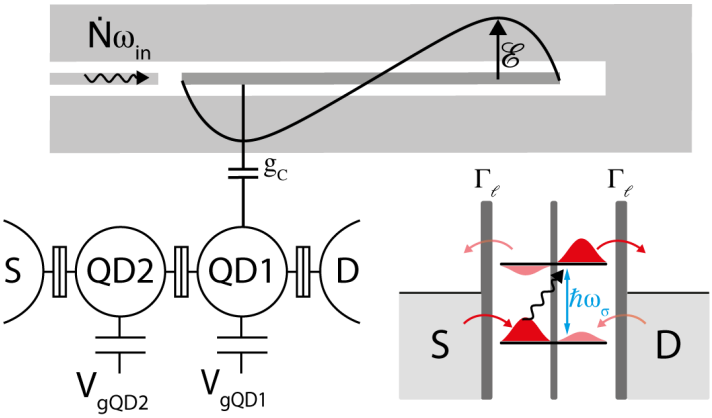

FIG. 1.22: Schematics of the hybrid DQD-resonator circuit. A transmission line with incident photon flux $\dot{N}\omega_{in}$ is capacitively coupled to a high-quality factor coplanar waveguide resonator that behaves like an ideal quantum harmonic oscillator, with low average photon occupation. The resonator is also capacitively coupled (g_c) to the DQD. The level spacing of the DQD can be tuned to match the resonator frequency. When a photon is absorbed, the excited electron can tunnel to the drain contact and be detected as a current flow. From reference [81].

interaction [57, 58, 130] or an inhomogeneous magnetic field [63, 147, 148], thus the spin coupling strength (g_s) can be an alternative to bare electrical g_c. The regime of strong DQD–photon coupling has been achieved with either charge ($g_c \gg \gamma_c, \kappa$) [60, 61, 132] or spin ($g_s \gg \gamma_s, \kappa$) [62, 63, 133] qubits.

The damping rates γ_c and γ_s are related to relaxation and dephasing of the DQD charge and spin state, respectively. A large variation of these parameters is reported for different DQD devices and materials [60–63, 130–132, 148–152]. Fluctuating electric fields affect both relaxation and dephasing rates in DQD charge and spin qubits. Electric field fluctuations could arise from different sources, including background $1/f$ charge noise, fluctuations in the gate potentials or other electrical noise sources [50, 153–155]. Dephasing in DQD charge qubits is more affected by charge noise for $\varepsilon \neq 0$. Conversely, for $\varepsilon = 0$, the DQD energy is insensitive to gate potential fluctuations ("sweet spot") at first-order [153]. Charge noise induced dephasing is proportional to the square of the total charging energy E_c^2, with $E_c = e^2/C_\Sigma$ [154], thus larger interdot capacitance, i.e., smaller interdot charging energy, is expected to reduce the effect of charge noise [132, 156]. Coupling to the phonon bath can also induce fluctuating electric fields as an effect of different mechanisms. Common to all semiconductors is the inhomogeneous deformation of the crystal lattice under the effect of the so-called deformation potential phonons, which alter the band gap in space and give rise to fluctuating electric fields. Additionally, in polar crystals, such as III-V semiconductors,

homogeneous strain leads to electric fields through the piezoelectric effect [50].

A microwave photon detector based on a DQD coupled to a microwave cavity has been recently theoretically proposed [68] and experimentally demonstrated.[157] The schematic diagram of the detector is shown in Figure 1.22. A flux of $\dot{N}$ microwave photons with frequency ω_{in} entering from a transmission line is stored in a single-port resonator with high-quality factor (Q_L) and frequency ω_0. In a DQD, in the case of weak interdot tunnel coupling (t_c), the electrons are strongly localized on the individual left dot ($|L\rangle$) and right dot ($|R\rangle$) states. Conversely, for larger t_c, the DQD can be described as a two-level system, whose eigenstates [77]

$$|g\rangle = \cos\frac{\theta}{2}|L\rangle - \sin\frac{\theta}{2}|R\rangle \tag{1.24}$$

$$|e\rangle = \sin\frac{\theta}{2}|L\rangle + \sin\frac{\theta}{2}|R\rangle, \tag{1.25}$$

are often referred as bonding and antibonding states. Their energy spacing is

$$\hbar\omega_\sigma = \sqrt{4t_c^2 + \varepsilon^2}, \tag{1.26}$$

where ε is the detuning energy, equal to the difference in the chemical potentials of the two dots, and $\cos\theta = -\varepsilon/\hbar\omega_\sigma$.

The DQD detector is appropriately configured near the charge transitions between the charge states $|L\rangle = |N+1, M\rangle$ and $|R\rangle = |N, M+1\rangle$, where $|N, M\rangle$ denotes $N(M)$ electrons in the left (right) dot. In the "pumping" configuration, with $V_{SD} = 0$ and non-zero detuning ($\varepsilon \neq 0$), inelastic PAT transitions lead to pumping electrons between the left and right dot, or vice versa, depending on the sign of ε, thus giving rise to a net source-drain current [77]. The spacing of the DQD levels is tuned to the frequency of the input photons ($\omega_{in} = \omega_0$) for $\varepsilon = \varepsilon_{res} = \sqrt{\omega_{in}^2 - 4t_c^2}$. Tunnel couplings are also appropriately tuned in order to ensure that the dot-lead tunnelling is faster than the DQD relaxation rate.

For symmetric dot-lead tunnelling with rate Γ_l, the photon-induced current $\langle\Delta I\rangle = \langle I - I_0\rangle$, where $\langle I_0\rangle$ is the current generated by dark counts for $\dot{N} = 0$, reads [68]

$$\langle\Delta I\rangle = -e\frac{\Gamma_l\cos(\theta)}{3}\Delta m_z. \tag{1.27}$$

Here, $\Delta m_z = m_z - m_0$ is the photon-induced polarization, being

$$m_0 = -\frac{\gamma_e + \Gamma_l}{3\gamma_1/2 - \gamma_e/2 + \Gamma_l} \tag{1.28}$$

the equilibrium polarization. $\gamma_1 = 1/T_1$ is the incoherent relaxation rate, where T_1 is the charge relaxation time, and γ_e is the phonon-induced spontaneous emission rate due to difference in excitation

and relaxation rates related to thermal phonons [68]. The effective depolarization rate results

$$\Gamma_1 = \gamma_1 + \frac{2\Gamma_l - \gamma_s}{3}, \tag{1.29}$$

while the transverse relaxation rate reads

$$\Gamma_2 = \frac{1}{2}(\gamma_1 + \Gamma_{0e}) + \gamma_\phi, \tag{1.30}$$

where Γ_{0e} is the incoherent tunnelling rate to the lead. The dephasing induced by low-frequency $1/f$ charge noise (γ_ϕ) is also included to quantify its contribution to Γ_2.

The detector efficiency, defined as $\eta = |\langle \Delta I \rangle|/e\dot{N}$, has been calculated by optimizing the reflection of input photons at the resonator port [68, 158]. The reflection is minimized when the decay rate of the resonator (κ) matches the DQD-mediated photon dissipation rate

$$\kappa = \frac{2[g_c(\varepsilon_{res})]^2 |m_z|}{\Gamma_2(\varepsilon_{res})}, \tag{1.31}$$

where $g_c(\varepsilon_{res}) = g_0 \sin\theta_{res} = 2g_0 t_c / \sqrt{4t_c^2 + \varepsilon_{res}^2}$. When this condition is valid, the detector efficiency becomes

$$\eta_{res} = |\cos\theta_{res}| \frac{2\Gamma_l/3\Gamma_1}{1 + 2\dot{N}/|m_0|\Gamma_1}. \tag{1.32}$$

In the optimized condition, obtained by combining the parameters $t_c/h = 0.5$ GHz, $g_0 = 50$ MHz, and $\kappa/2\pi = 76$ kHz, the calculated efficiency is $\eta \approx 98\%$ even in the presence of strong DQD dissipation [68], but in the current experimental realization the measured efficiency was $\eta = 6\%$.[157]

Part II

EXPERIMENTAL TECHNIQUES

2 FABRICATION

2.1 NANOWIRE GROWTH

Many techniques for the fabrication of nanostructures exist, with different approaches available in order to obtain spatial confinement along multiple dimensions. Here we focus on InAs/InP nanowires, which can be grown by metal-assisted chemical beam epitaxy. In this process Au nanoparticles (with typical dimensions in the 30-100 nm range) are deposited on a III-V semiconductor substrate oriented along the [111] direction. In the growth chamber mettalorganic precursors are introduced: tributyl-arsine for As, trimethyl-indium for In, tributyl- phosphate for P [51, 53, 56]. The constituents of the semiconductor diffuse inside the nanoparticle and form crystal planes below it. This process leads to the formation of nanowires, with a diameter related to the size of the nanoparticle. Growth rates are controlled by flux, pressure and temperature in the chamber, which are also critical to obtain nanowires without planar defects and a constant radius. Typical nanowire lengths attainable are in the 1-3 μm range. Atomically sharp interfaces between InAs and InP can be obtained by changing precursor flux in the chamber.

2.2 OPTICAL LITHOGRAPHY

Optical lithography is a technique where a photosensitive material, "resist", is selectively exposed to light (typically ultraviolet) to design a pattern, that is then transferred to the target material. Many different resists exist, most are based on polymeric chains dispersed in a solution. The coating on the sample is often done with a spin coater: the resist is deposited in the middle of the sample, which is then spinned at speeds of 1000-6000 rpm. During the rotation the solvent evaporates which leaves behind a mostly uniform layer. The exposition to light can either break or cross-link the polymeric chains, which determines if a resist is "positive" or "negative". In the development step the sample is submerged in a specific solution. Broken chains are much more soluble and are selectively removed, exposing the sample only in the wanted regions.

In optical lithography the whole device is flooded by UV-light from a special purpose source. A transparent mask (glass or quartz) with chromium patterns blocks the light where needed. This makes the exposure very fast, since it is done in parallel for the whole device, but has limited flexibility since every time a new pattern has to be

FIG. 2.1: SEM picture of nanowires as grown on a substrate. Insert shows a Scanning Transmission Electron Microscope image of a nanowire, with the gold seed nanoparticle visible on top.

implemented a new mask is needed. Mask-less solutions, where a laser beam is directed to sequentially expose the resist, also exist and allow for faster prototyping.

The use of light means that the resolution of this technique is fundamentally limited by diffraction effects, which emerge when the feature size is comparable to the light's wavelength. In standard conditions the actual resolution limit is $\sim$1 μm. In the semiconductor industry special purpose high energy ultraviolet sources, with smaller wavelength, are used to reach resolutions of $\sim$4 nm at the time of writing.

2.2.1 *Etching*

Two main etching processes are applied in micro and nano-fabrication: dry and wet etching. The latter consists in wetting the sample in a liquid (typically a base or an acid) that etches the material [159]. This approach is relatively easy and fast to apply, but has some drawbacks. Some etching solutions are not very selective, they might also attack the resist or other material. Furthermore, the etching is isotropic and therefore often leads to an undercut: the material below the resist is also etched. This severely limits the resolution attainable because of the low control over this effect.

Dry etching techniques usually employ a plasma to etch the material. In this work a Reactive Ion Etching (RIE) machine was used. In a RIE a radiofrequency field between two electrodes excites a very low pressure gas (5-20 mTorr) , ionizing it. In a plasma the electrons are much more mobile than the ions because of their low mass. They are able to travel enough within each cycle to charge the chamber walls and the sample. This charging creates a DC bias (in the order

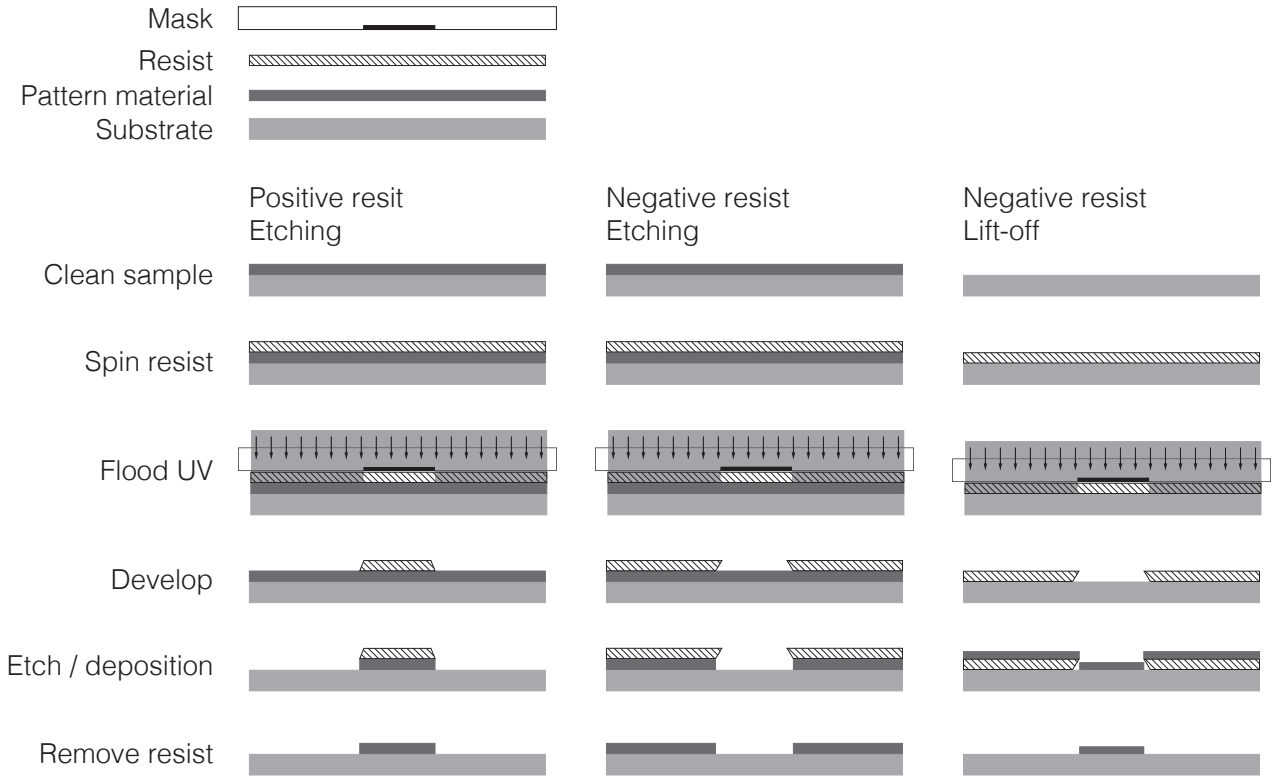

FIG. 2.2: Schematic representation of the three most common lithographic procedures. The same mask leads to different final results (in terms of negative or positive of the initial design) depending on the resist and procedure used. Lift-off with a positive resist is not displayed here, because it requires an additional layer to provide sufficient undercut for the lift-off to be successful.

of hundreds of volts) that accelerates the ions in the plasma towards the sample. These ions are the ones that etch the sample[160]. The etching can be purely physical, meaning that the ions induce sputtering, which works on any material but is very slow and not selective. But it can also be reactive, when a gas mixture is used that reacts chemically with the sample to improve the etch rates substantially. This kind of process is anisotropic since the ions impinge mostly from above, but is affected by loading effects and the re-deposition of the etched material. Loading effects can be particularly challenging in the fabrication of very small features: the etching rates depend both on the size of the etching region and on the density of the patterns. [161] Another complication of this technique is that if a purely physical etching with a noble gas is used, the very low etch rates have to be compensated by using high parameters (in particular high RF power consequently high DC bias). This leads to the degradation of the resist film, which then becomes difficult to remove.

2.2.2 *Lift-off*

In this work the only material deposition process for lift-off used is thermal evaporation of gold. Thermal evaporation is obtained by placing the sample in a high vacuum chamber ($< 5 \times 10^{-5}$ Torr). A high current is driven through a tungsten holder, which heats up enough to evaporate the metal. Evaporation rates and total thickness are monitored by a calibrated quartz crystal microbalance (typical rate of $\sim$1 Å/s and thickness of 100 nm). A thin (10 nm) adhesion promoting layer is usually evaporated before the Au with the same technique. Th materials of choice being titanium for adhesion on Sapphire and titanium or chromium on silicon substrates. The evaporation chamber provides the possibility to heat the substrate ($\sim$ 400°C) during the evaporation. This is particularly useful for the evaporation of Au: a high substrate temperature promotes the formation of an ordered film, with larger single crystal islands[162]. The impact of the improved film quality on the transport characteristics is not noticeable from the testing performed, but a high quality film results in much more robust wire bonding connections. One downside of this procedure is that the high temperatures are not compatible with lift-off procedures because of resist degradation. The high temperature evaporation was therefore used in combination with etching in order to fabricate the bonding pads, and not for all successive steps. An increase in the island size is expected [162] also by baking in vacuum the already deposited gold contacts, but no difference in the bonding strength was observed in this case.

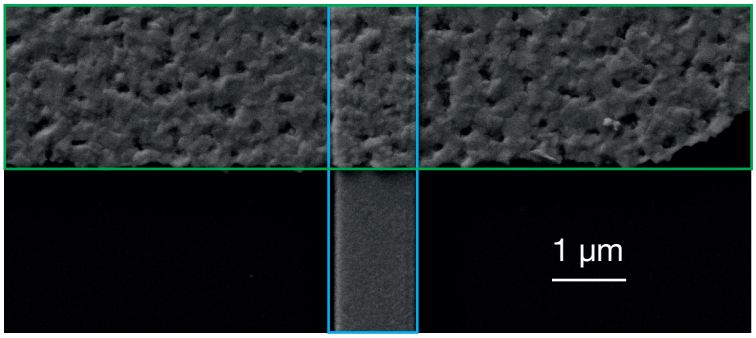

FIG. 2.3: Comparison of the grain texture for gold evaporated at 400°C (green) and 25°C (blue). The two (partially overlapping) areas were evaporated at different stages of the fabrication process.

The lift-off process requires that the film is discontinuous along the pattern lines (see Fig.2.2) in order for the unwanted material to separate cleanly. Some mechanical stimulation (as provided by ultrasound baths or a solvent flux) might help in the case of a partial discontinuity, but might also lead to tearing of the pattern. The discontinuity is usually obtained by having a thick resist film with some degree of undercut. The resist thickness is mostly determined by the spin

coating rotation speed and must be much higher than the deposited film thickness (the lowest ratio between resist over deposited material used in this work was 2:1). The undercut is easily obtained by using negative photoresists, with a varying degree that depends on the pre-bake temperature, the exposure, and the developing procedure. Positive photoresists tend to develop an over-cut instead (both are visible in Fig.2.2), which results in a continuous film. Lift-off process can still be implemented with a positive photoresist by using a sacrificial layer underneath it, which can be developed to provide the desired undercut. The most used electronic resist is PMMA, which is a positive resist. But in this case the undercut is provided by both the forward and backscattering processes (section 2.3.1).

2.3 ELECTRON BEAM LITHOGRAPHY

In order to fabricate smaller features than the 1 μm typical of photolithography, Electron Beam Lithography (EBL) can be used. This technique employs a resist which is sensitive to electrons, meaning that the electrons break or cross-link the polymeric chains. By precisely controlling an electron beam to draw the wanted pattern, the resist is exposed and all of the usual steps (development, etching or lift-off) can be performed similarly to what is known from photolithography. This technique can reach very high resolutions (10-20 nm [163]) and is very flexible: since it does not require a mask, changes in the device design require just a modification of the exposition CAD. But it also has some drawbacks.The resist film thickness is typically lower than the optical ones, therefore some processes are more constrained (like etching). The pattern area is small (200×200 μm is the area used for most of this work), unless specific and costly tools are used. But most importantly, the exposition is sequential: the electron beam is driven to sequentially expose every point of the pattern. Therefore his process is not suitable for large scale manufacturing where the processing speed of photolithography provides a strong advantage.

2.3.1 *Scanning Electron Microscopes*

Two main types of devices exist for EBL. Specialized systems have beam energies in the 100-120 kV range (the effect of the beam energy on the results is discussed later) and are capable of patterning bigger areas. Much more common are Scanning Electron Microscopes (SEM) that can also be controlled by an external pattern generator. These have electron energies in the 0.2-30 kV range and can be also used for imaging. The instrument used for this work belongs to the latter category: a Zeiss R Sigma SEM equipped with a Schottky field emitter

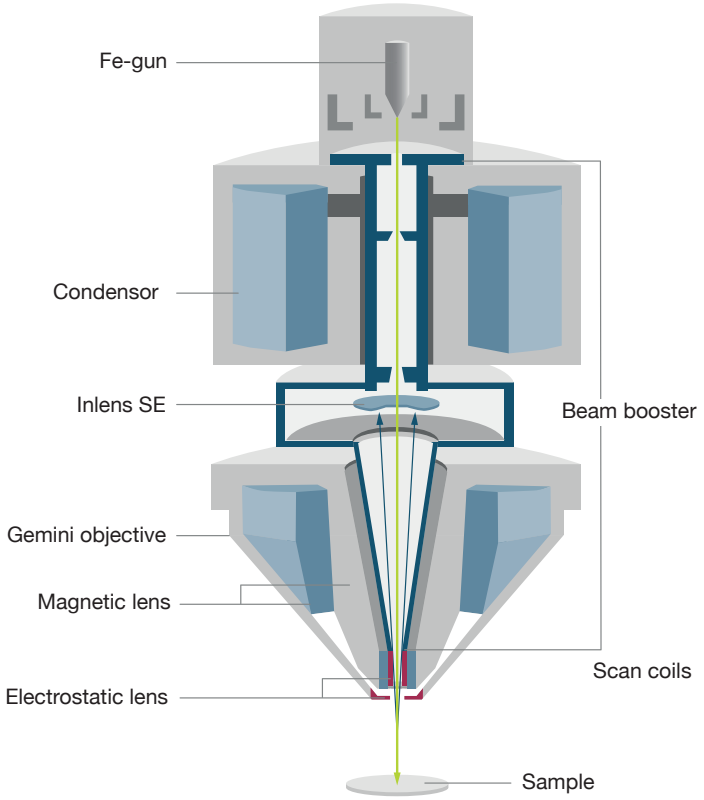

FIG. 2.4: Scheme of a Zeiss Sigma Gemini 1, similar to the device used in this work.

and a Raith Elphy Quantum pattern generator. The main component of a SEM are:

- An electron source, with Field Emission Guns (FEG) being the best in terms of beam characteristics (brilliance, energy and emission spread). They are formed by a cathode and some potentials which extract the electrons from it.
- Several systems of magnetic lenses that focus the beam. At the sample position the beam is ideally focused in a single spot. In practice a spot size <10 nm can be obtained at best focusing conditions.
- An accelerating potential that determines the electron's kinetic energy when they impinge on the sample. This in turn has drastic consequences on the interactions with it.
- Scanning coils, that quickly move the beam in order to raster the sample.
- One or more detection systems, that collect electrons emitted from the sample and use their signals to form an image. The

most common ones are secondary and backscattered electrons, which provide information about the morphology and the composition respectively.

2.3.2 *Electron-Solid interactions*

A detailed description of all of the parameters that can be controlled during a lithographic process is beyond the scope of this work. But the most relevant ones can be understood with a simplified picture of the electron-matter interaction, thus providing an understanding of the main limiting factors in this technique. When high energy electrons impinge on a solid many interactions can happen that alter the path of the electrons: inelastic and elastic scatterings, generation of x-rays, generations of secondary electrons to name few. The most interesting ones here are the scattering events. These change the trajectory of the electrons and (for the inelastic ones) their energies. Each electron undergoes several scattering events until they have lost all of their initial kinetic energy. As a result of this and the high number of electrons in the beam we get a pear shaped interaction volume. The higher the energy the further into the solid the electrons manage to travel, leading to an elongated and bigger interaction volume (Fig.2.5).

In the context of the resist exposure, what is most relevant is the distribution of forward and backward scattered electrons [164]. Forward scattered electrons are those that originate from the impinging beam. They are relatively confined in a cone with the tip at the top of the resist layer, and they pose a strict limit to the maximum resolution achievable with EBL: even if the electron beam is focused to a single point, the net effect is the exposure of a finite area because of forward scattering. Backscattered electrons are electrons that come from the substrate, possibly as a result of multiple backscattering events. They are much more spread than forward scattered ones, and as such they are typically the factor that actually limits the resolution in realistic conditions. Their impact can be drastically reduced by using high accelerating potentials (Fig.2.5) or by using very thin, suspended samples, so that most of the electrons are transmitted in the vacuum below. These two factors can be modelled by two different Gaussian profiles of exposition [164] and at least partially compensated by proximity correction techniques [165, 166].

Among the different phenomena that happen in the interaction volume we have the generation of secondary electrons. These can be broadly classified as all electrons with low energy (< 50 eV). These electrons can be collected by an external potential, and their number used as a signal for the formation of an image while rastering the sample with the electron beam. Because of their low energy they have a very short mean free path in the solid, therefore the

collected signal is mostly originated very close from the surface and the information they provide is morphologic. Another response that is often collected is the current of backscattered electrons that manage to escape the sample. Since the backscattering efficiency strongly depends on the atomic number of the sample, the information they provide is compositional, even if they cannot be used to determine exactly the composition of the sample.

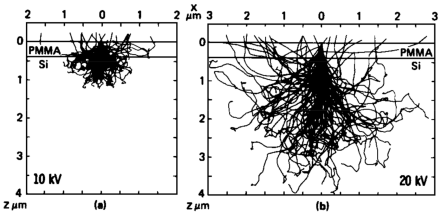

FIG. 2.5: Monte Carlo simulations of 100 electron paths in PMMA on Si, with different electron accelerating potentials (10 and 20 kV respectively). Taken form [167]. The interaction volume changes drastically, with the higher energy having also a much bigger interaction volume. This counterintuitively improves the resolution of the exposition. In the higher energy case most of the interaction volume is deep into the Si, where it doesn't expose the resist. The paths trajectories in the PMMA are mostly concentrated in the close proximity of the beam incidence point. Even if some of the electron trajectories in the PMMA are much further from the origin in the 20 kV case, they are much less dense. Therefore they do not expose the resist enough to lead to noticeable development.

2.4 FABRICATION OF DEVICES WITH NANOWIRES

The end result of the nanowire growth process is a substrate with a nanowire "forest" (Fig.2.1). The nanowires can at this point be transferred on a substrate by a micro-manipulator [168], but the most consistent and quick approach is to disperse them in an isopropanol solution and drop cast them on a pre-patterned sample. Once the nanowires are deposited on the substrate they get strongly attached thanks to the strength of van der Waals forces in nanoscale objects. The result of this is visible in Fig. 2.6.The nanowire position can then be observed at the SEM. At this point a normal lithographic procedure is performed. The resist is deposited and exposed as usual, with the exposition pattern previously prepared in order to match the exact position of the device. In this step the alignment of the pattern and the nanowires is fundamental, since the contacts are usually very close (down to 100 nm). The precise alignment is allowed by the use of Au markers fabricated by EBL. After the development a short oxygen plasma treatment is used to remove the remaining resist residue on the nanowires. Thermal evaporation of $\sim$ 100 nm of gold and lift-off form the connection from the nanowires to the pre-patterned pads for wire bonding. To obtain a good ohmic contact

between the semiconductor and the gold, a passivating step with a NH_4S_x solution [169] is needed to etch the surface oxide that forms as a result of exposure of the nanowires to air.

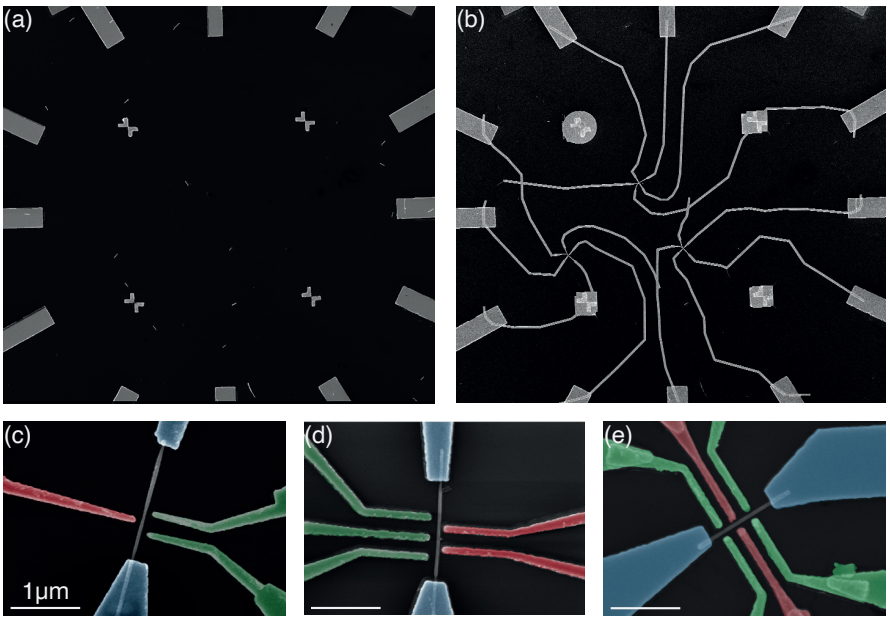

FIG. 2.6: SEM images of the 200×200 μm region where contact fabrication by EBL is performed. (a) shows the region with deposited nanowires. Alignment markers and already fabricated contacts are visible. (b) shows the same sample, with final contacts to the nanowires now fabricated.(c,d,e) Different gate configurations that where tested. The fabrication happens always in a single step. thus simplifying the process significantly with respect to other approaches.

2.5 SUPERCONDUCTING RESONATORS

The chosen superconducting material for the fabrication of coplanar resonators is $YBa_2Cu_3O_7$ (YBCO), a high temperature superconductor (critical temperature of $\sim$ 90 K in the tested samples). This material presents several advantages:

- the high critical temperature extends the working range of the device,
- the superconducting resonators obtained are resilient to the magnetic field [170],
- the technology chain of this material is well known by the group in Modena.

The superconducting coplanar resonator have been fabricated by optical lithography starting from commercial (Ceraco GmbH) 8 × 5 mm Au(200 nm) / YBCO(330 nm) / sapphire(430 μm) multilayer films. Excess Au and YBCO regions were etched by argon plasma in

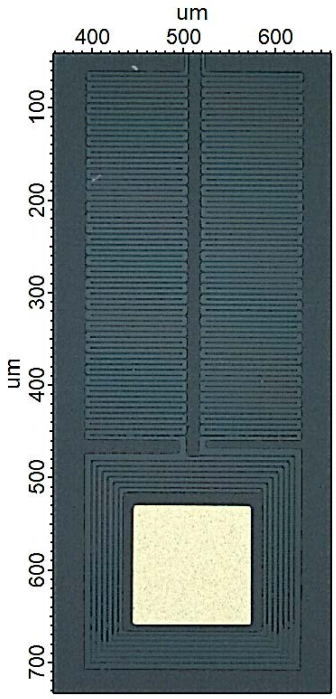

FIG. 2.7: Optical microscope image of a fabricated low-pass filter, displaying high resolution patterning of YBCO over a wide area, obtained through optical lithography and RIE etching.

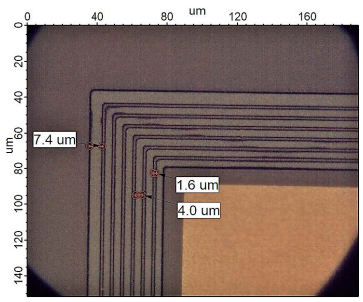

FIG. 2.8: Detail of a fabricated YBCO pattern, showing the resolution attained in this fabrication procedure.

a reactive ion etching (RIE) chamber. In this process, gold pads were defined on top of the YBCO film in order to serve as wire bonding spots and used either to link the coplanar launchers to the external feedlines or for grounding connections. Additional leads and pads (eight per each slot) for dc measurements were fabricated by lift-off of thermally evaporated Au(100 nm)/Ti(10 nm)/sapphire films. The dry etching in a RIE has the advantage, with respect to alternative wet etching processes, of avoiding exposure to water which affects the superconducting properties of YBCO. Furthermore, this technique allows a very high spatial resolution in the patterning; we fabricated devices with feature sizes down to 1.6 μm through optical lithography with good reproducibility, as visible in figures 2.7 and 2.8

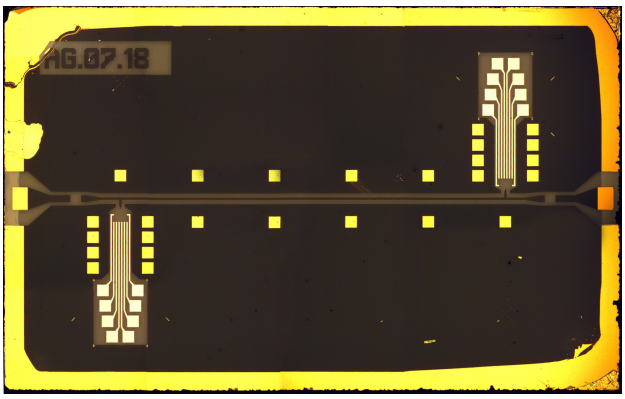

FIG. 2.9: Optical microscope image of one of the fabricated coplanar resonators. Size of 8×5 mm.

2.6 STATISTICS: RATE OF SUCCESS & OPEN ISSUES

Out of a total of 367 nanowire devices, ∼200 were fabricated by me in Modena and ∼160 in Pisa. Of the ∼ 300 which were successfully fabricated, about 150 worked properly, with a success rate that increased in time as a results of improvements in the fabrication process. The most significant improvement in the success rate was the introduction of the high temperature evaporation of gold for the pre-patterned contacts. This increased significantly the success rate during the bonding process, which is still the cause of most device malfunctions. Finally, the introduction of a long pre-cooling bake in high vacuum improved significantly the nanowire conduction, as is visible in Figure 2.11.

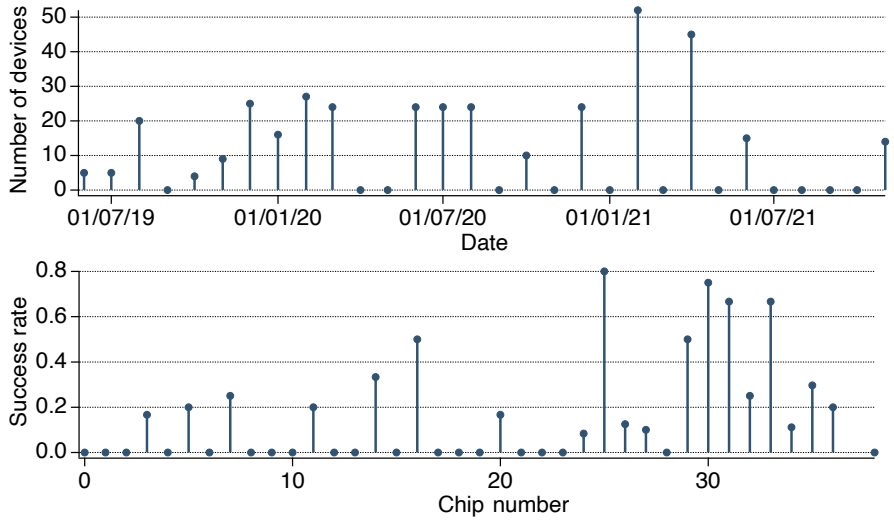

FIG. 2.10: Plot of the number of nanowire based devices fabricated and tested over time and the success rate in the fabrication process for each chip fabrication.

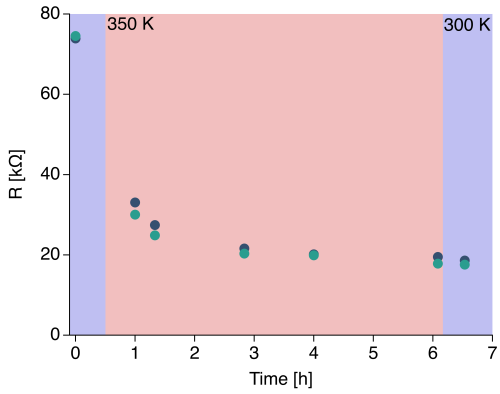

FIG. 2.11: Resistance monitored during bake time in high vacuum of two InAs nanowire devices. While keeping the device under high vacuum we heat up the sample to 350 K in order to evaporate all humidity from the devices. After the 3 hours mark we stop observing significant changes in the device resistance.

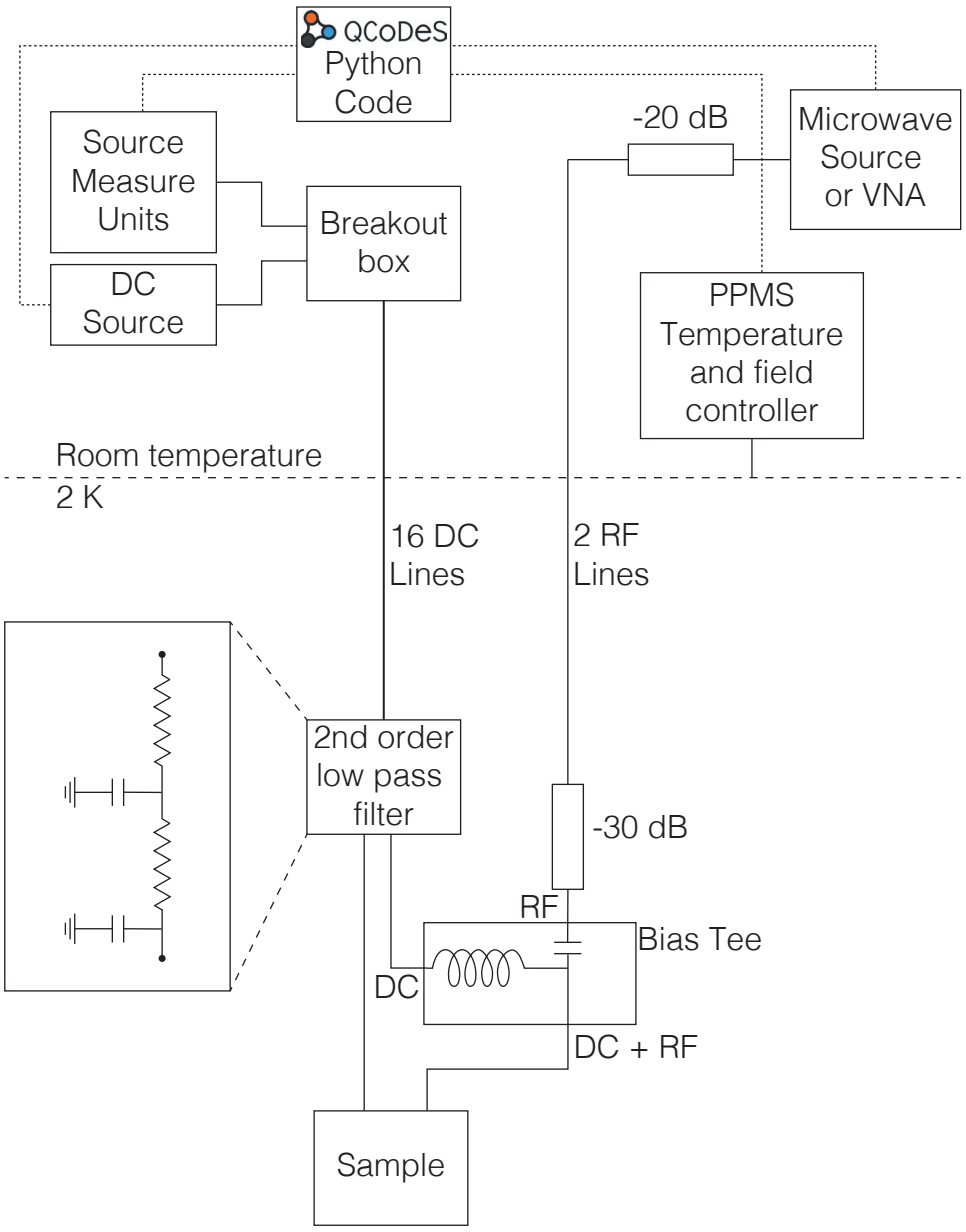

FIG. 2.12: Schematic sketch of the experimental setup. The functionality of each component is explained in the following.

3

EXPERIMENTAL SETUP

In this work two classes of characterization are presented: DC transport and microwave spectroscopies. The former can further be split in room temperature (300 K) and low temperature (from 300 mK to < 300 K). In this chapter we will discuss the setup used, the improvements that I introduced and the control over the devices for data acquisition.

3.1 PROBE STATION

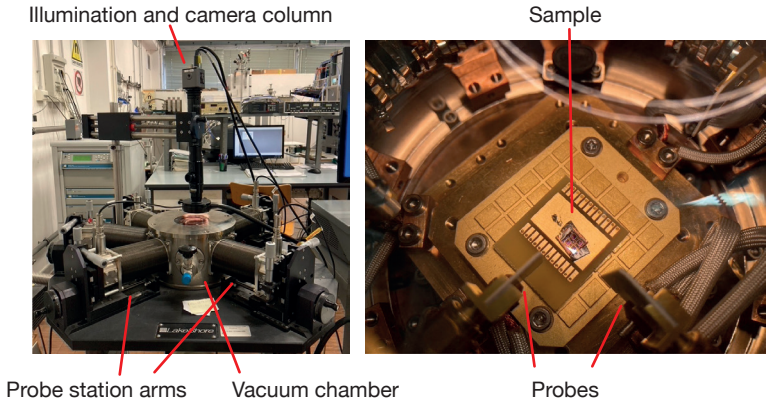

FIG. 3.1: Picture of the probe station and of the sample inside of it.

A probe station is a system formed by a vacuum chamber, an imaging system and several probes. The latter are formed by a small metallic tip attached to an arm which can be moved along three axes. The tip is electrically connected to an external Source Measure Unit and they are used to form temporary connections on the device under test. The imaging system is needed in order to locate the gold pads used for the electrical connection itself, while the vacuum chamber is needed since the tested nanowires are sensitive to the environment they are placed in. The strength of this system relies in the possibility of testing many devices without resorting to the wire bonding, which is a slow and error prone process. Furthermore, the used probe station allows the cooling of the devices through a liquid nitrogen flux and a temperature controller. In this work the probe station is employed mostly for the preliminary characterization of the devices, to check the success of the fabrication process and the selection of the best candidates for long measurements in a cryostat. The device used is a LakeShore PS-100 equipped with 3 arms, used for source, drain and gate contacts.

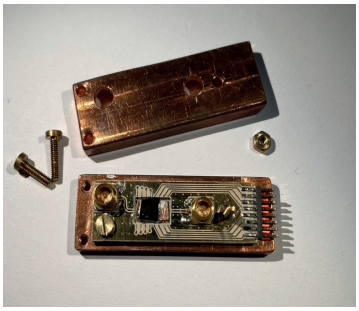

FIG. 3.2: Picture of the sample holder and its cover.

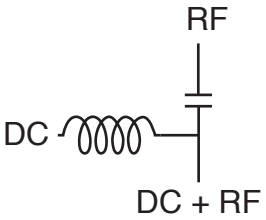

FIG. 3.3: Circuit of a bias tee.

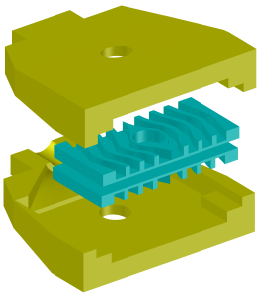

FIG. 3.5: Render of the 3D printed housing used for the DC connectors. Size 14.5×14×11 mm

3.2 SAMPLE HOLDER

A common ingredient of all cryostat operation is the sample holder, shown in figure 3.2. This sample holder, build in house, combines 16 DC contacts (through a pin connector) and 2 RF lines through SMP connectors. It can house samples up to 5×8 mm and is completely shielded through the copper lid. In certain experiments a modified version of this samples holder was used, which housed also surface-mount 10 pF capacitors along the RF lines, and a 1 μH ceramic inductor along one of the DC lines. By using these devices we define a bias tee (Figure 3.3) which allows us to combine RF and DC signals onto the same contact. While the inclusion of these component does induce additional losses, they can be easily accounted for thanks to the knowledge of the transmission spectra shown in Figure 3.4.

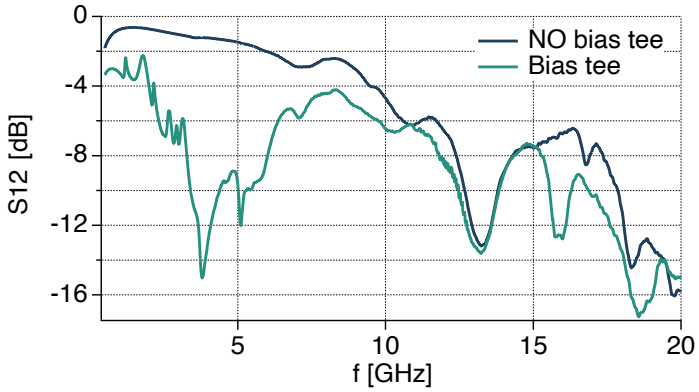

FIG. 3.4: Frequency dependent transmission across the sample holder RF lines, comparing the standard sample holder to the one with the bias tee.

3.3 CRYOMAGNETIC SYSTEM

The Physical Property Measurement System (PPMS) by Quantum Design, shown in Figure 3.6 is the cryogenic system in which most of the low temperature measurements reported here were taken. It features a 2-400 K working range, a 7 T superconducting magnet and accessories that implement several characterization techniques: electric transport, magnetometry, thermal measurements and many others. I this work an additional, in house built, probe was used. Fitted with 2 coaxial lines and 16 low thermal conductivity wires for cryogenic application, it allows simultaneous microwave spectroscopy and DC transport measurements. A cold section of the probe, marked in figure 3.6 by the DC filters, can house attenuators that greatly increase the thermalization of the coaxial lines' core, as well as as second order low pass filters for all of the DC lines, which shield the devices from high frequency noise and assist in the thermalization of DC wires. The vacuum chamber is fitted with a cryopump for

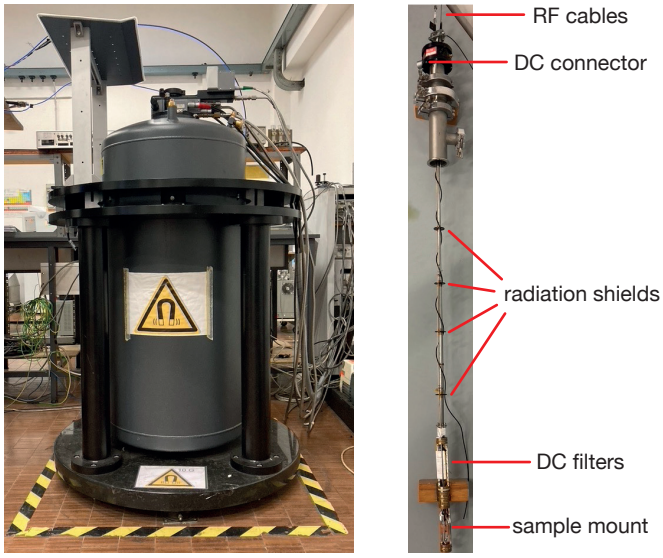

FIG. 3.6: PPMS and the in house built insert for DC + RF characterization.

high vacuum, but is usually operated with a $\sim$ 4 mBar pressure of helium, which facilitates cooling by acting as a thermal exchange gas. Radiation shields fitted along the probe help reduce the thermal load due to irradiation form the probe head.

3.4 HELIOX

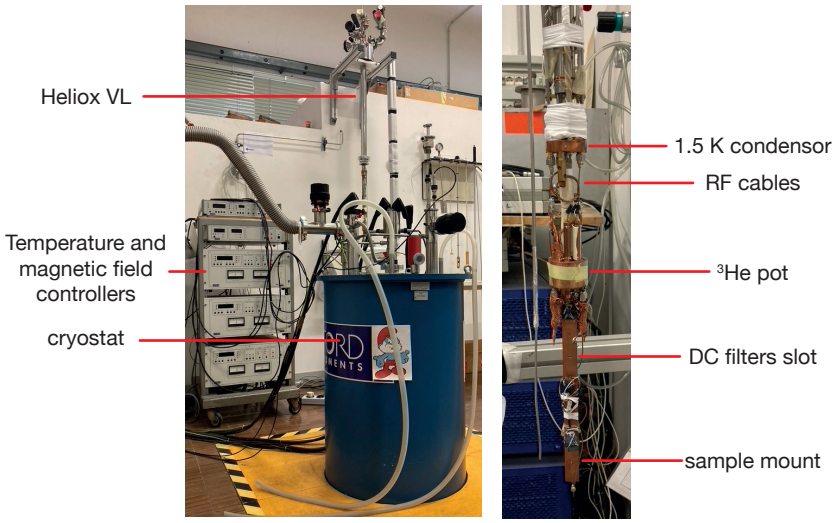

FIG. 3.7: Oxford Heliox VL, showing both the cryostat, the external electronics that control the temperature and the magnetic field. To the right the final part of the Heliox is visible, with certain components and the connections with their thermalization stages.

The Heliox VL by Oxford is a cryogenic system that exploits ^{3}He in order to reach temperatures of $\sim$ 350 mK. Furthermore, it's equipped with a triaxial set of superconducting magnets (9, 1, 1 T respectively)

that allows vectorial control over the field direction. This instrument is wired similarly to the PPMS described before, but the lower temperature needs more stages of thermalization in order to reduce the thermal load on the cold finger. It was used to explore phenomena at temperatures < 2 K.

FIG. 3.8: Keithley 2636 Source Measure Unit.

3.5 LOW NOISE ELECTRONIC SETUP

In order to perform DC transport measurements on nanostructured devices a very low noise setup is needed. 4 sets of Quad-twist wire by LakeShore, with 2 sets of twisted wires each, that have very low thermal and good electrical conductivity as well as low noise pickup, were used in all cryogenic conditions. For the low temperature filtering a second order, low pass RC filter with surface mount components was realized in order to fit in the limited available space on the probe. On the probe head an in house built breakout box was used for the handling of the connections. A Keithley 2636 Source Measure Unit (shown in figure 3.8) was used to source and measure voltages (0.1 mV - 200 V) and currents (0.1 pA- 100 mA). It combines two separate channels and is usually employed for the source-drain connectivity and the backgate voltage, thanks to the high voltage ranges available. For other gate operations the stabilized auxiliary DC sources of a Stanford Research SR830 lock-in amplifier were used.

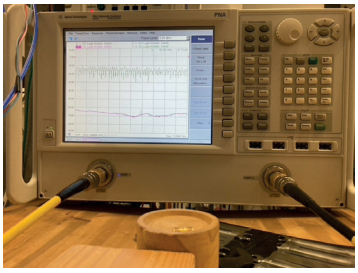

FIG. 3.9: Vector Network Analyser (VNA) N5222A by Agilent Technologies .

3.6 MW GENERATORS AND CIRCUITS

The main tools of the microwave spectroscopy used in this work are: a vector analyser, a microwave source, a MW amplifier and several attenuators. The high frequencies are affected by significant electrical losses in typical electrical cables. Therefore high frequency coaxial cables, fitted with SMA connectors were employed in the whole setup. The Vector Network Analyser (VNA) N5222A by Agilent Technologies was used for the S parameter characterization of the setup in the 10 MHz to 26.5 GHz range: it allowed us to measure the losses and reflections of the setup. The Anritsu MG3692b microwave generator was used as the source of continuous microwave radiation at fixed frequency (0-20 GHz) and power (-20 to 10 dBm). Several attenuators were used to both decrease the input MW power when needed and to thermalize the coaxial cables in the cryostat. An amplifier, cooled by liquid nitrogen, was used for amplification of the highly attenuated signal in combination with the VNA for some experiments.

FIG. 3.10: Logo of the QCoDeS package.

3.7 COMPUTER INTERFACE

The control over the instrumentation was performed with python code using the QCoDeS [171] package. This package provides the

drivers for many of instruments and modules for the data acquisition and to manage the database for the storage of the data. On top of this I had to update many drivers for my specific need, write new ones for instruments that were not supported and new routines for the data acquisition and handling. The data acquisition process is typically performed with a jupyter notebook, a software that couples the use of python code with tools for annotations, which has the advantage of creating an automatic log of all of the operations performed during the data acquisition.

Part III

EXPERIMENTAL RESULTS

4

EXPERIMENTAL RESULTS ON INAS NANOWIRES

This chapter reports the performance of InAs nanowire FETs as microwave detectors in the 1-10 GHz range. The first section describes the devices' design and reports their characterization through transport measurements. The the MW response is investigated, measuring some key figures of merit such as the responsivity (R) and Noise Equivalent Power (NEP). Finally the dependence of the response from several parameters parameters is reported, such as the device carrier density, temperature and radiation frequency.

4.1 DEVICES AND THEIR GEOMETRIES

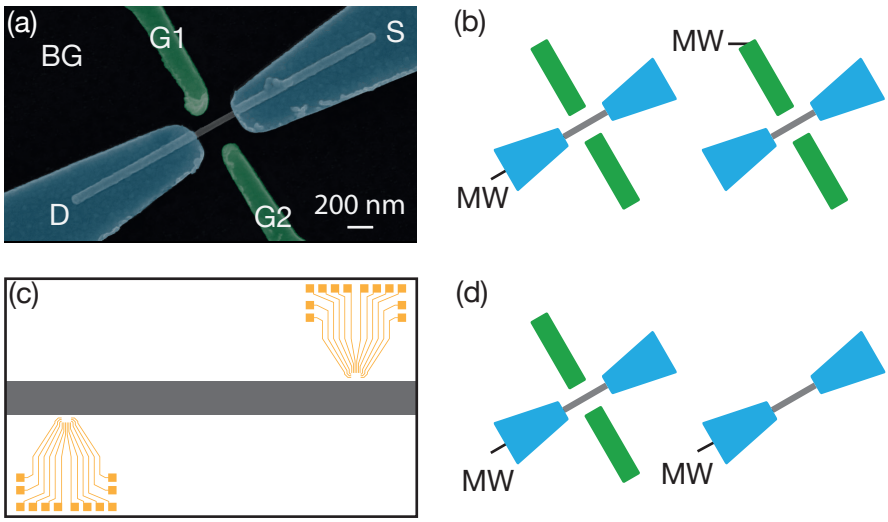

FIG. 4.1: Direct coupling devices: (a) False color SEM image of one of the tested devices, source (S), drain (D) and sidegate (G1, G2) contacts. A backgate voltage (BG) can also be applied. (b) Different MW injection configurations used for devices on SiO_2/Si substrates. Microstrip coupling: (c) NW arrangement close to Ag microstrip. The NW are contacted by using the pre-patterned Au/Ti contacts visible in the bottom left and top right corners of the device. (d) Device geometries tested in the microstrip configuration, in terms of gating and NW-microstrip connection. In this configuration only MW feeding to the S-D contacts was tested. The only difference between the two cases is the absence of the sidegates in one device. The leftmost configurations of (b) and (d) are identical: the microwave connect in both case to S-D, this is a direct comparison between the direct and microstrip coupling architectures.

In this chapter two main device classes are considered: direct coupling and microstrip coupling, as shown in figures 4.1 and 4.2. These

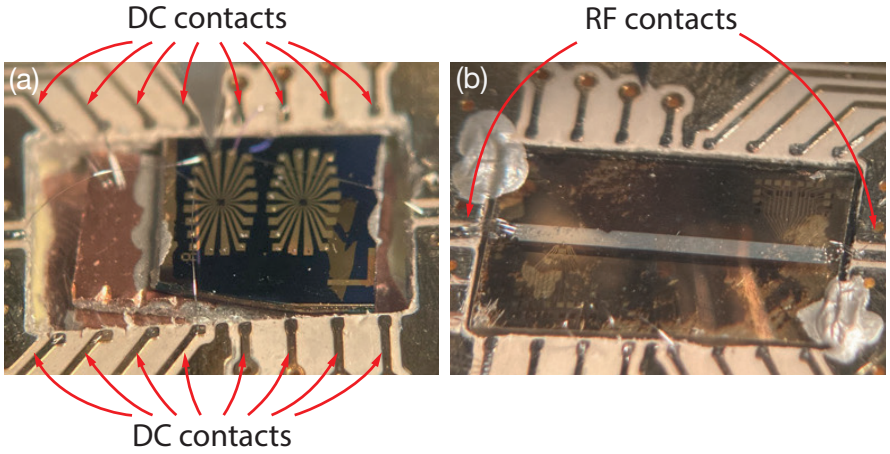

FIG. 4.2: Pictures of the two device classes tested, in their sample holder: (a) Direct coupling (dark blue), (b) Microstrip coupling. In both pictures it is possible to distinguish the DC contacts (above and below the chip) and the coaxial RF lines for MW spectroscopy (left and right).

two classes are distinct in the connections made in order to feed the microwave signal and the choice of substrate material. The latter was a direct consequence of the microwave feeding method chosen. The direct coupling devices were fabricated on SiO_2/Si substrates, with microwave feeding through direct bonding either to a sidegate or to source-drain contacts. This geometry presents several advantages: the fabrication process has high yield, since it employs the most widely used substrate and gate architectures for nanowire devices. Furthermore, the Si substrate can be used as a backgate, which is capable of fully depleting and saturating the carrier concentration in undoped InAs nanowires. The main drawback of this geometry is the limited control over the MW circuitry: it is not possible to design miniaturized metallic microstrip or coplanar waveguide lines on the Si substrates. The opposite is true for microstrip configuration. The fabrication process requires additional steps in order to define the microstrip itself and the insulating sapphire substrate complicates the electron beam lithography. Nanowire gating is in this case limited to two sidegates, which cannot be biased with voltages as high as those used on backgates, limiting the control over the nanowire conductivity. But the microstrip allows a more precise characterization of the MW response. The use of this architecture was important in validating the results concerning the dependence of the response from the radiation frequency. In this case, silver was preferred to superconducting materials, allowing detection also at room temperature.

In the the microstrip devices sapphire was used as a substrate for the fabrication of both the nanowire FETs and an Ag microstrip on the same chip. In these devices the microstrip is kept grounded through a bias tees and is connected to one side of the nanowire, acting as a source electrode. In the direct coupling devices, the substrate material

is highly doped Si with a 300 nm surface layer of SiO_2. This insulate the doped Si, which acts as a backgate, from the device. The presence of this dielectric allows us to explore a wide voltage range (typically $-60\ \text{V} < V_{BG} < 60\ \text{V}$) without risk of dielectric breakage. In the microstrip devices the only gating available is though sidegates (such as those visible in figure 4.1), with typical gate-nanowire distances in the 150-300 nm range. The usable range in this case is limited to $-15\ \text{V} < V_{SG} < 15\ \text{V}$. This kind of gate can be used to apply a transverse electric field [53, 56].

In this section I report the measurements performed on 10 nanowires fabricated on 4 different chips. Within these 10 devices, different microwave feeding approaches (see figure 4.1), different substrates and gating solutions were tested. While the results differ slightly across devices, for example in the strength of the response, the features and trend described in the following are general and reproducible.

The nanowires come from 2 separate batches, both of nominally undoped InAs, with radius ranging in the 40-55 nm range. The two batches behave similarly and do not shown any systematic difference in the transport features or the microwave response. The distinction between the two batches is therefore dropped in the following, except for the reference in table 4.1. The nanowires were fabricated in a FET configuration, as shown in figure 4.1: drain and source contacts were connected to a Source Measure Unit (SMU) which allows to sourcing and measurement of voltages and currents across the device. In all but one of the devices two sidegates are present in order to control the FET resistance. Table 4.1 contains a summary of device characteristics, such as batch, gate configuration and geometries.

MW feed	Gating	Batch	Diameter	DS distance	R(300K)	Code	Fab. at
Direct - DS	BG & SG	6763	46 nm	370 nm	14 kΩ	42 Cnw1	Mo
Direct - SG	BG & SG	6763	40 nm	400 nm	18 kΩ	41 Cnw2	Mo
Direct - SG	BG & SG	6763	40 nm	370 nm	17 kΩ	41 Cnw3	Mo
Direct - SG	BG & SG	6763	42 nm	550 nm	32 kΩ	41 Anw4	Mo
Direct - DS	BG & SG	6763	44 nm	560 nm	100 kΩ	41 Anw1	Mo
Direct - DS	BG & SG	6763	53 nm	540 nm	26 kΩ	41 Anw2	Mo
Direct - SG	BG & SG	7793	51 nm	400 nm	29 kΩ	44 Bd1	Mo
Direct - SG	BG & SG	7793	-	460 nm	14 kΩ	44 Bd2	Mo
Microstrip - DS	None	7793	-	300 nm	12 kΩ	47 Rd2	Mo/Pi
Microstrip - DS	SG	7793	-	-	12 kΩ	47 Rd1	Mo/Pi

TABLE 4.1: Summary of some features of the devices characterized in this chapter. DS stands for Drain-Source, BG for backgate, SG for sidegate.

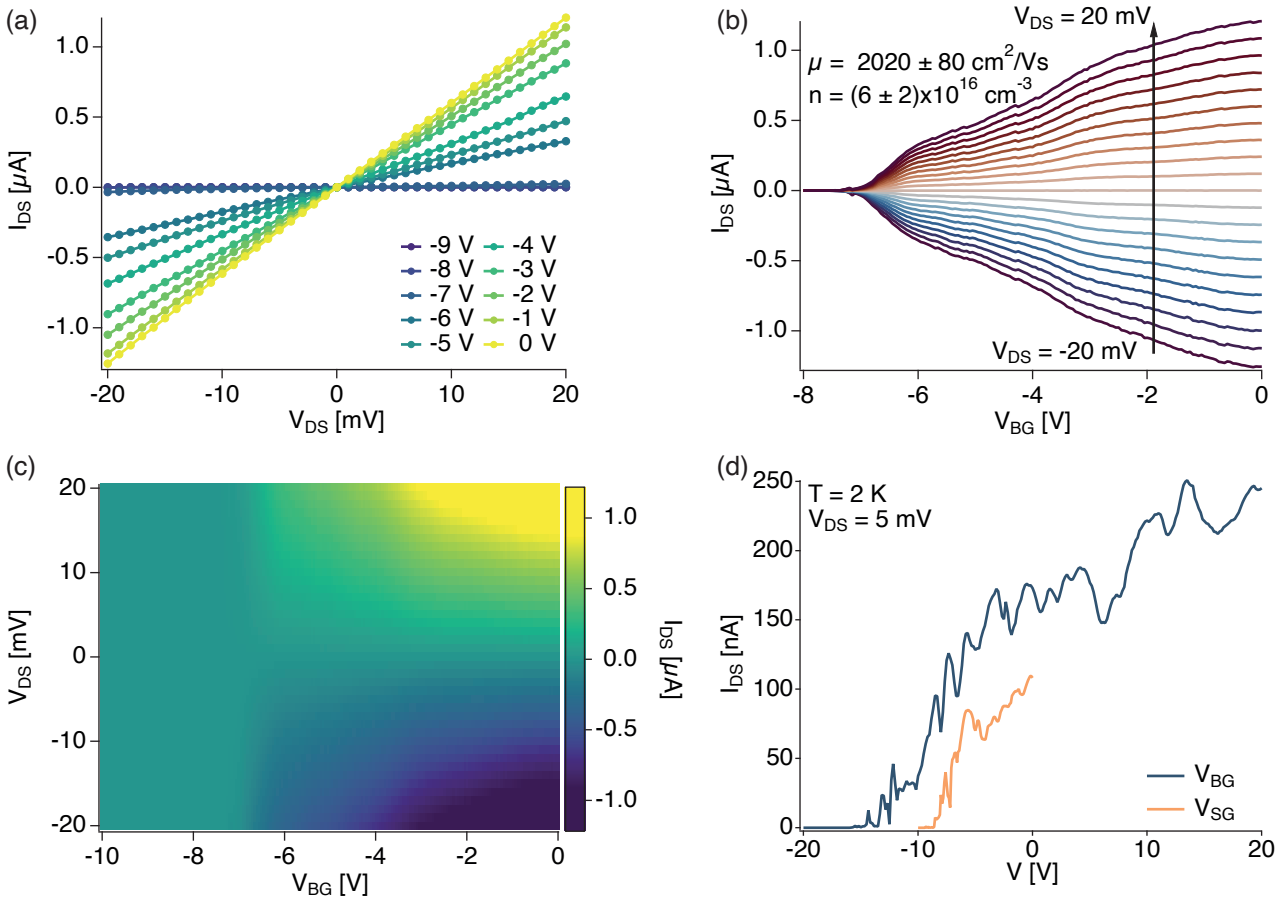

FIG. 4.3: (a) IV curves measured at selected V_{BG} values for a typical NW FET device (47 Rd2), cooled to 50 K. (b) Transconductance curves for the same device, from which the mobility and intrinsic carrier densities are extracted. (c) Colour map of the current as a function of V_{BG} and V_{DS}. (d) Transfer curves showing the effect of using the backgate V_{BG} or two sidegates in parallel ($V_{SG1} = V_{SG2}$) on the same device.

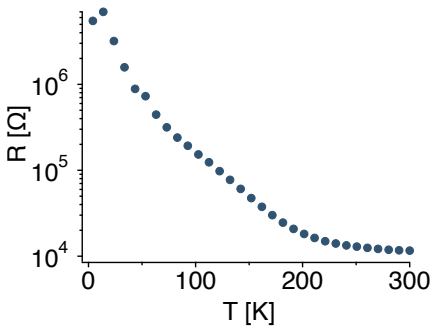

FIG. 4.4: Resistance as a function of the temperature for one the of the measured devices (47 Rd2).

4.1.1 *Nanowire FET characterization*

In this section the electrical characterization of the mentioned devices is reported. The fundamental feature of a Field Effect Transistor (FET) is that it behaves like a variable resistance as a function of an external electric field, generated by a so called gate electrode. The electric field is used in order to open or close the passage of electrons, reducing the number of carriers in the device and affecting the conductivity (figure 4.3.a). Figure 4.3 (b) shows a transconductance plot: the current is measured, at fixed drain-source bias V_{DS}, as a function of the gate-source voltage V_G.

Figure 4.3(d) shows the transfer current while sweeping either two sidegates in parallel $V_{SG} = V_{G1} = V_{G2}$, or the backgate V_{BG}. The lever arms of the two gates can be similar, leading to comparable modulation of the device conductance. The backgate has two advantages: a wider range of gate values can be explored, and a simplified model allows an estimation of the carrier mobility from a simple transfer current curve. At the same time, the backgate cannot be used to feed the MW radiation to a single nanowire.

Figure 4.4 shows the temperature dependence of the resistance, at $V_{BG} = 0$: as the device is cooled the thermal occupation of the conduction band decreases, leading to an increase in resistivity. In cold devices the gates are also more efficient in tuning the carrier density, resulting in increased transconductance and pinch-off threshold voltage, as visible in figure 4.5.

Calculation of the mobility

The dependence of the current from V_{DS} and V_G is fundamental in order to estimate some key properties of our devices, namely the mobility and the carrier density. The mobility in a FET is given by:[172]

$$\mu = \frac{gL^2}{CV_{DS}} \tag{4.1}$$

where $g = \mathrm{d}I_{DS}/\mathrm{d}V_G$ is the linear part of the transconductance, L is the channel length, C is the gate capacitance, $V_{DS(G)}$ the already mentioned drain-source (gate-source) voltages. For a sidegate configuration the determination of the gate capacitance is not a trivial task, that typically requires finite element simulations of the electrostatic system. For a backgate, the simplified model of a metallic cylinder (the NW) parallel to an infinite metallic plate (the doped Si of the substrate) yields a gate capacitance per unit length:

$$\frac{C}{L} = \frac{2\pi\varepsilon_0\varepsilon_r}{\cosh^{-1}\left(\frac{t}{R}\right)} \tag{4.2}$$

Where t is the distance of the metallic plane from the center of the cylinder (thickness of the SiO_2 layer) and R is the NW radius. An effective $\varepsilon_{r,eff} = 2.2$ [172] is used to take into account the fact that

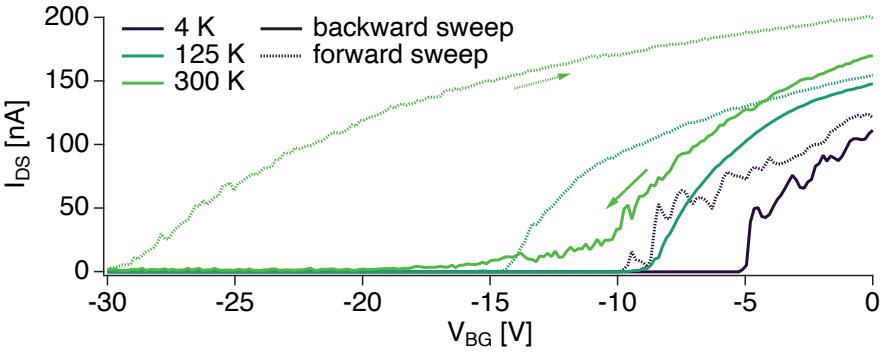

FIG. 4.5: Transconductance plots at selected temperatures highlighting the hysteresis of the transport features at different temperature. Here we may notice how also the hysteresis changes dramatically as a function of the temperature. Results from device 44 Bd1.

the nanowire is not embedded in SiO_2. With the knowledge of the mobility, it is then possible to determine the average field-effect electron density from the conductivity $\sigma = n\mu e$, where n is the electron density and e is the electron charge. While a single transconductance curve is in principle sufficient to determine the mobility, it is usually best to measure a map of the current as a function of both V_{DS} and V_G. The mobility is then calculated by taking the maximum of g as a function of V_G, repeating this for each V_{DS} and averaging the results. The electron density n is then calculated by determining the conductivity σ from the fitting of I_{DS} vs V_{DS} at the gate value corresponding to the previously determined maximum of g. The mobilities measured typically range in the $300 - 500$ cm^2/Vs with one case of 2020 ± 80 cm^2/Vs. The electron densities were determined to be in the $6 \times 10^{16} - 5 \times 10^{17}$cm^{-3} range, depending on the device. All of these values are commonly observed for undoped InAs nanowires.

Hysteresis

Graph 4.5 show two transfer curves for each temperature value: one for forward and one for backward sweeping. These terms define the acquisition of the transconductance curve while changing the V_G from lower to grater values for forward and vice versa for backward sweeping. The curves acquired with the two approaches are never identical. This hysteresis depends mostly on the temperature, gate sweeping rate and range; this is explained in the literature [173] as a result of charge traps, which strongly affect the electrostatic environment in a 1D nanoscale device. This effect is not investigated in further detail here, since it does not influence the results except for the introduction of a small uncertainty on the position of the pinch-off.

4.2 MICROWAVE RESPONSE

This section describes the phenomenology of the microwave detection, its dependence on the gate voltages and the procedures performed in order to determine the voltage responsivity R_V. The data reported in this section mainly comes from the device 42 Cnw1, but similar results were obtained from all devices. In all of the previously described measurements the standard approach consists in sourcing a bias V_{DS}

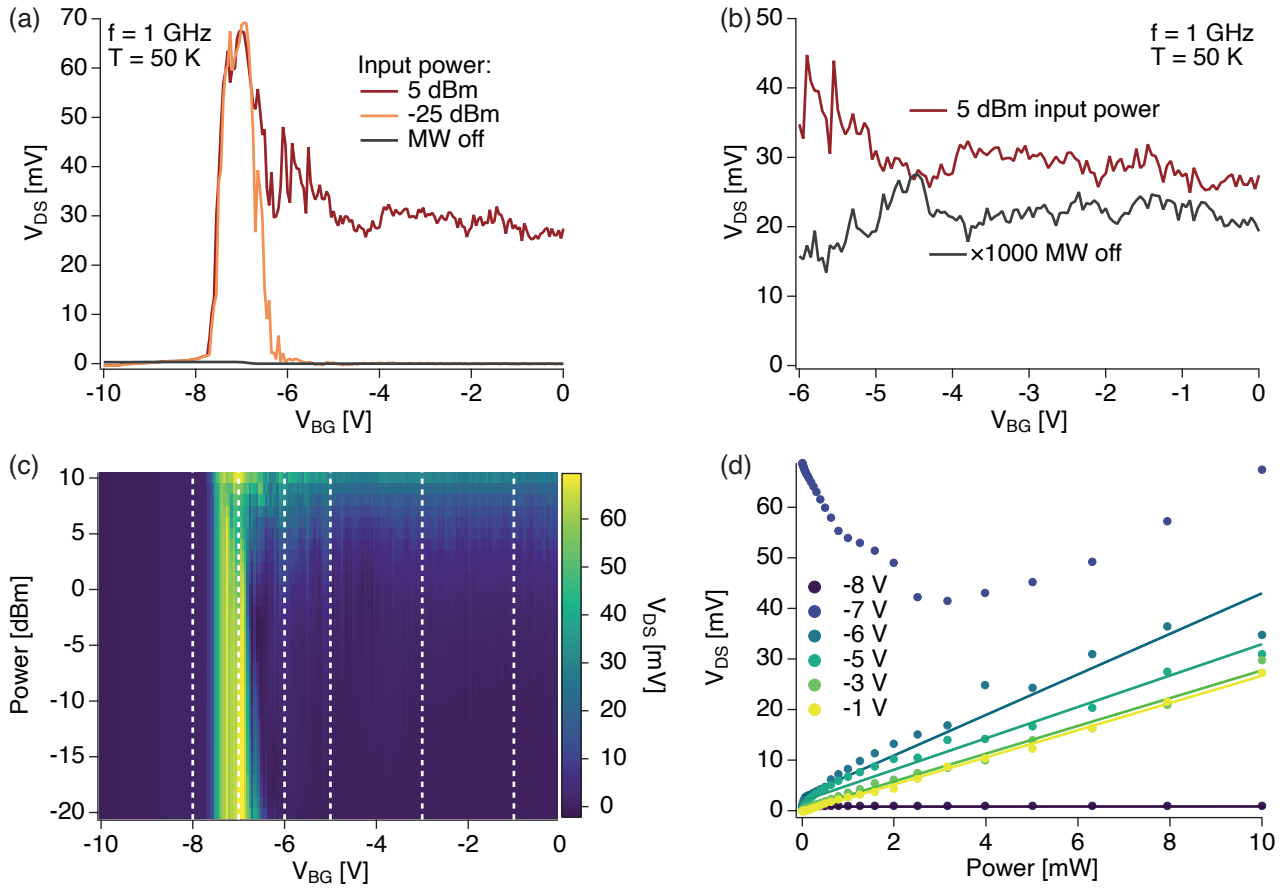

FIG. 4.6: (a) Measured V_{DS} bias as a function of V_{BG} for two different MW powers and with the MW source turned off. (b) Details of the difference between the measured V_{DS} with microwaves on or off. A difference of more than $\times 1000$ is observed. (c) Colour map of V_{DS} as a function of the backgate V_{BG} and the MW incident power. (d) selected curves along the dotted lines in (c). Linear fits highlight the dependence of the measured signal from the incident power. Results from device 42 Cnw1.

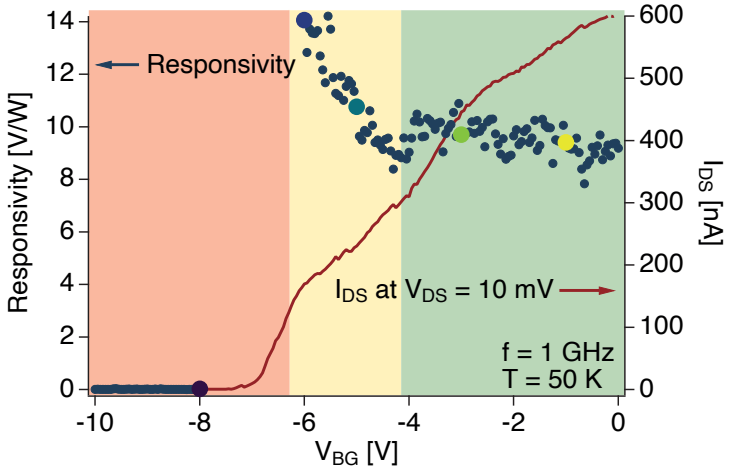

FIG. 4.7: Plot of the responsivity R_V, obtained from the map in 4.6(c), calculated as the slope of the V_{DS} vs incident power curve for each V_{BG} step. The transconductance curve highlights how the operation configuration begins just above the pinch-off. The green, yellow and red shaded regions mark the operation boundaries discussed in the main text.

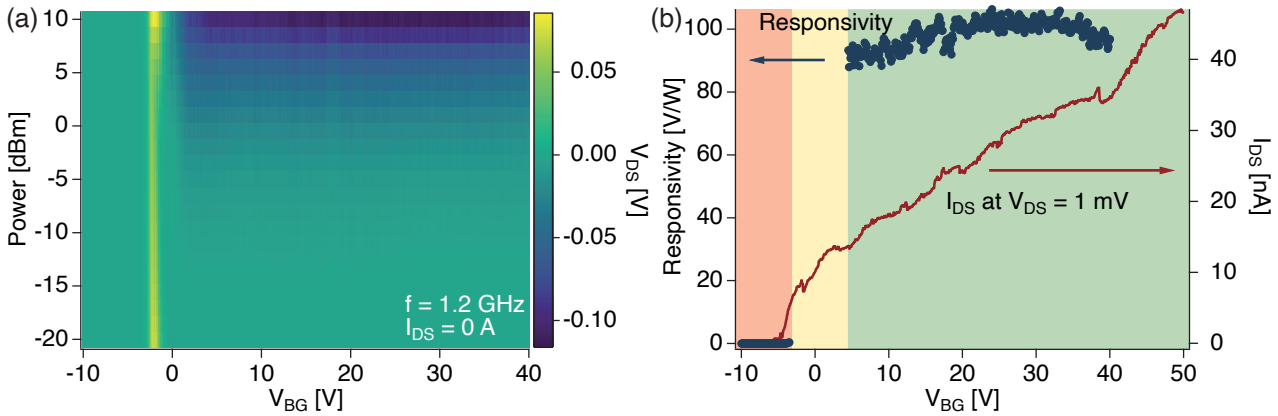

FIG. 4.8: (a) Colour map showing the measured V_{DS} as a function of V_{BG} and incident MW power. (b) Responsivity curve obtained from (a). Results from device 41 Anw2, to highlight the reproducibility of the obtained results and showing that the flat detection region extends up to high V_{BG} values. 4.7.

and measuring the resulting I_{DS} current through the device. The MW rectification signal is typically measured instead by operating the SMU in voltmeter mode while keeping $I_{DS} = 0$.

Regimes of operation

Two MW feeding configurations were tested, defined as asymmetric (when feeding to the source-drain contacts) and symmetric (when feeding to the sidegate), as illustrated in figure 4.1. We consider initially the source-drain configuration. Figure 4.6 (a,b) shows a direct comparison of the measured signal with microwaves turned on and off. For $V_{BG} > -6$V the measured voltage is flat and reproducible. The fact that this signal is constant with respect to the gate voltage implies that the device operation is resilient to small instabilities of V_{BG}. For $-7 < V_{BG} < -5$ V, close to the pinch-off, a strong, rapidly changing with the gate voltages signal is measured. Below the pinch-off the device is not conductive and no signal is observed (alternatively a flat, power independent, voltage might be present in this "open circuit" condition). The green shaded area in figure 4.7 defines the high electron density device operation configuration for this nanowire. The pinch-off gate voltage varies from device to device, therefore the minimum operation voltage must be determined on each one.

Determination of the responsivity

Here the procedure used in order to determine the dependence of the responsivity from any parameter is described, taking the gate voltage as an example. A 2D map of points is measured, where both the gate voltage and the MW input power vary. Figure 4.6(c) shows an example of such maps. For each V_{BG} the measured response as a function of MW power is plotted. From the linear fit of these curves the slope is extracted, that corresponds to the responsivity. The responsivity is a figure of merit which quantifies how strong response is for a given input power.

In the calculation of the responsivity the incident power on the device, and not simply the output power of the MW source, was

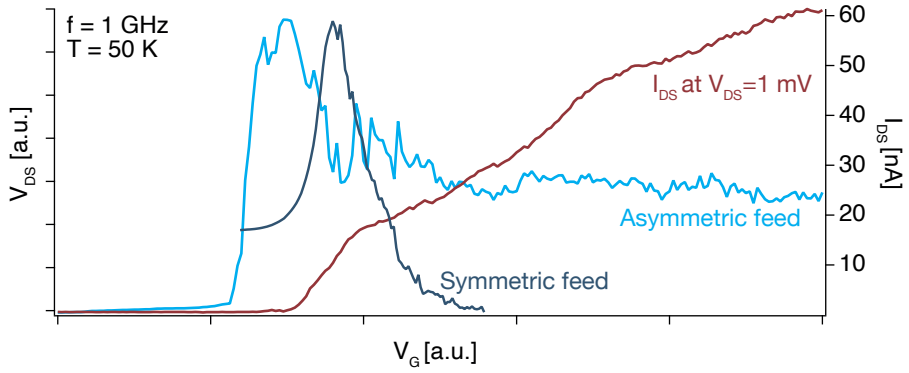

FIG. 4.9: MW response at fixed power, frequency and temperature, in the asymmetric (device 42 Cnw1) and symmetric (device 41 Cnw3) configurations. Gate voltages are scaled in such a way that the two transfer curves matched as much as possible. Here only the current curve relative to device 41 Cnw5 is reported.

considered by accounting for the measured source-device attenuation. This attenuation is a frequency dependent value, obtained using a Vector Analyser (described in chapter 3). By measuring the response as a function of the impinging power the linear dependence of the signal from the radiation power over several orders of magnitude is established. Results of this analysis, showing the voltage responsivity R_V as a function of the backgate, are reported in figures 4.7 and 4.8. The gap in the responsivity curves is due to the non linearity of the MW response in the previously discussed pinch-off region.

Symmetric and asymmetric configurations

Finally we compare symmetric and asymmetric feeding configurations. In figure 4.9 the flat region of MW response is only visible in the asymmetric configuration. In the symmetric configuration the signal intensity has a sharp decline for gate voltages slightly higher than the pinch-off. In the following we will implicitly consider every device to be in the asymmetric feed configuration and with gate voltages high enough to be in the flat response region, unless explicitly stated.

4.2.0.1 *Temperature modulation of the response*

Here the temperature dependence of the responsivity is investigated. Figure 4.10(a) shows transfer curves at 4, 125 and 300 K. The pinch-off moves towards higher gate voltages for decreasing temperatures. The analysis described in the previous chapter is repeated for each temperature, from which the responsivity curves shown in figure 4.10(b) are obtained. By decreasing the temperature, the operation region moves to higher backgate values, following the pinch-off shift. At the same time, a clear increase in the responsivity value is obtained through cooling. Figure 4.11 shows this trend in detail: for all of the devices studied a similar trend is obtained, even if the responsivity values differ slightly. By normalizing the data to a common value, chosen as the interpolated $R_V(T = 50\ \mathrm{K})$, all samples follow the exact same trend. The responsivity increases by a factor of ~ 5 going from 300 K to ~ 20 K. In doing so, because of the pinch-off voltage shift, the operating range of gate voltages slightly moves toward higher gate voltage values.

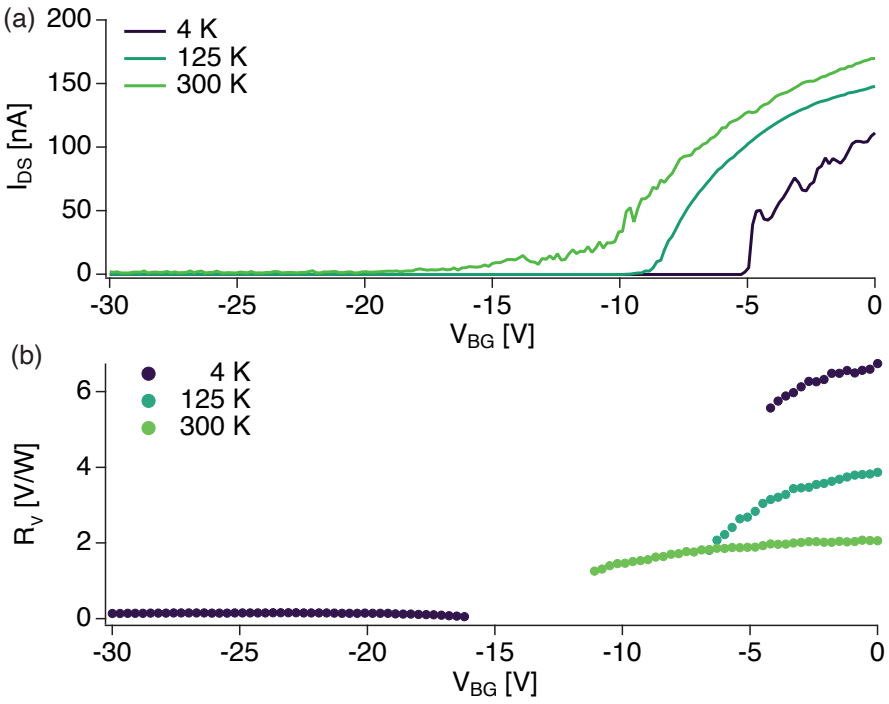

FIG. 4.10: (a) Transconductance plots already shown in 4.5, reported here for comparison with the (b) responsivity as a function of the backgate voltage (acquired with a backward sweep). Results from device 44 Bd1.

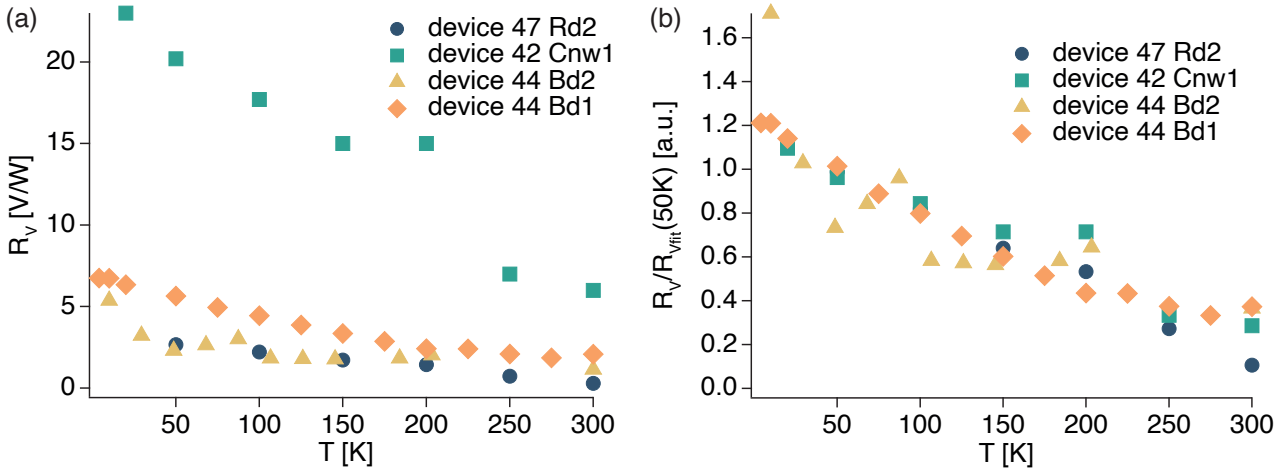

FIG. 4.11: (a) Responsivity as a function of the temperature, in a given configuration, for some of the measured devices. (b) Responsivity scaled to the interpolated value at 50 K for each device. While the absolute values of the responsivities might be very different depending on the device and configuration, the general trend that I observe is the same in each case.

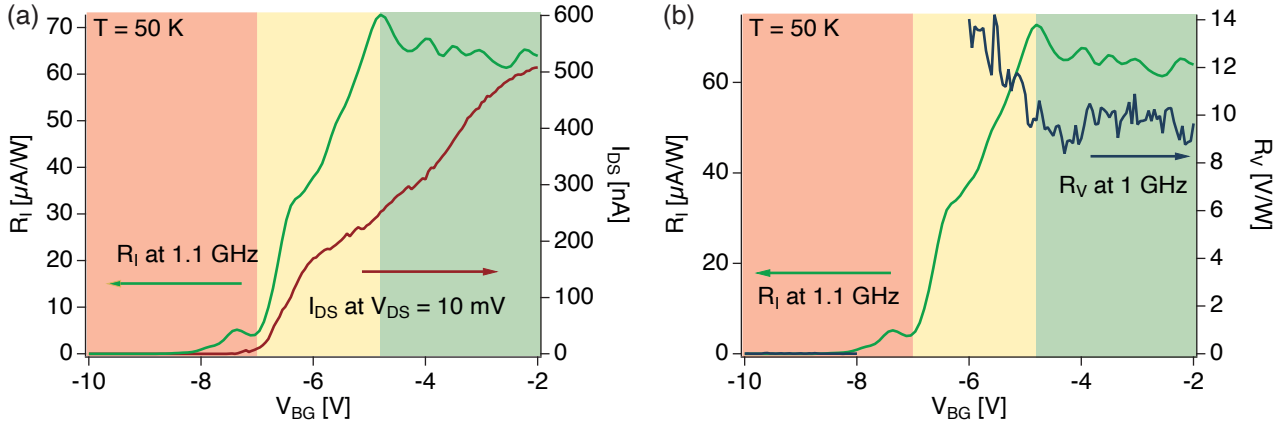

FIG. 4.12: (a) Current responsivity R_I as a function of the backgate and the transconductance curve. (b) comparison of the voltage (R_V) and current (R_I) responsivities as a function of the backgate. Results from device 42 Cnw1.

4.2.1 *Current responsivity*

An alternative approach for the detection of the MW signal is to measure the induced current while applying $V_{DS} = 0$. Also in this case the current is usually proportional to the input MW power. The current responsivity R_I can be introduced. By applying the same procedure described before, the relationship between R_I, the backgate voltage and the transfer curve is investigated. In figure 4.12 the pinch-off region still shows linear response as a function of the input power, differently from what observed for the voltage signal. An almost flat responsivity is obtained far from the pinch-off, in the same region in which R_V is constant. Given a certain gate configuration and temperature, the ratio of the responsivities is constant: $R_V/R_I = 14 \pm 3$ kΩ, that is consistent with the measured nanowire resistance of 12 kΩ at that configuration. The two detection mechanisms are therefore linked and can be alternatively used depending on the target application.

Temperature dependence

Figure 4.13 shows the evolution of the responsivities as a function of the temperature. R_V follows the already discussed trend, increasing with the temperature; R_I - except for the value obtained at 300 K - follows the inverse trend, decreasing with the temperature. The ratio between the two can be compared with the nanowire resistance in the same configuration, as shown in figure 4.13(b). Once again R_V/R_I is consistent with the resistance value, even if it changes by almost two orders of magnitude. This suggest, once again, that the R_I and R_V are directly linked by Ohms law, also explaining the observed trend of R_I as a function of the temperature. While R_V increases with decreasing temperature, the nanowire resistance increases more than enough to compensate for it.

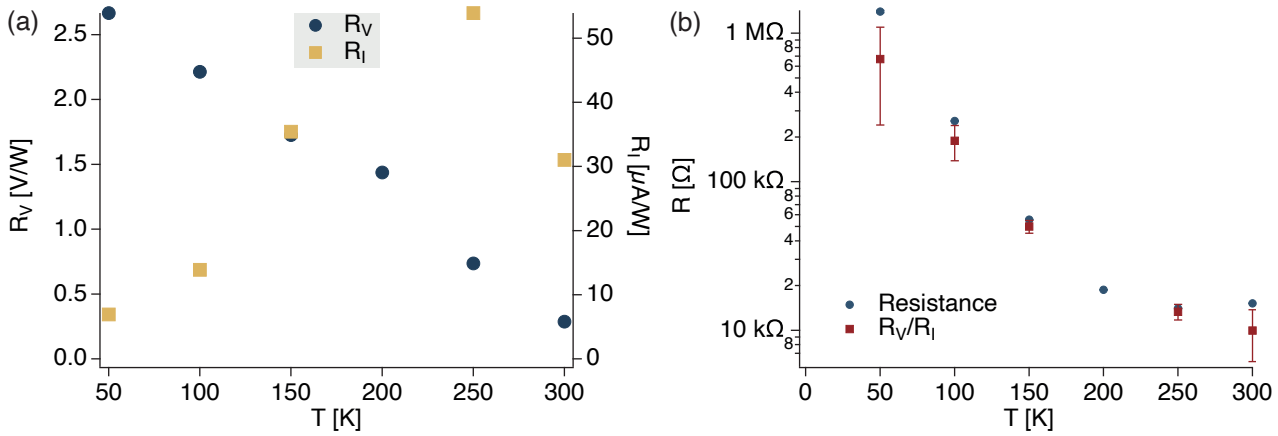

FIG. 4.13: (a) Responsivities R_V and R_I for the same device (47 Rd2) and sidegate configuration ($V_{SG} = 0$ V) as a function of the temperature. (b) Nanowire resistance and ratio R_V/R_I as a function of the temperature.

4.2.2 *Frequency dependency*

The frequency response changes drastically depending on the microwave feed approach used. Feeding to one of the drain or source contacts proved to be the most efficient approach: not only the responsivity was much higher (1 order of magnitude or more), but as a function of the microwave frequency the response was smoother and better accounted for by the experimental setup. In the gate feed case, R_V showed resonance peaks that might be due to local field modes in the proximity of the nanowire. Here we should note that the nanowires are an extremely small probes of the electric field. Some discrepancy between the NW response (which is local) and the transmission spectra of the microstrip, as measured from the external (non local) network analyser, is therefore expected. Figure 4.14 shows the spectra for a device fabricated on a Si substrate, in which the microwaves were fed to the drain contact. The observed MW signal clearly follows pretty well the measured attenuation from the MW source to the device. Once again, the attenuation can be estimated by fitting the V_{DS} vs MW power curve, but considering for each frequency set point the respective attenuation, since it is strongly frequency dependent. The obtained $R_V(f)$ is flat in the region $2 < f < 8$ GHz, demonstrating broadband rectification. At lower frequency ($f < 2$ GHz) the response is stronger, which might be due to an overestimation of the attenuation in this range.

The presence of a different rectification mechanism for $f < 2$ GHz can be ruled out thanks to the microstrip coupling devices. The nanowire signal at fixed power, shown in figure 4.15, qualitatively follows the attenuation spectrum. Once again by accounting for the frequency dependent attenuation it is possible to compute $R_V(f)$. The result obtained with this approach displays resonance peaks that were not visible for the direct coupling sample shown in figure 4.14. We at-

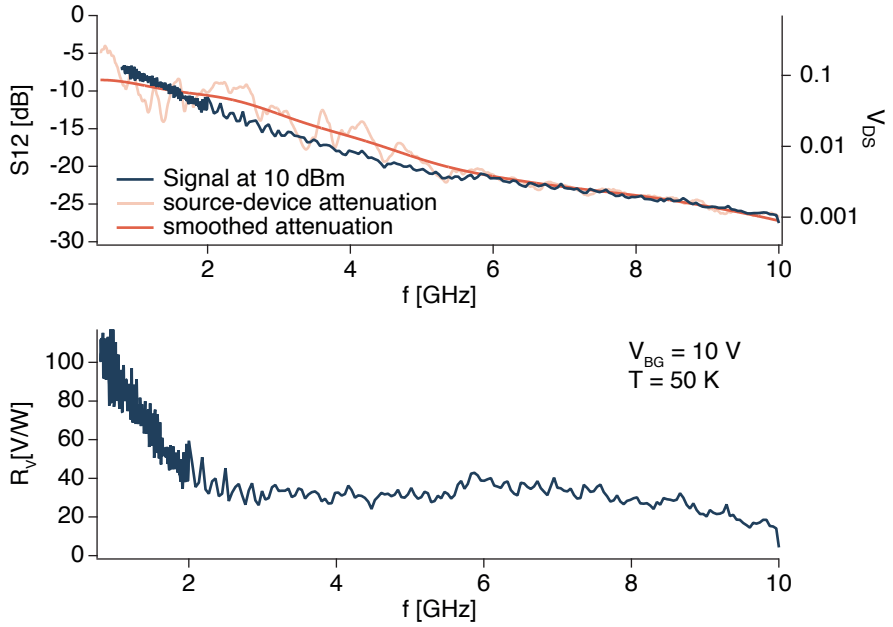

FIG. 4.14: The observed nanowire response to the incident microwaves exhibits a frequency dependence. Here I compare this behaviour with the spectrum of the attenuation between the MW source and the device and observe that they follow the same trend. If I consider this frequency dependent attenuation in the calculation of the responsivity for each point I get the spectra shown in the bottom graph. Results from device 41 Anw2.

tribute these to local resonances in the metallic contacts. At the same time no significant trend of R_V is visible for $f < 2$ GHz. This confirms that the observed trend is dominated by the microwave matching conditions and not by intrinsic characteristics of the nanowire response.

4.2.3 *Noise equivalent power*

In order to measure the signal to noise ration, we measure - with half a second of integration time - the target signal repeatedly at each input power level (P). For each set point, an average and a noise figure are extracted. The Noise Equivalent Power (NEP) is defined as the input power at which the signal to noise ratio (SNR) is equal to 1, in a 1 Hz bandwidth. The knowledge of the signal intensity as a function of the power and of the noise figures allow the determination of the NEP. Figure 4.16 shows the $I_{DS}(P)$ trend for device SC-Si-42 Cnw1. In principle, this kind of plot allows a graphical determination of the NEP: it is the power at which signal and noise curves intersect. While measuring V_{DS} the intersection happens at ~ -24 dBm which corresponds to a NEP $= 1.5\ \mu\text{W}/\sqrt{\text{Hz}}$. While measuring I_{DS} the two lines never intersect in the explored power range. This suggests that in the first case the NEP must be determined by a limitation of the used voltmeter rather than by and intrinsic limit of the rectification

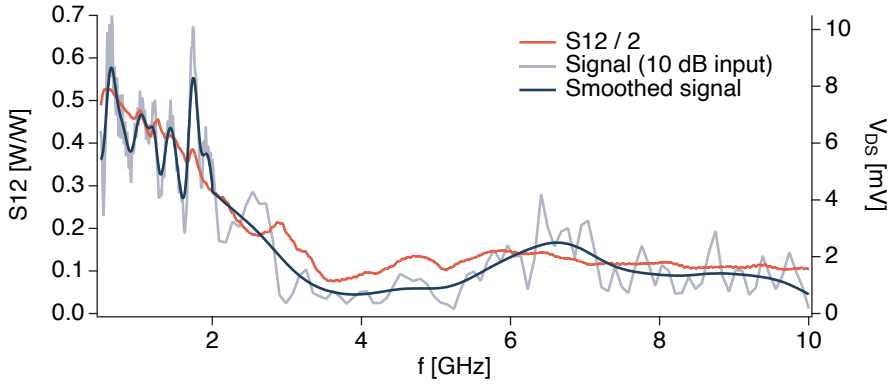

FIG. 4.15: (Top) Nanowire response and microwave source-device attenuation as a function of the frequency for a device fabricated together with an Ag microstrip on a sapphire substrate. Results from device 47 Rd2.

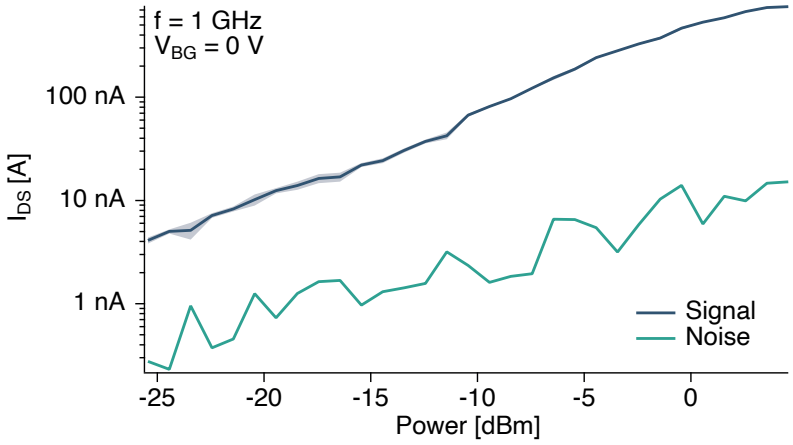

FIG. 4.16: I_{DS} signal and noise level as a function of the incident power on the device at T = 50 K. Responsivity $R_I = 444 \pm 2$ μA/W and NEP = 1 μW/$\sqrt{\text{Hz}}$. Results from device 42 Cnw1.

mechanism. This is confirmed by the lowest level of noise observed, 35 μV, which corresponds to the known sensitivity of the used SMU unit while in voltmeter mode. In devices with higher resistance, the NEPs in the two cases are closer.

Even without the graphical approach, it is still possible to estimate the NEP from the knowledge of the responsivity. By estimating the minimum noise level N (typically done at the lowest power level measured) the NEP can be determined:

$$\text{NEP} = \frac{N}{R_{V(I)}} \tag{4.3}$$

where $R_{V(I)}$ is the voltage (current) responsivity. These considerations are valid if the integration time is chosen as 1/2 second, which

matches the 1 Hz bandwidth definition. If a different integration time t_i is chosen the definition becomes:

$$\mathrm{NEP} = \frac{N \times \sqrt{t_i}}{R_{V(I)}} \tag{4.4}$$

The best voltage responsivity measured is $R_V = 100$ V/W at a temperature of 50 K, with typical values falling in the $20 - 40$ V/W range. Noise equivalent powers in the case of voltage responsivity were found to be limited by the voltmeter to NEP $= 1.5\ \mu\mathrm{W}/\sqrt{\mathrm{Hz}}$. Current responsivities in the range $200 - 500\ \mu$A/W were observed at temperatures of 300 and 50 K, with NEP as little as NEP $= 0.4\ \mu\mathrm{W}/\sqrt{\mathrm{Hz}}$.

4.3 DISCUSSION

Chapter 1.1.1 summarizes several rectification mechanisms that could be employed for microwave detection in InAs nanowires. Here we will discuss all of these mechanisms in light of the results of this chapter. The mechanisms can be divided in thermally and electrically drive. Among the former we mentioned the Bolometric effect and the Photo thermoelectric effect.

Bolometric effect

The bolometric effect is usually active at low carrier concentration ($n \sim 10^{16}$ cm^{-3} from [18]). The bolometric voltage is proportional to β/σ where σ is the static conductivity and $\beta = \mathrm{d}\sigma/\mathrm{dT}$ is the bolometric coefficient.

Photo thermoelectric effect

The Photo thermoelectric effect (PTE), was found in the same work to be active at high carrier densities $n > 10^{17}$ cm^{-3}, which is consistent with the requirement for high conductivity. The photocurrent is in this case given by $I_{PTE} = -\sigma S_b \nabla T$ where S_b is the Seebeck coefficient and ∇T is the thermal gradient. While this mechanism might be at play in higher radiation frequency, it leads in this case to unreasonable results. The work from Roddaro et al. [33] investigates in detail the thermoelectric effect in InAs nanowires. At room temperature, for a temperature difference across a $\sim 4\ \mu$m nanowire of $\Delta T \approx 12.5V$, they measure a thermoelectric voltage of ~ 1.5 mV. In our devices, at room temperature and for nanowires 400 nm long, voltages in the order of 20 mV are observed. This would correspond to temperature differences in the order of 100 K (and gradients 1000 times greater than those reported) which are unreasonable at room temperature at such a small scale.

Active rectification

In chapter 1.1.1, among the electrically mediated rectification mechanisms active rectification and plasma waves were presented. Active rectification is limited by the RC cut-off frequency of the devices. The value of the cut-off frequency can be estimated starting from the DC parameters in the quasi-static approximation: $f_T = \frac{g}{2\pi C}$,[38, 39] where g is the maximum of the transconductance and C is the total gate capacitance of the device. The gate capacitance

of the nanowire can be calculated for a backgate from geometrical parameters: $C = \frac{2\pi\epsilon_0\epsilon_r}{cosh^{-1}(t/R)}L$.[172] From these considerations, a rough estimate of the cut-off frequency is obtained for one of the tested devices devices: $f_T = 160$ MHz. This is one order of magnitude smaller than the investigated frequencies. In addition to this, this rectification mechanism intrinsically requires active control of the device resistance, via gate control. This is typically archived through comparators that sense the incoming radiation and apply a voltage on the gate electrode with the right timing in order to open the channel, allowing current flow in only one direction. One of the studies devices (sample 47 Rd1) displayed rectification even if no gate electrodes were available, which would be impossible if the underlying mechanism was active rectification.

Alternative mechanisms

Here we note that other mechanisms are present in the literature, but they require a significantly different device architecture:

- Photon assisted tunnelling: can be ruled out because it requires discrete energy levels that are not present in InAs nanowires, especially at high temperatures.[174]
- Photo-gating: that is only reported at frequencies several orders of magnitude higher than those studied here (mid-infrared to the UV). [175]
- Ballistic rectification: ballistic electrons are scattered by the edges of the device, which is fabricated with a specific geometry. The electrons are therefore funnelled towards one electrode where they are picked up. [176]

Finally we introduce in this discussion the distinction made between symmetric and asymmetric microwave feed. Figure 4.9 showed that in the symmetric configuration the only significant rectification happened close to the pinch-off. With the backgate capacitance model the electron density at these gate voltages can be estimated to be in the order of $n \sim 10^{16}$ cm^{-3}. This is consisted with the Bolometric effect: the it is present at low carrier concentrations that match those reported in the literature, and is active both in the symmetric and asymmetric configurations since some global heating of the device is always present to a certain extent.

In the asymmetric configuration, an additional signal at higher gate voltages is present. This regime corresponds to an estimated carrier density of $n > 10^{17}$ cm^{-3}, which is once again consistent with what is reported in the literature. Both the photo thermoelectric effect and the damped plasma waves require an asymmetry in the MW feed or device design. Because of the previous discussion on the magnitude of the measured effect we rule out the photo thermoelectric effect, and tentatively explain the rectification as the result of the damped plasma waves. Figure 4.17 shows the two regimes in the rectification

signal, as a function of the gate voltage. In summary: at low carrier concentrations ($n \sim 10^{16}$ cm^{-3}) the signal is due to the bolometric effect. This phenomena is present both in the symmetric and asymmetric configurations because they both induce global heating of the nanowire. At high carrier concentrations ($n > 10^{17}$ cm^{-3}) an additional is present that can be tentatively accounted for by damped plasma waves. The presence of this signal only in the asymmetric configuration corroborates this explanation.

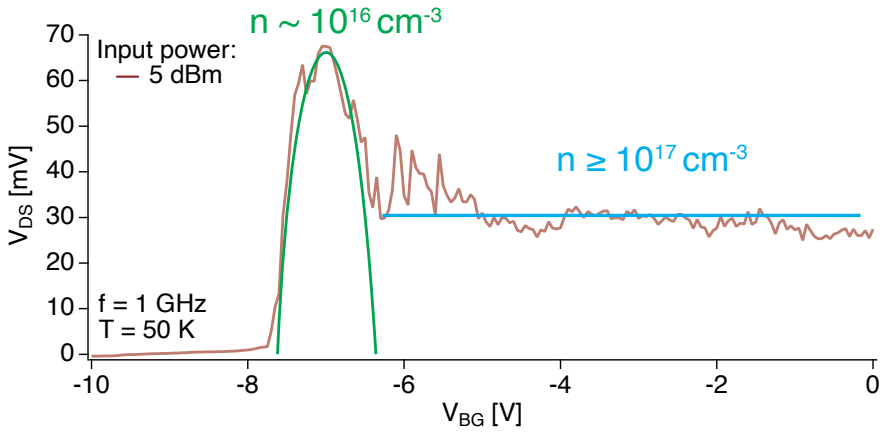

FIG. 4.17: Rectification signal at fixed microwave power, frequency and temperature. Two regimes are distinguished. A peak signal at $V_{BG} = -7$ V, in a region with carrier concentration $n \sim 10^{16}$ cm^{-3}, and a flat signal for $V_{BG} > -7$ V, in a region with carrier concentration of $n > 10^{17}$ cm^{-3}. Results from device 42 Cnw1.

In conclusion we have investigated microwave induced transport in InAs nanowires. We have shown robust and reproducible rectification above a gate voltage threshold and investigated the dependence of detection efficiency from different parameters such as temperature, radiation frequency and gate voltage. Furthermore we demonstrated that the the same device can be operated in voltage detection or current detection modes. We studied different device architectures, which helped us establish the broadband frequency response of our device, and different microwave feeding modes, which lead to distinct trends in the MW response. We tentatively associate these to specific detection mechanisms among those discussed in the literature for similar phenomena. We find that through control over the electron density in the field effect transistor we can operate in regimes where these distinct detection mechanisms are active.

5 EXPERIMENTAL RESULTS ON QUANTUM DOTS

In this chapter we study InAs/InP nanowire based quantum dots coupled to coplanar superconducting resonators. First, we characterise the stability diagram of InAs/InP NW QDs; then we study Coulomb-blockade lifting in the presence of an off-resonant MW drive. We find that MW effects exhibit a power threshold and, under suitable conditions, current polarity reversal can be observed. Our results show that MW assisted tunnelling can take place in non-resonant conditions as an effect of the voltage fluctuations of the microwave field and may depend on the presence of excited states of the QD involved in the tunnelling process. Finally we demonstrate that this effect can be exploited for the realization of a sensitive MW detector at the resonator frequency.

Results discussed in this chapter were published in Scientific Reports.[3]

5.1 INAS/INP DEVICES DESCRIPTION AND CHARACTERIZATION

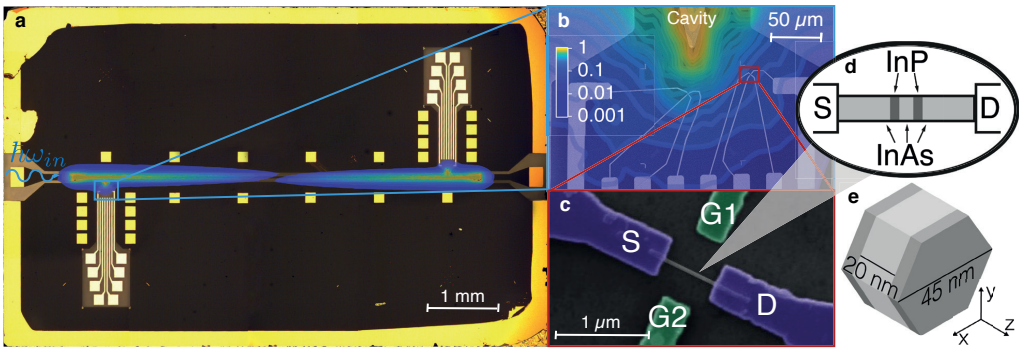

FIG. 5.1: (a) Optical microscope image of the whole electrical device with central YBCO/sapphire coplanar resonator. Gold contacts and bonding pads are used for connecting dc lines and the coplanar resonator to the external cables. (b) Scanning Electron Microscope (SEM) close-up showing the antenna tip and the leads of two NW QD devices. In panels (a) and (b) the finite-element simulation of the distribution of the electric component of the fundamental mode of the resonator is superimposed with false colours. The colour scale is normalized to the maximum value. (c) False colour SEM image of the NW QD device investigated in this work, where source (S), drain (D) and gate (G1, G2) leads are indicated. (d) Schematic diagram of the InAs/InP NW QD. (e) Sketch of the NW QD showing InAs (light grey) and InP (dark grey) sections. From reference [3].

In order to optimise the coupling with microwaves, NW QD devices were fabricated in proximity of a half-wavelength superconducting coplanar resonator. The resonator was realised out of a 8×5 mm^2 YBCO/sapphire film and presents a 6 mm-long central conductor, having width of 30 μm and distance of 55 μm from the lateral ground planes. The fundamental mode has resonance frequency

$\omega_0/2\pi = 9.815$ GHz (section 5.4.2). QD devices are fabricated in correspondence of the electric antinodes of the fundamental mode of the resonator, where two tips connected to the central strip are designed to work as "antenna", in order thus to extend and enhance the microwave field in proximity of the NW QD device (Fig. 5.1(a,b)). Up to four QD devices can be individually tested for each chip. In this work we report results obtained on one of our NW QD devices, positioned at 65 μm from the antenna tip (Fig. 5.1).

In order to characterise the QD we first measured the dc current (I_{SD}) as a function of bias voltage (V_{SD}) and gate voltage (V_G). The same voltage was applied simultaneously to both side gates ($V_{G1} = V_{G2} = V_G$). The stability diagram of the NW QD measured at the temperature $T = 2$ K presents a typical Coulomb-diamond structure (Fig. 5.2(a)). The addition energy of the N-th electron in the QD can be estimated in the framework of the constant interaction model [50]:

$$\mu_N = E_k + \frac{Ne^2}{C} - |e|\alpha V_G + c, \tag{5.1}$$

where E_k is the energy of the first available QD level, C is the capacitance of the QD and c is a constant. The lever arm α is a geometry-dependent parameter that accounts for the effect of gate voltage on QD levels, which can be obtained from the diamond boundary slopes m_1 and m_2 as $1/\alpha = 1/m_1 - 1/m_2$. Data in Fig. 5.2(a) yield average values $\alpha = 120 \pm 20$ mV/V and a charging energy $e^2/C = 9 \pm 2$ meV. The split of the energy levels in our QD well matches values obtained for hard-wall InAs/InP NW QDs (*ca.* 10 meV) having similar geometry and stronger axial confinement along the growth direction of the NW [29, 53].

The plot of I_{SD} at constant voltage bias $V_{SD} = 1$ mV is shown in the top panel of Fig. 5.2(a). As a function of the gate voltage, full depletion and progressive occupation of the QD states can be observed. Although collected data do not allow for a direct correspondence of current peaks with electron levels with spectroscopic precision, we expect that electrons are added to fill in the shell structure of the QD, which is determined by the specific characteristics of the electron orbitals [46–48].

Data plotted in log-scale in Fig. 5.2(a) show a marked increase of the peak current from ~ 10 pA to ~ 1 nA beyond a threshold voltage of 1 V. These abrupt change reflects the different tunnelling rates (Γ) that can be estimated by considering the Fermi-Dirac occupation of the source and drain leads at $T = 2$ K (section 5.4.1). By fitting the $I_{SD}(V_{SD})$ peaks, we obtain $\Gamma' = 1$ GHz for $V'_G = 0.86$ V, whilst for $V_G > 1$ V we estimate $\Gamma'' \approx 10$ GHz. These numbers are consistent with what previously observed in similar QD devices [53].

The stability diagram taken as function of the gate voltage for $V_G \sim V'_G$ is shown in Fig. 5.2(b). The diamond exhibits two different

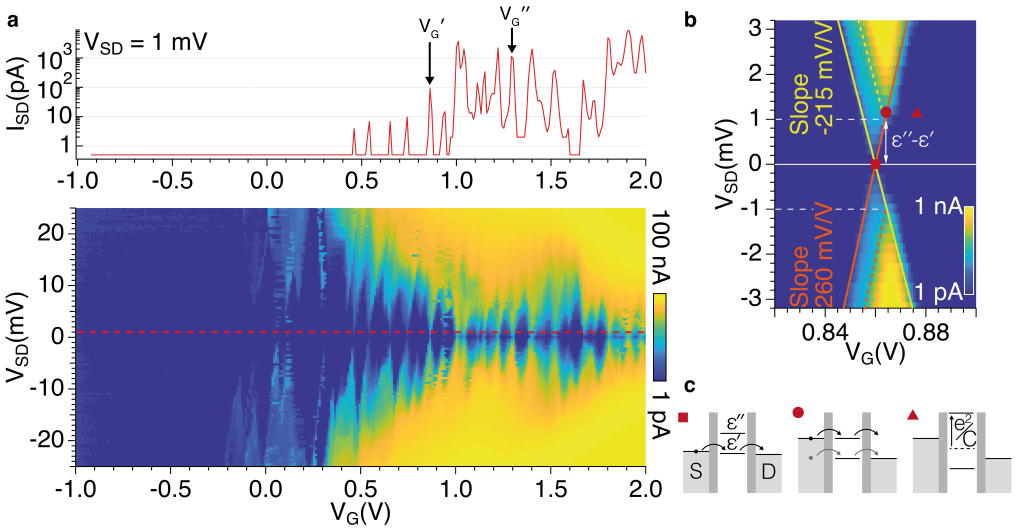

FIG. 5.2: (a) Stability diagram (bottom panel) and cross-cut at $V_{SD} = 1$ mV (top panel) of the $\log(|I_{SD}|)$ current measured at $T = 2$ K. (b) Blow-up of the current map measured in the proximity of the peak at $V'_G = 0.86$ V. The colour scale is logarithmic. (c) Schematic diagrams showing the configuration of the electrochemical potentials of ground (ϵ') and first excited (ϵ'') states in correspondence of the symbols in panel (b). From reference [3].

slopes ($m_1 = -215$ mV/V and $m_2 = 260$ mV/V) that correspond to slightly asymmetric lever arms for source and drain leads. Fig. 5.2(b) shows that $I_{SD} \propto \Gamma' V_{SD}$ for voltage gate $V_G = V'_G$ and bias $|V_{SD}| < 1$ mV, whilst a steeper dependence $I_{SD} \propto \Gamma'' V_{SD}$ is observed for $|V_{SD}| > 1$ mV. This behaviour suggests that the Coulomb peak is related to tunnelling through two charge states with the presence of an excited level at energy $\Delta E_k = \epsilon'' - \epsilon' \approx 1$ meV.

The electron tunnelling through the QD can be depicted as in Fig. 5.2(c), which shows the configuration of the electrochemical potentials $\mu(\epsilon')$ and $\mu(\epsilon'')$ as a function of the gate voltage around V'_G. For $V_G = V'_G$ and $V_{SD} = 1$ mV (square symbol in Fig. 5.2(b,c)), the tunnelling involves only the energy level ϵ', thus the low tunnelling rate Γ' gives rise to a low tunnelling current. By expanding the bias window ($|V_{SD}| > 1$ mV) (circle symbol), the transmission channel through ϵ'' becomes accessible and contributes to the electron transport. A sudden increase of the tunnelling current is observed as a consequence of the larger tunnelling rate Γ''. When $|V_G - V'_G|$ is sufficiently large (triangle symbol), the level ϵ' is permanently filled and the addition of an extra electron costs the charging energy e^2/C. In this case, ϵ'' is no longer accessible and the current flow is blocked.

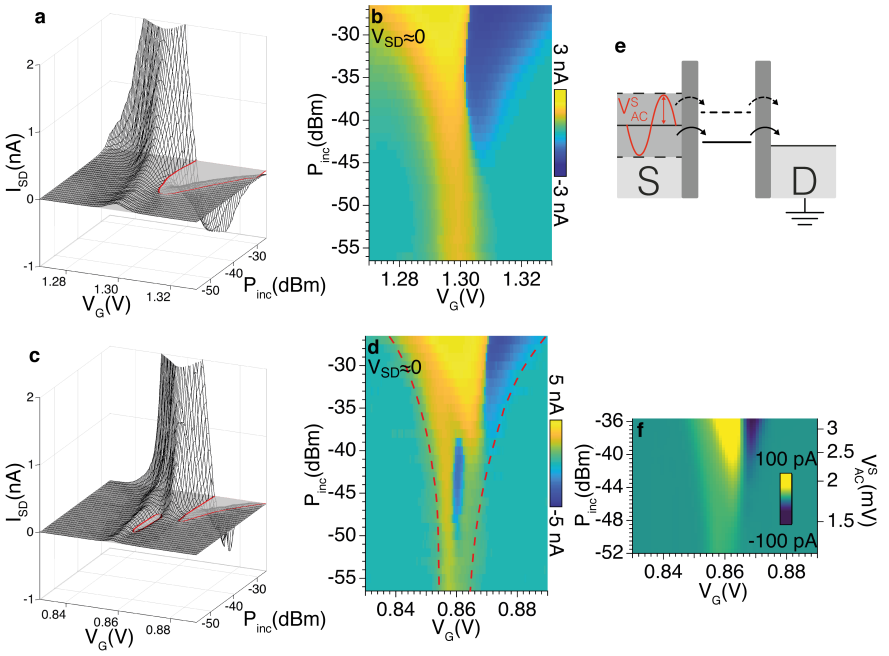

FIG. 5.3: Evolution of the $I_{SD}(V_G)$ characteristics in the presence of a microwave drive of frequency ω_0 and increasing power P_{inc}. Three dimensional plots and maps are measured for gate voltage around $V_G'' = 1.30$ V (a,b) and $V_G' = 0.86$ V (c,d) at the temperature $T = 2$ K. Solid lines indicate the contour of regions with negative I_{SD}. The dashed line in panel (d) display the zero current points used to extract the peak width ΔV_G. (e) Schematic energy diagrams showing the MW-assisted tunnelling through the dot levels ϵ' and ϵ''. (f) $I_{SD}(V_G)$ characteristics calculated for $V_{SD} \simeq 0$ by averaging the measured current over increasing voltages V_{AC}^S. From reference [3].

5.2 MICROWAVE-ASSISTED TRANSPORT

In order to study the effect of the microwaves on the transport properties of InAs/InP NW QDs, current measurements were performed in the presence of a monochromatic wave ($\omega_0/2\pi = 9.815$ GHz). In the following we shall focus on two Coulomb peaks at $V_G' = 0.86$ V and $V_G'' = 1.30$ V that are representative of the two electron transport regimes as previously described. We initially focused on the Coulomb peak at $V_G'' = 1.30$ V to investigate the $I_{SD}(V_G)$ characteristics by varying the microwave power (Fig. 5.3(a,b)). As a general observation, the presence of an intense MW drive leads to amplification of the tunnel current and, as expected, this is particularly evident close to $V_{SD} = 0$. No effect on electron transport is detected for $P_{inc} < -55$ dBm, while MW impact increased more than linearly with increasing MW power. For $P_{inc} > -45$ dBm a polarity reversal of I_{SD} and the broadening of the Coulomb peak are visible. In particular, a negative current peak appears for $V_G > 1.30$ V even with $V_{SD} > 0$. Such trends are found for all Coulomb-blockade peaks that were investigated.

In the case of the Coulomb peak at $V_G' = 0.86$ V (Fig. 5.3(c,d)), an additional dip with $I_{SD} < 0$ (*i.e.* current polarity reversal) is present in the intermediate power range ($-50 < P_{inc} < -38$ dBm) and steps appear in the I_{SD} characteristics for $P_{inc} > -38$ dBm. In order to further investigate this point, we mapped I_{SD} as a function of V_{SD} and V_G under constant MW power. Figure 5.4(a-c) shows the evaluation of the Coulomb diamond with increasing P_{inc}. For $P_{inc} = -36.5$ dBm

two current peaks are visible in panel (c). This effect is enhanced for high power (panel (d)), where the two peaks broaden and merge. The additional dip in Fig. 5.3(c,d) for -50 dBm $< P_{inc} <$ -38 dBm can thus be related to the evolution of the diamond shape as a function of the MW power, which gives rise to multiple reversal of the current in the $I_{SD}(V_G)$ characteristics for $V_{SD} \approx 0$.

In hard-wall InAs/InP NW QDs Coulomb blockade persists up to $T \approx 50$ K [53], thus the effect of the MW field on the transport characteristics can be tested at intermediate cryogenic temperature. At 8 K the Coulomb peaks are much broader, yet the reversal of I_{SD} is still visible for large power levels (section 5.4.3). The comparison between 2 and 8 K data shows that the effect of the temperature on the $I_{SD}(V_G)$ characteristics is qualitatively different from that of the microwave drive, ruling out the possibility that the observed behaviour is simply due to heating.

5.3 DISCUSSION

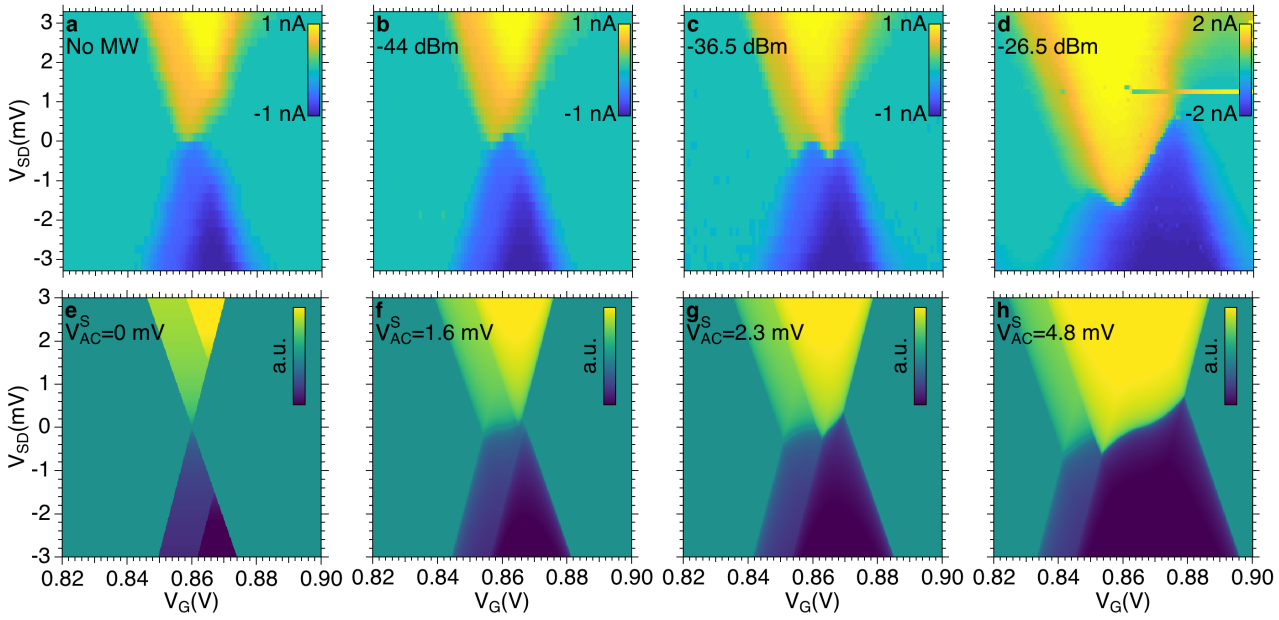

FIG. 5.4: (a,b,c,d) Charge stability diagrams measured around the Coulomb peak at gate voltage V'_G=0.86 V. (e,f,g,h) Calculated evolution of the stability diagrams in presence of different voltages V^S_{AC} as reported in the text. From reference [3].

In NW QDs used in our experiments, the separation between the energy levels of the QD is orders of magnitude larger than the energy of the fundamental mode of the resonator ($\hbar\omega_0 \approx 40$ μeV). This implies that the observed effects (broadening of the Coulomb peak and reversal of the tunnelling current) are not related to resonant transitions between single-particle energy levels. On the other hand, the effects of MW are evident for finite intensity of applied electromagnetic radi-

ation: in the many-photon regime and for $k_B T > \hbar\omega_0$, the microwave mode can be treated as a classical electromagnetic field that induces a broadening of the electrodes energy levels [70, 71, 73, 74]. More specifically, the coupling with the microwave field induces an oscillating voltage of amplitude V_{AC}^S on the source lead. At $V_{SD} = 0$, and for a given V_G, the current flows when V_{AC}^S matches the equivalent value of $|V_{SD}|$ that would lift the Coulomb blockade. Therefore the width of the peak results $\Delta V_G = 2V_{AC}^S / \min(|m_1|, |m_2|)$, where m_1 and m_2 are the slopes of the diamond edges. For a given power P_{inc}, V_{AC}^S can be estimated from the broadening of the Coulomb peak in Fig. 5.3(d). We calculated the $I_{SD}(V_G)$ characteristics by following the method suggested in Refs. [73, 74] which consists in calculating, for each V_G value, the average of the current over the $\pm V_{AC}^S$ interval. Curves obtained from the experimental data in Fig. 5.2(b) are displayed in Fig. 5.3(f). It is worth noting that the main trends of the experimental $I_{SD}(V_G)$ data shown in Fig. 5.3(a-d), in particular current amplification, peak broadening and reversal of current polarity for increasing voltage V_{AC}^S, are reproduced by this simple average calculation. Within the framework of this classical model, the reversal of current polarity emerges as a result of the asymmetry of the Coulomb diamonds (*i.e.* $m_1 \neq m_2$).

More careful inspection of experimental spectra reveals however a more complex behaviour such as a multiple reversal of current polarity, as shown in Fig. 5.3(c,d) and in the maps in Fig. 5.4(a-d) and this demands more details. Here it is worth pointing out that multiple reversal of current polarity was observed in coincidence of the Coulomb peak at V_G' (Fig. 5.2(b)), for which the presence of an additional excited states is evident in the measured stability diagram. Kouwenhoven et al. [71] investigated the process of photon-assisted tunnelling with spectroscopic resolution and suggested a model in which excited QD states also contribute to the tunnelling. The phenomenological description of stability diagram we previously discussed allows us to extract the essential parameters to describe the effects of classical microwave field also in the presence of excited states in the QD. We firstly reproduce the main features of the DC stability diagram by means of the experimental parameters m_1, m_2, $\epsilon'' - \epsilon'$, Γ' and Γ'' and we assume $I_{SD} \propto \Gamma V_{SD}$ (Fig. 5.4(e)). Then, to reproduce the evolution of the stability diagram for increasing power P_{inc}, we apply the average method reported above at finite bias V_{SD}. In this way, we can calculate the average of the current for increasing V_{AC}^S voltages. The outcome of the simulations (Fig. 5.4(f-h)) well reproduces the main trends of the experimental data (Fig. 5.4(b-d)).

To check the consistency of this phenomenological model, we compare the V_{AC}^S voltages extracted from the measurements in Fig. 5.3 with the voltage fluctuation generated by the microwave field (V_{AC}). At finite P_{inc}, we calculate the root mean square voltage fluctuation

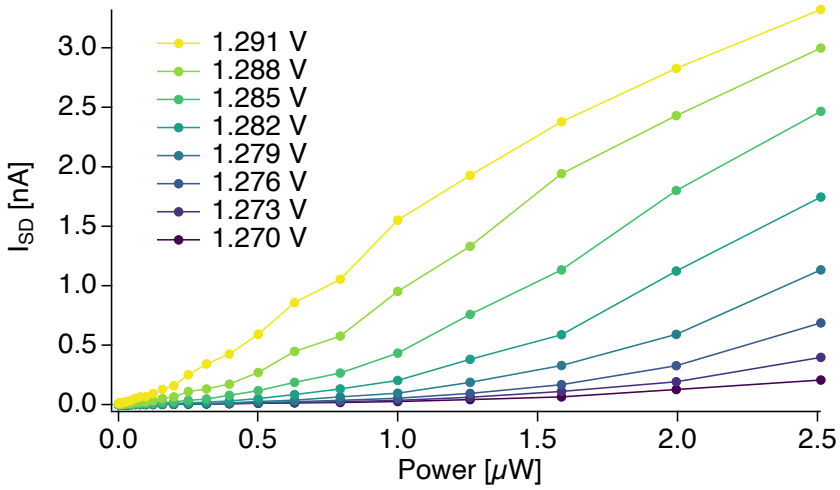

FIG. 5.5: Plot of the measured current as a function of the input microwave power for selected V_G values, taken from the map in figure 5.3(a,b).

as $V_{AC} = \sqrt{2}V_{AC}^{zpf}\sqrt{n+1/2}$, where $V_{AC}^{zpf} = 2.3\ \mu$V is the zero point fluctuation in the center the coplanar resonator and n is the number of photons (section 5.4.2). We introduce the effective coupling factor $\lambda = 5 \times 10^{-2}$ such as $V_{AC}^{S} = \sqrt{2}\lambda V_{AC}$. Finite element simulations indicate that the value of λ is consistent with the estimated decrease of the root mean square electric field between the electric antinode and the position of the QD (Fig. 5.1(b) and section 5.4.2). We also expect that the misalignment between the direction of the electric field and the NW axis contributes in determining its value.

Finally we discuss the use of this device as a microwave detector, in a similar fashion to what is discussed in chapter 4. The current I_{DS} dependence from the input power, plotted for selected gate voltages in figure 5.5, is linear. This response can therefore be used in order to measure the impinging power on the resonator. But the same is not true for the data shown in 5.3(c,d): for a threshold power the excited state with higher tunnelling rate is involved, leading to non linearity in the response. By fitting the data in figure 5.5 a maximum responsivity of $R_I = 1.40 \pm 0.02$ mA/W is determined. Given this result and the noise level it is also possible to estimate the Noise Equivalent Power $NEP = 2.7 \times 10^{-10}\ W/\sqrt{Hz}$.

In conclusion, we have investigated the influence of MW radiation on the transport characteristics of InAs/InP nanowire QDs and found that, above a threshold power, the MW field induces a broadening of the current peak and a current polarity reversal. These effects are relevant for microwave-assisted tunnelling processes in the many-photon regime and reflect the discrete nature of QDs excited states. From these experiments we learn that a suitable choice of the working point, as well as of the electron wavefunction, enables one to control the tunnelling current in strongly confined NW QD systems under external MW excitation. These effects can be exploited for the realization of MW detectors coupling superconducting resonators and QDs.

5.4 ADDITIONAL INFORMATION

5.4.1 *Tunnelling rate*

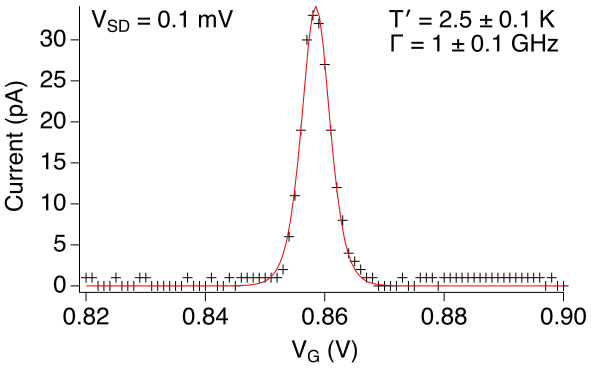

FIG. 5.6: Current I_{SD} measured as a function of the gate voltage V_G at V_{SD} = 0.1 meV (symbols). The fit with Eq.5.2 is displayed by the solid line. From reference [3].

The tunnelling rate of the QD at $V_G' = 0.86V$ was determined by fitting the Coulomb peak measured in the low bias limit with the equation [177]

$$G = \frac{I_{DS}}{V_{DS}} = \frac{e^2\Gamma'}{k_B T'} \frac{1}{4\cosh^2\left(\frac{e\alpha(V_G' - V_G)}{2k_B T'}\right)} \tag{5.2}$$

where α is the lever arm of the gates whilst e, h and k_B are respectively the elementary charge, the Planck and the Boltzmann constants. From the experimental data (Fig. 5.6) we extracted $\Gamma' = 1.0 \pm 0.1$ GHz and $T' = 2.5 \pm 0.1$ K. The latter is compatible with the measured temperature of the experiment (T = 2 K). For Coulomb peaks at $V_G >$ 1 V the tunnelling rate was simply estimated by the maximum value of the current at fixed bias.

5.4.2 *Electromagnetic characterisation*

Electrical characterisation and measurements under microwave radiation were performed down to 2 K in a Quantum Design PPMS by means of a low temperature probe wired with 16 dc filtered lines and 2 coaxial cables. The hybrid device was enclosed in a copper box, in which microwave and dc lines were wire bonded to a gold-plated printed-circuit board (PCB) (Fig. 5.7). A stage of attenuators was inserted at low temperature to suppress the heat radiated from room temperature components. The half-wavelength coplanar resonator was capacitively coupled through 140 μm wide gaps to the coplanar launchers located on the short sides of the chip that, in turns, connect the resonator to the external feed lines. The transmission spectrum

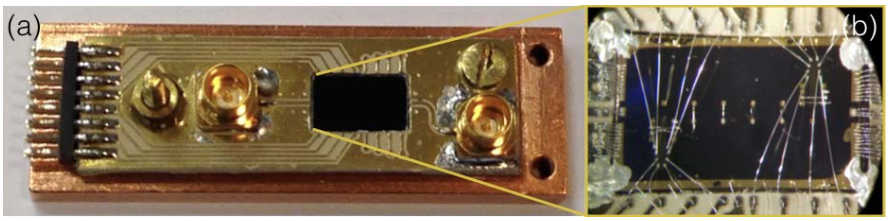

FIG. 5.7: (a) Gold-plated PCB realised on a high dielectric constant AD1000 laminate. Microwave lines are connected through SMP connectors to the coaxial cables. dc lines are linked to the 16 pin connector positioned on the left side of the PCB. The board is installed into an oxygen free high conductivity copper box. (b) Device bonded on the PCB board. From reference [3].

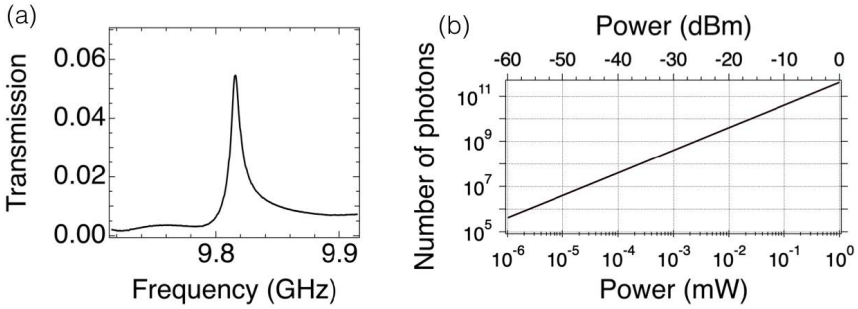

FIG. 5.8: (a) Transmission spectrum of the coplanar resonator showing the fundamental mode (T = 4 K). The incident microwave power is P_{inc} = -13 dBm. (b) Average photon population as a function of P_{inc}. From reference [3].

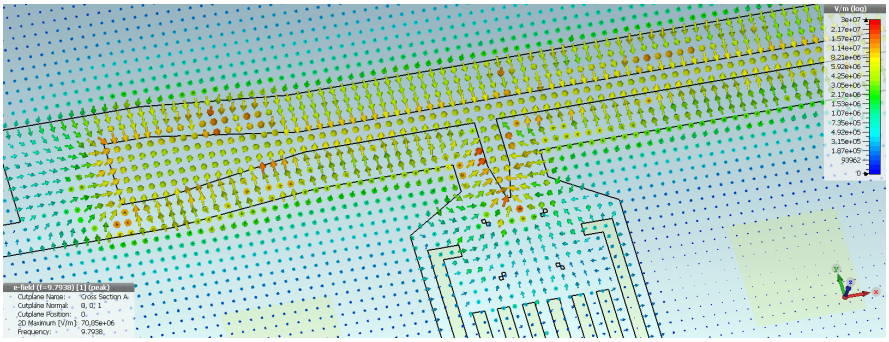

FIG. 5.9: Finite element simulation of the distribution of the electric field component of the fundamental mode of the resonator. The color scale shows the magnitude of the electric field for an incident microwave power P_{inc} = 1 W. From reference [3].

in Fig. 5.8(a) shows the fundamental mode of the YBCO/sapphire coplanar resonator with resonance frequency $\nu_0 = \omega_0/2\pi = 9.815$ GHz. Typical quality factor of our bare YBCO resonators are of the order of 10^4, while the loaded quality factor, as measured for the resonator in the configuration of the hybrid device including metal contacts, is $Q_L \approx 1500$. The insertion loss is IL = 25 dB. To estimate the average photon population in the fundamental mode (n) we use the conventional formula [178]:

$$n = \frac{1}{\pi h \nu_0^2} P_{inc} Q_L 10^{-IL/20} \tag{5.3}$$

where h is the Planck constant and P_{inc} is the incident power. For the typical P_{inc} values used in our experiment we estimate a photon number in the $10^6 - 10^9$ range (Fig. 5.8(b)). Finite element simulations of the coplanar resonator were carried by means of a commercial software (CST Microwave Studio). Fig. 5.9 shows the simulated distribution of the electric field component of the fundamental mode of the resonator. From the simulation, the root mean square (rms) amplitude of the electric field at the antinode can be estimated as $E_{AC}[V/M] = 3.0 \times 10^7 \sqrt{P_{inc}[W]}$. To calculate the zero-point fluctuation, we consider an incident power corresponding to the vacuum state (-150 dBm). The rms amplitude of the vacuum fluctuation of the electric component results $E_{AC}^{zpf} \approx 3 \times 10^{-2} V/m$. For comparison, the root mean square value of the vacuum fluctuation on the center conductor of the resonator can be estimated as $V_{AC}^{zpf} = \sqrt{\hbar\omega_0/2C_{res}}$ (Ref.[141]). C_{res} is the capacitance of the resonator, which can be calculated by analytical techniques and in our case results 0.6 pF.[179] We thus obtain $V_{AC}^{zpf} = 2.3\mu$V. By considering that the distance between the center of the coplanar resonator and the ground planes is $w/2 + s$, being $w = 30\mu$m the width of the central strip and $s = 55\mu$m the longitudinal separation between central strip and ground planes, we get $E_{AC}^{zpf} = 310^{-2} V/m$. This value is excellent agreement with the outcome of the finite element simulations. From the simulated distribution of E_{AC} (Fig. 5.9), we can estimate the rms amplitude at the position of the NW QD device as $E'_{AC}[V/m] \approx 2 \times 10^5 \sqrt{P_{inc}[W]}$. This rms value is two orders of magnitude lower than that estimated at the electric antinode. For the range of incident power -60 dBm$< P_{inc} <$ -20 dBm used in our experiments, the rms amplitude of the electric field results 10 V/m$< E' <$ 100 V/m. We note that the effective length calculated from the ratio $V_{AC}^{lead}/E'_{AC} \sim 30\ \mu m$ suggests that the electromagnetic wave effectively couples to the leads to modulate their voltage.

5.4.3 *Additional measurements*

Fig.5.10 shows the evolution of the Coulomb peak at V_G' for increasing values of P_{inc} (Fig.5.8).In this case the frequency of the microwave tone is $\omega_1/2\pi = 9.810$ GHz. $I_{SD}(V_{SD})$ characteristics measured for increasing power P_{inc} show features comparable to those reported in the main article for $\omega_0/2\pi = = 9.815$ GHz. The vertical shift of the measured curves in terms of incident microwave power follows as a consequence of the reduced transmission at ω_1. No significant frequency dependence was observed within the resonator bandwidth. Fig.5.11(a) shows the stability diagram measured near $V_G' = 0.86$ V at the temperature T= 8 K. With respect to the experimental data taken at T = 2 K (main article), the Coulomb peaks are broader due to the higher temperature. Current polarity reversal and peak broadening are visible in the presence of the microwave drive (Fig. 5.11(b)).

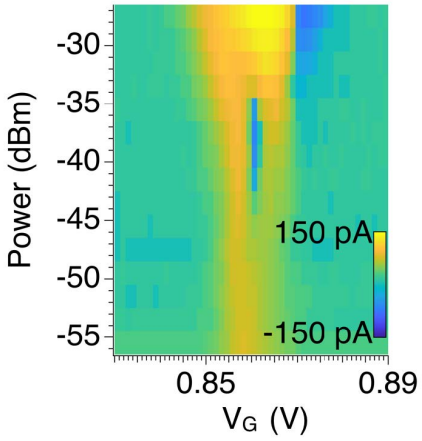

FIG. 5.10: Evolution of the $I_{SD}(V_G)$ characteristics in the presence of a microwave tone of increasing power P_{inc} and frequency $\omega_1/2\pi = 9.810$ GHz. The temperature is T = 2.4 K. From reference [3].

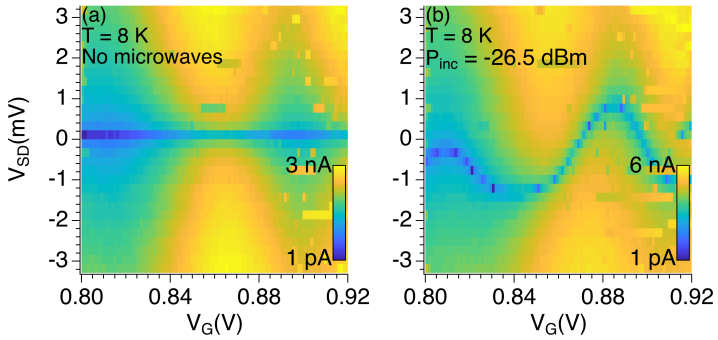

FIG. 5.11: Current (I_{DS}) maps taken at the temperature T = 8 K. (a) P_{inc} = 0, (b) P_{inc} = -26.5 dBm and $\omega = \omega_0$. From reference [3].

6

EXPERIMENTAL RESULTS ON DOUBLE QUANTUM DOTS

In recent years novel architectures based on semiconductor nanowires (NWs) have been proposed for the detection of high frequency radiation [180, 181]. These include arrays of NW diodes [182] and NW field effect transistors[183] for probing THz radiation [18, 19], as well as NW quantum dot (QD) systems coupled to superconducting resonators [3, 81, 105, 130, 157].

The latter systems - NW QDs[184] - can be realized electrostatically using gate electrodes[54, 134, 185, 186] to control tunnel barriers and chemical potentials in the dots, resulting in zero dimensional systems with relatively large size and weak confinement owing to the small energy distance among quantum confined energy levels: these systems can be relatively easily exploited for MW emission [181, 187] and detection down to single photons [68, 108, 109]. On the other hand, single and multiple NW QDs can be engineered exploiting the InAs/InP NW heterostructure technology, that allow to embed few nm-thick InP barriers separated by few tens of nanometres inside an InAs NW body[188]. The InAs island between two InP barriers implements a QD displaying extremely large charging energies, quantum confined energy differences exceeding 10 meV at 4.2 K [51, 52, 189] and a clean Pauli spin blockade up to 10 K [56]: this makes InAs/InP NW QD systems impressively resilient to temperature and magnetic field[35]. While these properties - namely, large energy scales and robust current blockade features - suggest that the InAs/InP NW heterostructure technology may offer intriguing perspectives for the detection of MW radiation, however, their exploitation still represents an open challenge, that must be tackled to boost the application of MW radiation in quantum science and technology.

In this work we exploit hard wall InAs/InP NW heterostructures to address the impact of a MW field on the transport properties of electrons tunnelling across a semiconductor double quantum dot (DQD). MW radiation in the range 1-10 GHz was applied to NW-DQD devices equipped with source and drain electrodes and two independently biased side gates, inducing quantitative and qualitative changes in the charge stability diagram of the nanodevices. Focusing on the triple points, at vanishing source-drain bias, V_{DS}, we map the evolution of the charge stability diagram as function of the MW input power and we address the responsivity of our devices, carefully ruling out the effect of temperature broadening. At finite V_{DS}, the characteristic current triangles emerging in the stability diagram widen in both the filling and detuning directions upon the application

of MWs, while current islands with sign opposite to V_{DS} emerge exactly in correspondence of the zero-bias triple points. To rationalize our experimental outcomes both at zero and finite V_{DS}, we resort to an effective AC bias accounting for the MW field in interaction with the NW-based device. This bias has the effect of shaking the chemical potentials in the leads, which in turns affect the addition energies in the dots via lead-dot capacitive coupling: this induces a shift in the relative alignment of the potentials in the leads and the dots, which explains the main features observed in the charge stability diagrams. These features allow us to measure the local amplitude of the AC drive at the device, without resorting to power calibrations. Our results demonstrate that the unique combination of transport features and spacial resolution offered by InAs/InP NW DQDs make these nanomaterials potential game-changers for future MW detection platforms and applications.

6.1 DEVICE ARCHITECTURE AND OPERATION

Figure 6.1(a) reports the false color scanning electron micrograph of one of the measured NW-DQD devices, equipped with source (S) and drain (D) electrodes (blue coloured) and two side gates (G1-2, green coloured). For this experiment we fabricated more than 20 nominally identical nanodevices starting from the same NW batch, we measured 7 devices and we carried out 8 measurement campaigns in the temperature range 4.2-0.25 K Nanodevice are fabricated onto a Si++/SiO_2 substrate that can be used as a backgate. This, together with the two side gates, allow to fully configure and control the dc transport features - the stability diagram - of the DQD. The inset shows the transmission electron micrograph of the InAs NW region embedding the three InP barriers which defines the DQD. Figure 6.1(b) reports the schematic of the experimental setup - the measurement circuit - together with the nanodevice equivalent circuit (inset). S-D dc bias voltage application and S-D current readout were performed with a source-measure unit, the gates were voltage-biased by stabilized dc sources, and MWs were applied resorting to an RF line - bonded to one of the chip pads - at a distance of ~ 2 mm from the nanodevice. In Figure 6.1(b-inset), quantum dots labelled 1 and 2 are connected in series and coupled to source and drain leads via tunnelling barriers characterized by resistive and capacitive components and are also capacitively coupled to external gate voltages (only side gates indicated) [77]. The device control scheme [190] exploits three global gates (one back and two sides) acting on the DQD [56] rather than local gates acting separately on each QD, and the control over the DQD filling and detuning stems from the average (balanced) and Stark (unbalanced) components of the electric field, respectively. Slight differences in the axial length and in the occupied electron

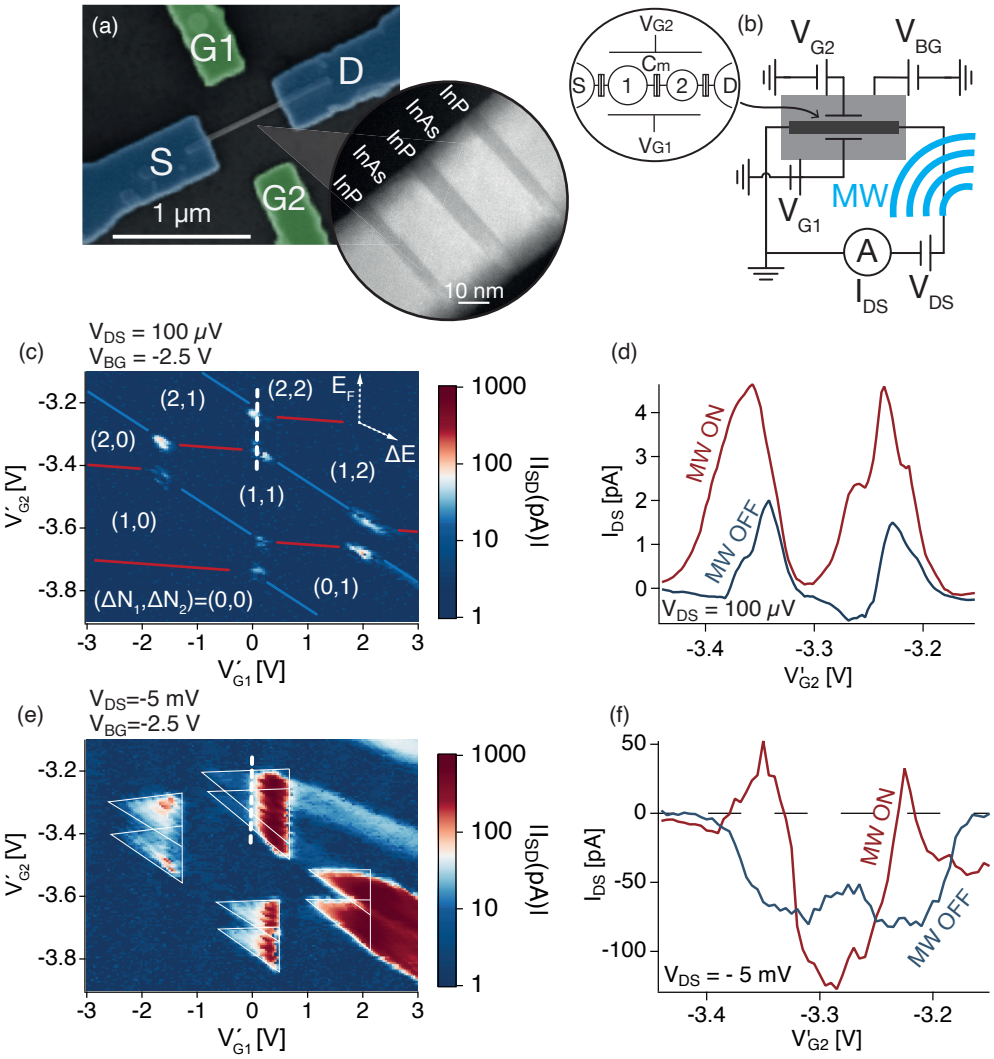

FIG. 6.1: (a) Scanning electron micrograph of one of the measured devices, comprising of source (S) and drain (D) contacts and gate electrodes (G1,G2). Inset: Scanning tunnelling electron micrograph of an InAs/InP nanowire double quantum dot (NW-DQD) used in this work. (b) Pictorial view of the experimental setup. The source measure unit (SMU) is used to voltage bias (V_{DS}) the nanodevice and measure the current intensity (I_{DS}). Microwaves are fed through an external antenna. Inset: model of the DQD system. The two QDs are represented by conductive islands connected in series and connected to source and drain contacts through tunnelling barriers. Global gates - sidegates and backgate (not represented in the model) - control the DQD filling and provide a transverse electrostatic field to achieve detuning by exploiting the quantum confined Stark effect. (c) Stability diagram of the NW-DQD, with triple points marking the edges of regions with fixed occupation number, labelled with $(\Delta N_1, \Delta N_2)$. $\Delta N_{1(2)}$ marks the number of additional electrons present in QD 1(2) with respect to a reference point. (d) Current response with and without microwave excitation along the filling direction of the DQD stability diagram, passing across two triple points (white dotted line). (e) Stability diagram measured with finite voltage bias applied ($V_{DS} = -5$ mV; characteristic current triangles marked by white contour. (f) Current response with and without microwave excitation, at finite bias, Measured along the dotted white line in (e).

orbitals in the two dots provide the system asymmetry enabling the Stark control. In this frame, the charge stability diagram is measured as a function of effective gate voltages V'_{G1}, V'_{G2} corresponding to linear combination of the voltages applied to the physical global gates (see chapter 6.1.1).

Figure 6.1(c) and Figure 6.1(e) report the color plots of the S-D current, I_DS, measured as function of V'_{G1} and V'_{G2}, for vanishing and finite S-D bias voltage applied, respectively. At vanishing SD bias (Figure 6.1(c)), transport is permitted only when the chemical potentials of S and D leads are aligned to the QD addition energies: this configuration corresponds to the white-coloured point-like current spots arranged in a honeycomb fashion in Figure 6.1(c). In the top-right corner of the current map, the dashed arrows labelled E_F and ΔE indicate the filling and detuning directions of the DQD, respectively. Along the filling direction, the total number of electrons confined in the DQD increases together with the electron population of each dot. Along the detuning direction, the number of electrons confined in the DQD remains constant while electrons redistribute in the two QDs. According to the electron population in the left and right dot (or dot 1 and dot 2 as in Figure 6.1(b-inset), different regions of the charge stability diagram are labelled (i,j) with i, j number of electrons inside dot 1, 2, respectively. Consistently, the locations of the current spots are referred to as triple points, because they connect three regions of the stability diagram with different electron population, as for instance the regions (1,1), (2,0) and (2,1). At finite SD bias (Figure 6.1(e)), for each triple point a finite energy window opens in which transport is allowed, and a current triangle is observed in the stability diagram. From the analysis of the stability diagrams at both vanishing and finite SD bias and resorting to the model illustrated in Figure 6.1(b), all physical parameters identifying the DQD can be extracted [77], including the charging and electrostatic coupling energies, the gate lever arms and the energetics of the DQD (chapter 6.1.1). For instance, for one of the measured devices the following values were extracted: lever arms $\alpha_{G1} = 20 \pm 2$ meV/V and $\alpha_{G1} = 18 \pm 2$ meV/V, dot capacitances of $C_1 = 23 \pm 3$ aF and $C_2 = 21 \pm 3$ aF, charging energies and electrostatic coupling energy of $E_{C1} = 8.1 \pm 1$ meV, $E_{C2} = 8.7 \pm 1$ meV and $E_{Cm} = 3.3 \pm 0.1$ meV, respectively. In all measured devices we observe a distribution of these parameters not exceeding the 30 % of the values reported above.

6.1.1 *Device control and gate configurations*

In order to control the device fillings and explore the stability diagram we employ the approach described in [56], using three gates: a backgate V_{BG} and two sidegates V_{G1}, V_{G2}. They all concur in the determination of the electron filling in the device by shifting the ad-

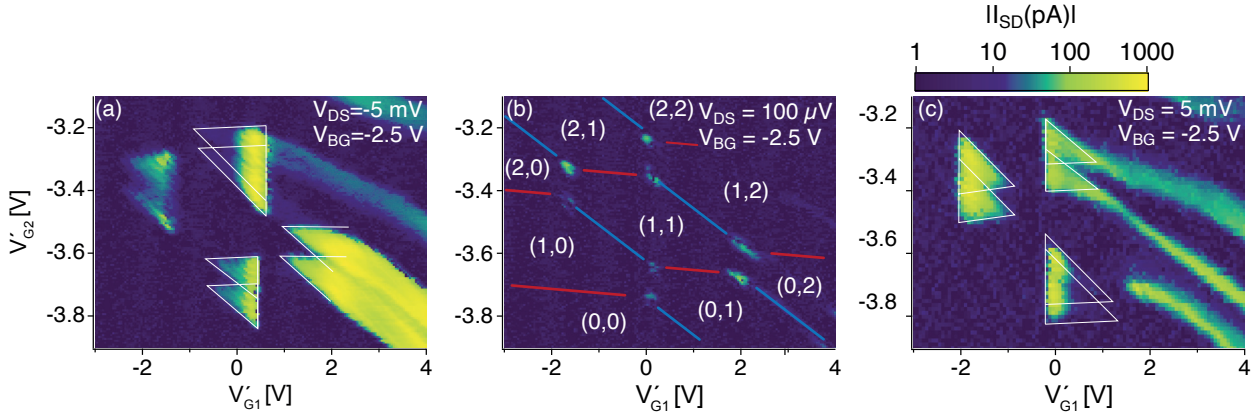

FIG. 6.2: Stability diagram of the DQD and negative, close to zero and positive V_{DS} bias.

dition energies. Any asymmetry in the gate voltages will determine the presence of a transverse field that differently affects the electronic wave function of the two QDs. This is in part due to the asymmetry in the QD sizes, in part to the intrinsic differences in the orbital's shapes. The squeezing of the orbital wavefunctions will determine distinct evolution of addition energies of the two QDs, allowing a control over the DQD configuration comparable to the typical picture of having distinct electrodes controlling each QD. In a first approximation we could consider the QDs filling and detuning to be controlled by the gate voltages average and difference respectively. In practice this is rarely the case: asymmetries between the gates and the indirect detuning mechanism are such that the most efficient gate combination must be experimentally determined for each device. V_{BG} is fixed at a value close the pinch-off, in order to get to the small electron number regime. The V_{G1} and V_{G2} are the used to explore the stability diagram in this confined range. The employed gate combinations are: $V'_{G1} = \frac{1}{\sqrt{2}}(V_{G2} - V_{G1})$ and $V'_{G2} = \frac{1}{\sqrt{2}}(V_{G1} + V_{G2})$.

6.2 MICROWAVE DETECTION

6.2.1 *MW effect on the stability diagram*

Figure 6.1(d) reports current traces measured along the filling direction in the zero-bias stability diagram (dashed line in panel (c)) without (blue curve) and with (red curve) MW applied to the device. The two peaks, corresponding to the two triple points connecting clock-wise the regions (1,1), (2,1), (2,2) and (1,2), display marked amplification (current intensity increase) as well as broadening upon application of the MW field. Figure 6.1(f) highlights the effect of the MWs over the current profile connecting along the filling direction a pair of current triangles measured at finite bias ($V_{DS} = -5$ mV).

Here, the MW-off current trace (blue curve) is robust (order of 100 pA) and always negative (according to the bias sign) and display a faint symmetric trend with respect to the effective gate voltage -3.3 V. With MW turned ON, the current profile (red curve) maintains its symmetry but exhibits a reversal of the derivative with respect to its MW-off counterpart as well as a sign reversal, with two peaks of positive current separated by a marked dip of negative current. In the following we shall investigate in detail the MW response of NW-DQD devices in both zero and finite bias configurations as function of effective gate voltages and MW nominal power, ruling out thermal effects and providing a phenomenological model to rationalize the observed results.

6.2.2 *Probing MWs at zero V_{DS} bias*

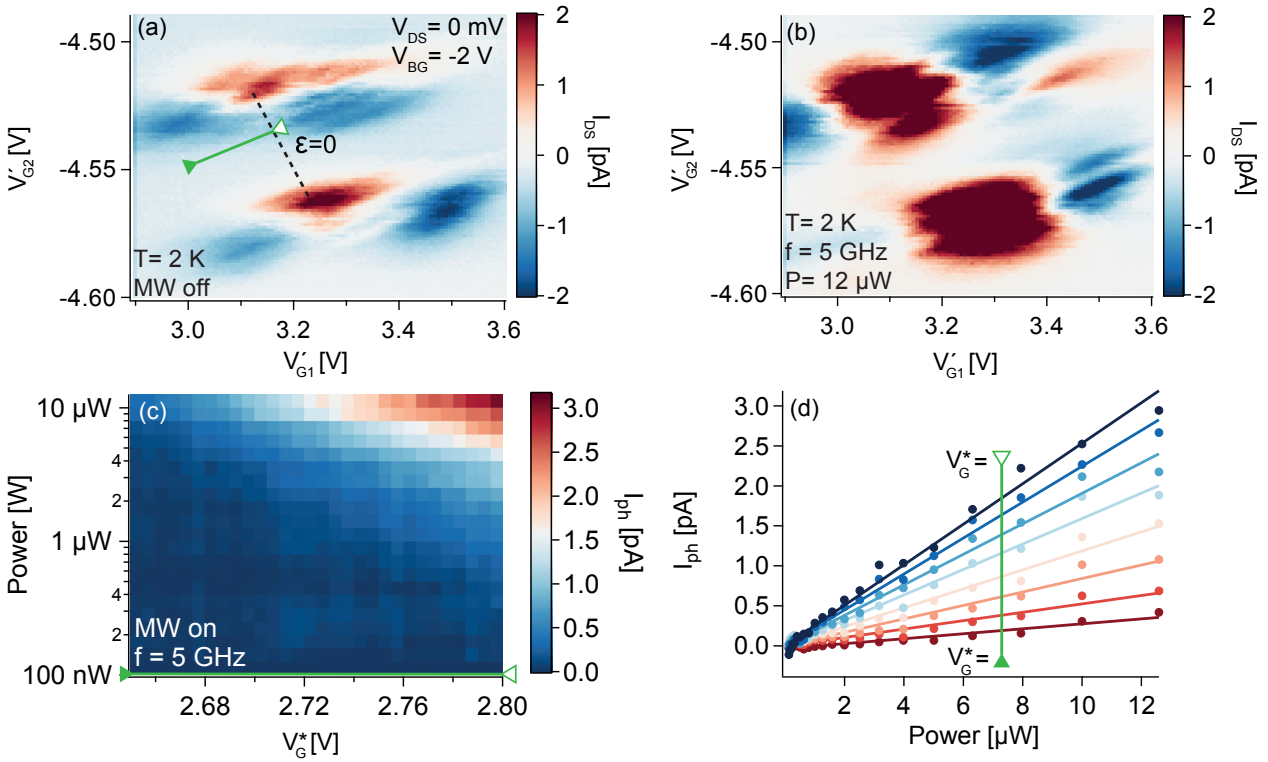

FIG. 6.3: Current triple points measured at vanishing bias without MW excitation (a) and upon nominal MW input power of 12 μW. The green line indicates the detuning direction, defined by the effective gate voltage $V_G^\star$. The open (full) triangle corresponds to zero (maximum) detuning. (c) Photocurrent map as function of $V_G^\star$ and MW power, at fixed frequency. (d) Vertical cuts of the current map reported in (c), i.e., photocurrent curves as function of MW power for different values of $V_G^\star$. Linear fitting curves are reported and used to estimate the responsivity R.

Figure 6.3 illustrates the effect of the MW field on the NW-DQD charge stability diagram at zero V_{DS} bias, focusing on a pair of triple points. In absence of a MW field, the triple points appears as reported in Fig. 6.3.a, where the filling (or zero-detuning, $\epsilon = 0$) and detuning

(ΔE in Fig.6.1a) directions correspond to the dashed-black and green lines, respectively. Fig.6.3.b reports the charge stability diagram measured upon the application of MWs with frequency of 5 GHz and power of 12 μW: the triple points are emphasized by the MWs, with an overall increase of the current level and a widening of each triple point along the filling and detuning directions. The photo-current (I_{ph}) map shown in Fig. 6.1.c displays the evolution of the dc current profile measured along the green segment in Fig.6.1.a (detuning direction) as a function of the applied MW power (accounting for the attenuation along the RF lines) in the range from 100 nW to 12 μW: the current increases markedly from the bottom-left corner of the color plot to the top-right corner. Figure 6.3.d reports I_{ph} as function of the MW power, for different values of the effective gate voltage $V_G^\star = 0.28 \times V_{G1} + 0.96 \times V_{G2}$ spanning the entire segment until the end marked with an open triangle, which matches the zero detuning condition (see Fig.6.3.a). Thus, each dataset (set of points with fixed color) corresponds to a vertical cut of the map in Fig. 6.3.c. Notably, all the measured photocurrent traces reported in Fig. 6.3(d) are linearly proportional to the input MW power, as evidenced by the solid curves in Fig. 6.3.d that correspond to linear fits of the experimental points: this clearly indicates that NW-DQD devices may operate as power law MW detectors.

The response of the NW-DQD devices as MW detector can be quantified resorting to the responsivity R, a key figure of merit measuring the intensity of the output signal for a given input power. R can be extracted as the slope of the linear fit of I_{ph} as function of the MW power. An alternative way to quantify the detector response consists in reporting the quantum efficiency $\eta = \frac{n_e}{n_{h\nu}}$, which measures the photon-to-charge conversion as the number of photoelectrons generated for each impinging MW photon.

Using the nominal MW power, we extract for our devices a maximum responsivity at zero detuning (open triangle in Fig.6.3.a,c-d) corresponding to $R = 250 \pm 10$nA/W and a quantum efficiency of the order of 10^{-12}. However, the realistic estimate of the detector figure of merit relies on the estimate of the radiated power at the antenna, assuming irradiation with cylindrical symmetry. Taking into account this normalization we estimated an equivalent intrinsic responsivity $R \sim 7$mA/W and quantum efficiency $\eta \sim 5 \times 10^{-7}$, comparable with those reported for other nanoscale semiconductor detectors [108, 109]. We also extracted the noise equivalent power (NEP) - the noise in the detection system defined as the input power for which a signal-to-noise ratio of 1 is obtained in a 1 Hz measurement bandwidth[191] - obtaining NEP $= 40$ pW$/\sqrt{\text{Hz}}$ (chapter 6.2.2.1). Remarkably, the values reported above for R, η and NEP are based on zero-bias spectroscopy measurements and implicitly assume unitary absorption of the MW radiation in the NW cross-section, hence they clearly

represent lower thresholds for the actual detector figures of merit. As will be clarified in the following section, resorting to finite-bias spectroscopy measurements allows us to extract the system impedance and to provide realistic and surprisingly high estimates for the three figures of merit. The entire study reported above at 5 GHz was carried out at different frequencies without observing any significant difference, except for the expected frequency dependent attenuation of the experimental setup. Importantly, the occurrence of transport features substantially unaffected by the change of the MW energy suggests that we can exclude photon assisted tunnelling from the possible mechanisms of interaction between the DQD and the MW [76, 103].

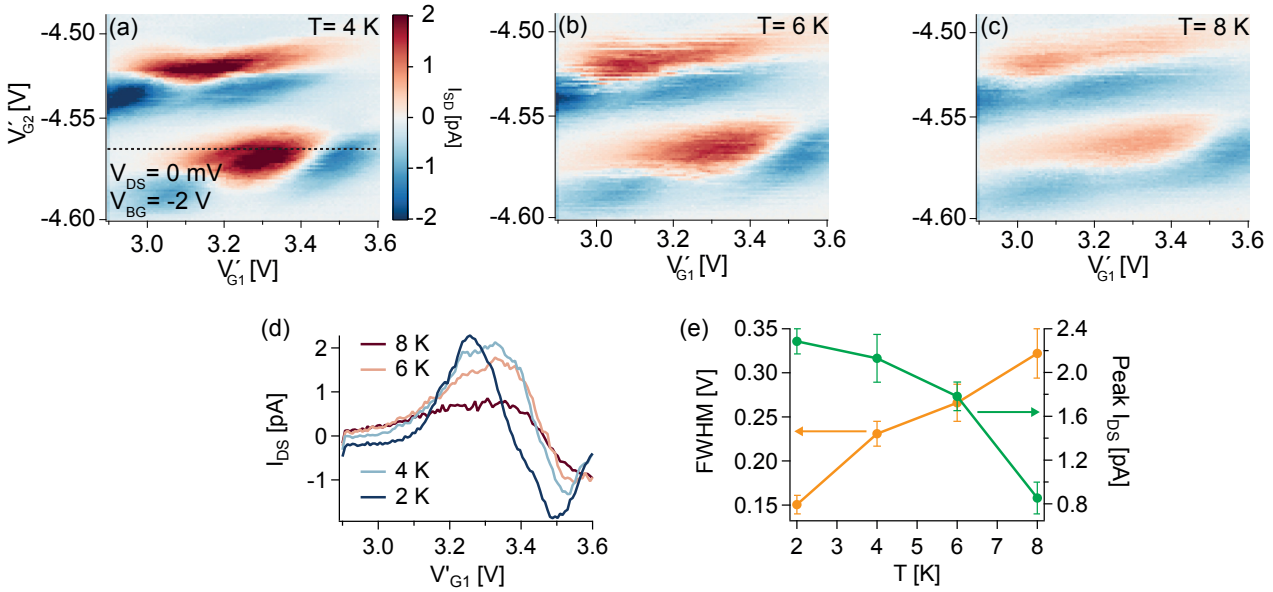

FIG. 6.4: (a,b,c) Current maps at triple points measured at T=4 K (a), T=6 K (b) and T=8 K (c). (The map at T=2 K is reported in Figure 6.3a). The effect of temperature on the stability diagram differs abruptly from the effect of the MW shown in Figure 6.3b. (e) Current traces measured along the dotted line in (a) at different temperatures. (f) Full width at half maximum (FWHM) and positive current peak intensity extracted from (e).

Moreover, the features observed in the current maps upon the application of a MW field are not ascribable to trivial heating effects potentially associated to the impact of the MWs, resulting in a temperature increase at the nanodevice. This was ascertained by addressing the effect of temperature on the stability diagram at MW-OFF, measuring the same pair of triple points at four different temperatures in the range 2-8 K, as reported in Fig.6.3.a and Fig.6.4.a-c. Fig.6.4.e reports the current profiles measured along the black dashed line shown in Fig.6.4.a at T = 2 K, 4K, 6K and 8 K. For each curve, from the current peak observed at gate voltage of about 3.3 V, we extracted the FWHM and the intensity. The results of this analysis, reported in Fig.6.4.e, clearly indicate that a temperature increase induces an overall broadening of the current features accompanied by a drastic

decrease of the current intensity: this is absolutely not consistent with the strong increase of the current level due to the application of MWs, as reported in Fig.6.3.b. In addition, together with temperature effects, we also exclude thermoelectric effects due to asymmetric heating at the leads that may establish a temperature gradient. Indeed, such effects typically activate phonon assisted transport mechanisms that yields to the occurrence of very peculiar transport features, namely triangularly shaped current side bands with sign reversal in the stability diagram [36, 192], that we never observed in our experiments.

6.2.2.1 *Calculation of the quantum efficiency*

The previous chapter describes the procedure used in order to estimate the detector's responsivity. This is a figure of merit that measures the whole device sensitivity to the radiation, considering the power emitted by the MW source and the known attenuation along the RF lines. We can use this result to estimate a different figure of merit: the quantum efficiency $\eta = \frac{n_e}{n_{h\nu}}$. $n_e = I/e$ is photocurrent divided by the electron charge, i.e. the number of electrons emitted because of the incident radiation. $n_{h\nu} = P/h\nu$ is the rate of incident photons, obtained by dividing the impinging microwave power by the photon energy. From the responsivity we obtain $\eta = 5 \times 10^{-12}$.

In order to estimate the proper quantum efficiency of the photon-to-charge conversion process we need to estimate the fraction of the emitted power gets absorbed by the nanowire. First we use the reflectivity of the RF line to estimate the emitted power at the antenna end. From VNA data we estimate an average reflectivity $S11 = -2.5$ dB $\simeq 0.56$ W/W. We then assume that the MW power is symmetrically irradiated by the wire bonding antenna, therefore a 1 μm nanowire at $\sim$ 2 mm distance can at most absorb $\sim 8 \times 10^{-5}$ of the emitted power. Accounting all of these factors we get an efficiency $\eta \sim 10^{-7}$. This is to be considered as a lower threshold of the actual quantum efficiency, since we considered full absorption by the nanowire. Any absorption below 100% would have the effect of increasing the quantum efficiency in this estimate. Equivalently we can obtain a value of the internal Responsivity that neglects the power lost in the antenna-detector coupling: $R \sim 7$ mA/W. Finally we compute the value of the current noise (N) in our setup for the used integration time. Together with the responsivity we can use this information to estimate the Noise Equivalent Power (NEP).

$$NEP = \frac{N}{R} \times \sqrt{t_i} \tag{6.1}$$

where t_i is the integration time, related to the measurement bandwidth (BW) by the Nyquist theorem $t_i = \frac{1}{2 \times BW}$. The value of the NEP obtained is NEP $= 41$ pW$/\sqrt{\text{Hz}}$. This same value can be graphically obtained from figure 6.5.

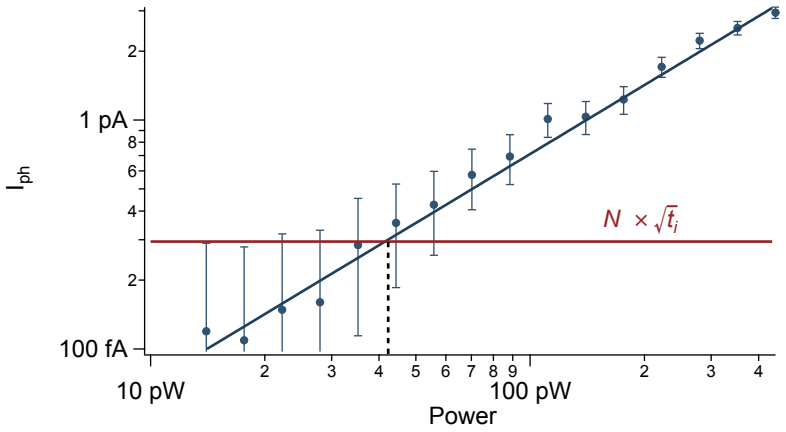

FIG. 6.5: Photocurrent as a function of the microwave power, corrected for all of the estimated losses, and fitting from which the responsivity value was obtained. The intersection with the line of value $N \times \sqrt{t_i}$ marks the condition of signal-to-noise ratio equal to 1. The corresponding power is the NEP.

6.2.3 *Probing MWs at finite V_{DS}*

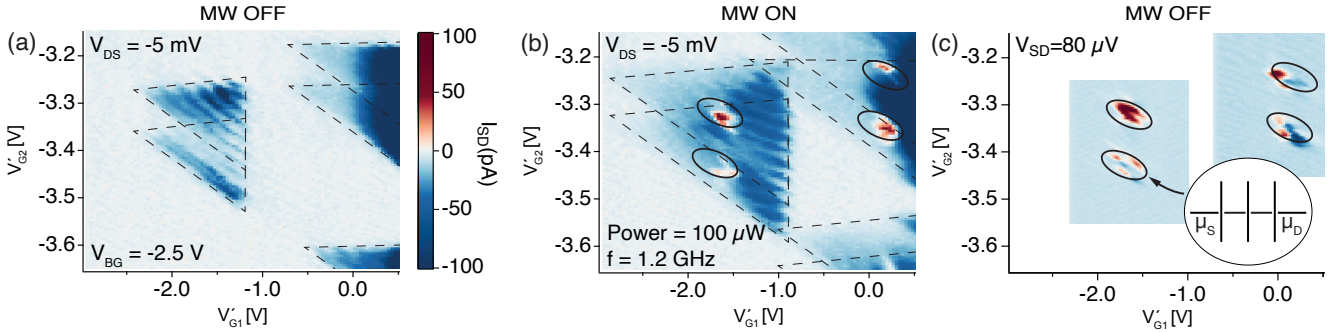

FIG. 6.6: Current triangles measured at finite bias without MW excitation (a) and upon nominal MW input power of 100 μW (b). Black dotted lines mark the edges of the current triangles. Black circles in (b) mark the onset of four current spots with sign reversal with respect to the full triangles. (c) Current triple points measured at vanishing bias, marked with black circles. The locations of the black circles in panels (b) and (c) show an excellent match.

The high figure of merit envisioned in InAs/InP NW-DQDs coexists with the possibility to operate the nanodevices as calibration-free or absolute MW detectors, a unique feature which stems on the peculiar transport characteristics displayed by DQDs at finite V_{DS}. Figure 6.6(a) reports two pairs of current triangles measured at $V_{DS} = -5$ mV and MW-off. The current is significantly quenched at the base of the left triangles with respect to the right ones, consistently with a Pauli spin blockaded transport in the left triangle pair. Fig.6.6(b) reports the charge stability diagram measured upon the application of MWs with frequency of 1.2 GHz and power of 100 μW. Overall, the impact of the MWs is two-fold, including a magnification of the

size of each current triangle as well as the rise of two current spots with sign reversal with respect to the main triangle (positive current spots inside negative current triangles).

Regarding the triangle magnification effect, we notice that in dc bias spectroscopy experiments the widening of triangles is proportional to the increase of V_{DS} and corresponds to an increased range of energetic configurations fitting inside the bias window [77]. This bring us to introduce an effective bias V_{DS}^{eff} accounting for the triangle magnification due to the MWs. With the energetics of the NW-DQD known from the finite bias spectroscopy at zero power MWs (chapter 6.1.1), we estimate that the increased triangle size reported in Fig.6.6.b correspond to $V_{DS}^{eff} = -10 \pm 1$ mV. This is confirmed by a direct comparison of the MW-ON stability diagram with the $V_{DS} = -10$ mV, MW-OFF stability diagram (chapter 6.2.3.2). The two current spots with sign reversal (positive current) shown in Figure 6.6(b) were actually observed also for different charge occupation configurations and for both Spin blockaded and non Spin blockaded current triangles (chapter 6.3). In all cases, the position and the relative intensities of the two positive current peaks perfectly match position and intensity of the triple points measured at $V_{DS} \simeq 0$, as reported in 6.6(c).

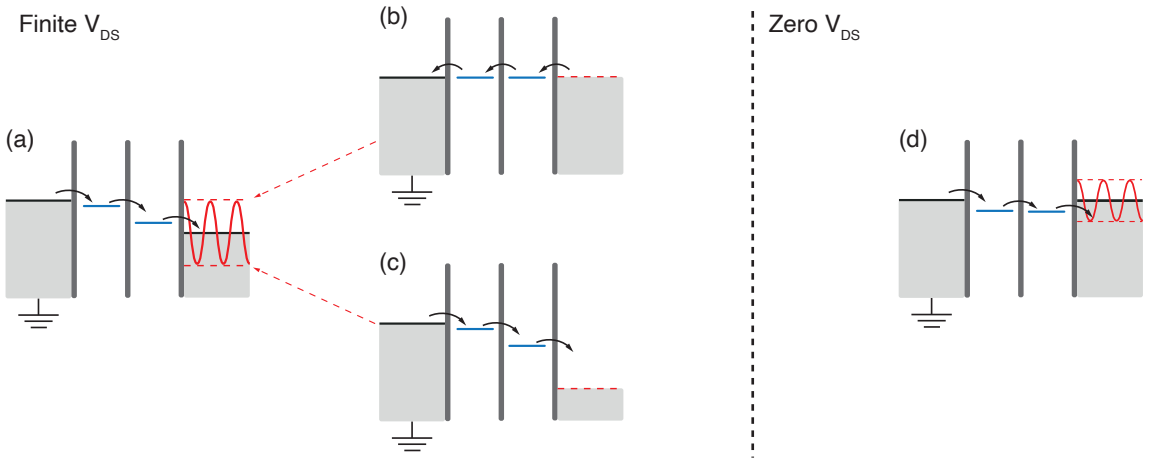

FIG. 6.7: (a) Schematic illustration of the model based on an effective AC bias (V_{AC}) used to rationalize the interaction of microwaves with NW-DQDs at finite V_{DS}. V_{AC} is assumed to couple preferentially with the drain. The oscillating potential $V_{DS}^{tot} = V_{DS} \pm V_{AC}$ (red-coloured in (a)) imposes a bias window for electron tunnelling spanning from configuration (a) to (b). (b) The effective AC oscillation brings the DQD to the minimum (zero-) voltage bias configuration. (c) the effective AC oscillation brings the DQD to the maximum voltage bias configuration. (d) Schematic illustration of the effective V_{AC} bias model used to rationalize the MW-DQD interaction at vanishing-bias.

In order to rationalize our results both at zero and finite V_{DS}, we adopt a semi-classical model of radiation-matter interaction where MWs are treated classically while NW-DQDs are in quantum transport regime, and we assume that the MW field couples preferentially with one of the leads - e.g. the drain - driving oscillations in its chemical potential. We define a total effective bias, V_{DS}^{tot}, which spans the

range $V_{DS} - V_{AC} < V_{DS}^{tot} < V_{DS} + V_{AC}$, where V_{AC} is the amplitude of the MW perturbation (Figure 6.7a). All the bias configurations in this range may contribute to electron tunnelling through the NW-DQD. The size of the current triangles is determined by the largest absolute value of the total bias i.e. $V_{DS}^{tot} = V_{DS} - V_{AC}$ (being $V_{DS} < 0$). In fact, this large bias leads to non-zero current in the widest possible range of gate voltages, corresponding to the configuration shown in Figure 6.7(c). From the previously obtained $V_{DS}^{eff} = -10 \pm 1$ mV we extract an AC voltage of $V_{AC} = 5 \pm 1$ mV. We now consider the opposite extreme of the bias range, where $V_{DS}^{tot} = V_{DS} + V_{AC}$. Starting from $V_{DS} = 5$ mV, we obtain a total voltage V_{DS}^{tot} compatible with 0 mV. Therefore we can expect the $V_{DS} \sim 0$ bias, characterised by the previously discussed triple points, to contribute to the total current. This is consistent with the position of the two positive current peaks emerging upon application of MWs. Remarkably, these peaks do not correspond to the zero detuning condition at finite bias, which is found at the base of the current triangles. The peaks emerge instead at the pure triple point positions. This is ascribable to the capacitive coupling of the drain contact with the QDs, according to which, by changing the bias, also the QDs configuration is affected. Importantly, the observation of these contributions is only possible because the currents outside of the triangle base is strongly suppressed. The same phenomenological model qualitatively explains the MW impact on the charge stability diagram at zero bias (see Fig. 6.3(b)). In fact, the shaking of the addition energies extends the region for which tunnelling is permitted along the filling direction, according to the schematic depicted in Figure 6.7(c).

In this framework, the appearance of the current reversal peaks marks the condition $V_{DS}^{tot} = V_{AC} + V_{DS} \geq 0$ and therefore the condition $|V_{AC}| = |V_{DS}|$. Strikingly, this permits to use an absolute reference - the applied bias voltage - for evaluating the local amplitude of the MW field, a physical quantity which is otherwise exceedingly difficult to measure, estimate or calculate: this purpose can be achieved without the need for any calibration and resorting to the unique transport features of InAs/InP NW-DQD detectors. The self-calibration of InAs/InP NW-DQD MW detectors [72] implies an assessment of the relationship between the effective V_{AC} and the photocurrent I_{ph}, which are measured exploiting two different device configurations. To this aim, we first estimate the electrical impedance Z from the ratio of V_{AC} and I_{ph}, obtaining 160 MΩ. Then, we compare this value to the one calculated starting from the measured DQD resistance and capacitances, obtained from the analysis of the conductive configurations in the current maps at zero and finite bias. In this case Z is dominated by the resistive component and measures 65 MΩ. These two estimates for Z, while displaying a faint discrepancy that could be filled by directly measuring the complex admittance of the device,

are sufficiently similar to validate the relationship $V_{AC} = ZI_{ph}$, which allows us to estimate the dissipated power at the device, obtaining $P_{diss} = V_{AC}I_{ph} = 1.5 \times 10^{-15}$ W. This very low experimental value accounts for both the antenna to detector losses and the non-unitary MW absorption by the device, and highlights the key role of the MW feeding system: optimal circuitry coupling the MW radiation with the NW-DQD detector yields to responsivity up to $R \sim 2000$ A/W, quantum efficiency of 0.04 and NEP of NEP $\sim 10^{-16}$ W/$\sqrt{\text{Hz}}$.

6.2.3.1 *Calculation of the device impedance*

The device impedance $|Z| = \sqrt{R^2 + \left(\frac{1}{2\pi\nu C}\right)}$ can be estimated from the knowledge of the resistance and capacitance (assuming the inductive term to be negligible). The resistance was obtained in the open channel configuration, with the energy levels of the two quantum dots aligned, by fitting the maximum current for each triangle measured at many V_{DS} values. We estimate $R = 6.5 \times 10^7$ Ω.

In order to compute the capacitance we account for the whole nanowire by scaling the value obtained for a single quantum dot to the whole nanowire length ($L_{NW} = 1.5$ μm, $L_{QD} \sim 20$ nm. We estimate therefore a capacitance $C = 1.5 \times 10^{-15}$ F. For a frequency ν =5 GHz the impedance is dominated by the resistive term. In order to estimate the same same quantity from the comparison of the measured photocurrent and the measured V_{AC} we consider the data at 12 μW, 5 GHz in both cases, where $I_{ph} = 3$ pA, V_{AC}= 0.5 mV. From this we estimate $Z = V_{AC}/I_{ph} = 160$ MΩ.

6.2.3.2 *Comparison of DC v.s AC triangle size*

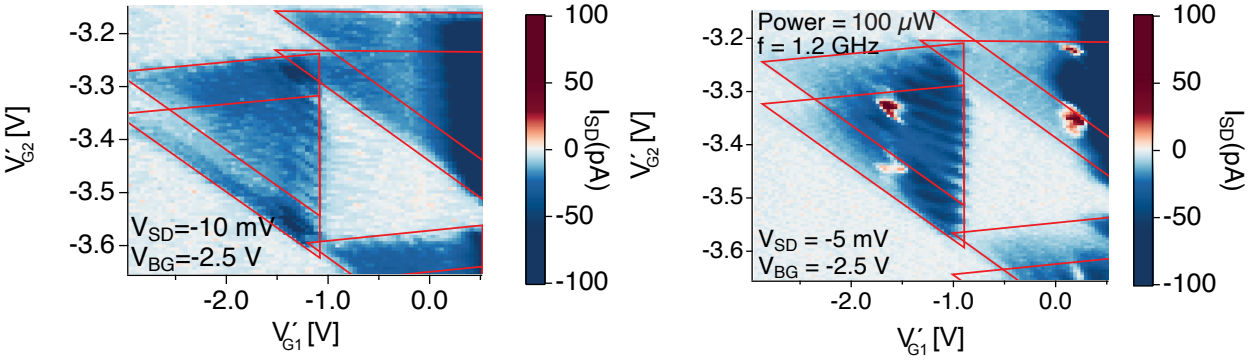

FIG. 6.8: Comparison of the current triangles with: (left) bias $V_{DS} = -10$ mV and no microwaves, (right) bias $V_{DS} = -5$ mV and microwaves turned on.

Here we show that we can directly compare the size of the current triangles and correlate the AC driven increase to the corresponding DC value. The microwave power of figure 6.8 is the same as the one reported in chapter 6.2.3, and is such that the total bias V_{DS}^{tot} matches

the DC bias of $V_{DS} = -10$ mV. The red contours confirm this: in the two cases they are identical. The only difference is a small rigid shift in gate values, which is routinely observed in DQD stability diagrams.

6.2.3.3 *Analysis of the frequency response*

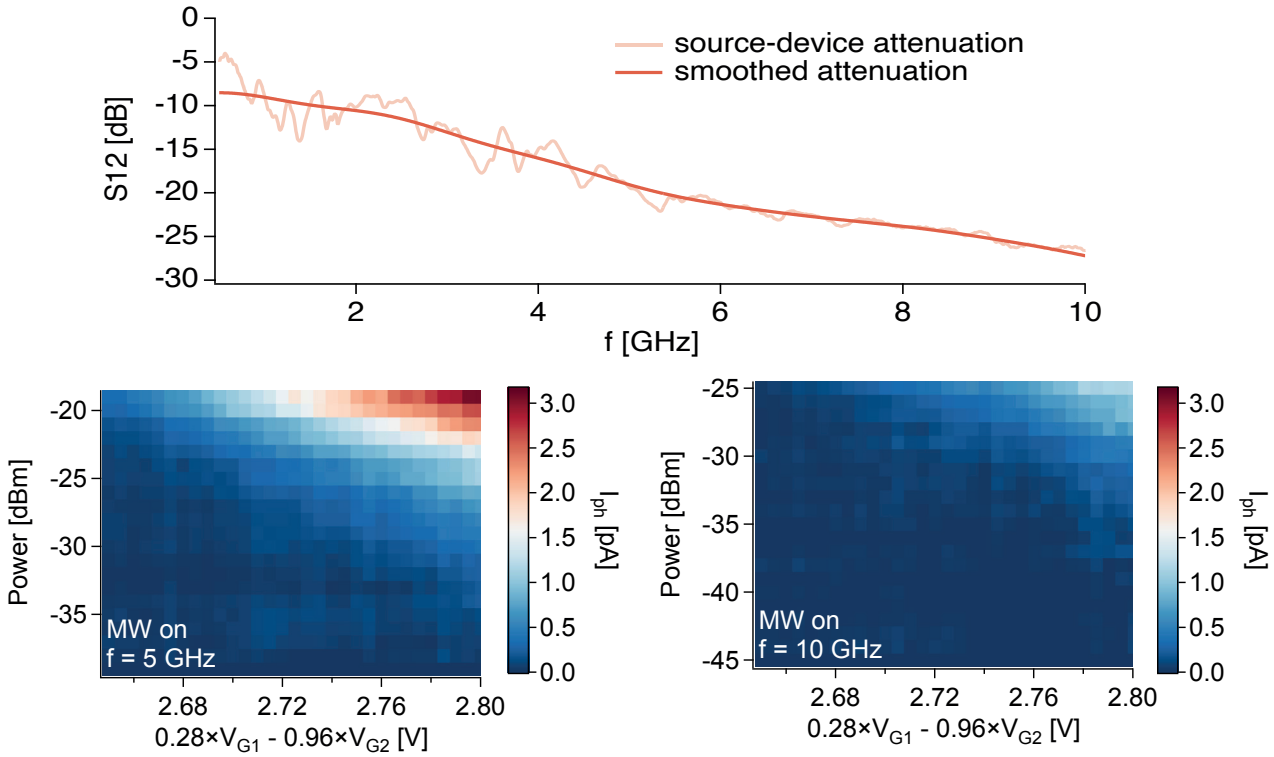

FIG. 6.9: Frequency dependent source-device attenuation of our experimental setup. Response as a function of the microwave power for selected frequencies. Because of the lower attenuation data at lower frequencies allows us to access higher output signal.

A key feature of the proposed model is that it does not require matching of photon energies to resonant transitions. Therefore we do not expect a strong frequency dependence of the response. We investigated this by probing the responses in the 1-10 GHz range and found no effect distinguishable from the frequency dependent attenuation and reflectivity of the experimental setup.

6.3 SPIN BLOCKADE

In this chapter we compare the spin blockade phenomena between different batches of InAs/InP DQDs. Complete transport measurements and energetics are reported in chapter A.3. From the energetic point of view the two systems were found to be equivalent. This is consistent with the fact that the growth parameters are similar. These are reported in table 6.1. Among the devices described in chapter A.3,

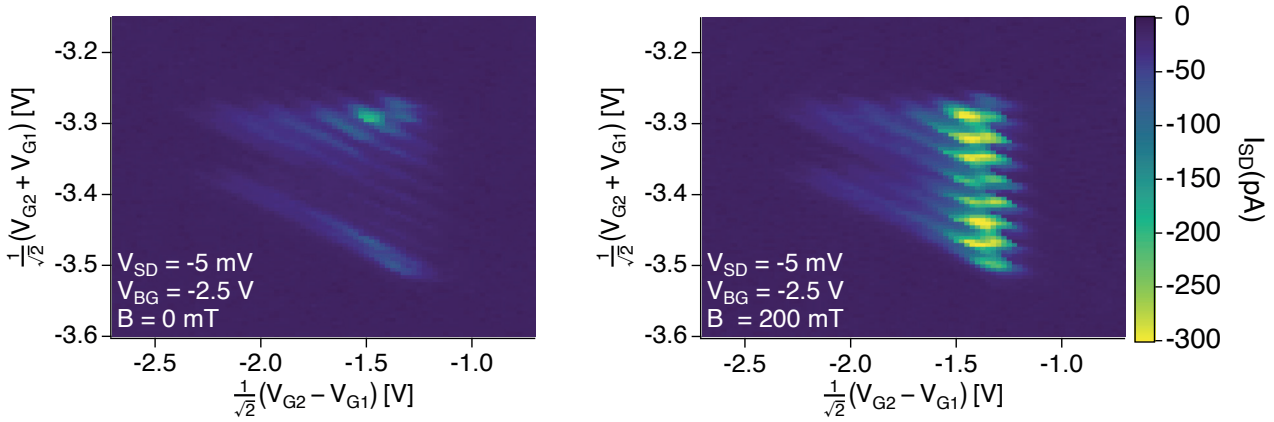

FIG. 6.10: Two maps at different magnetic fields of sample 1. In the $B = 0$ mT case the current is suppressed by the Pauli spin blockade, except for the top and bottom edges.

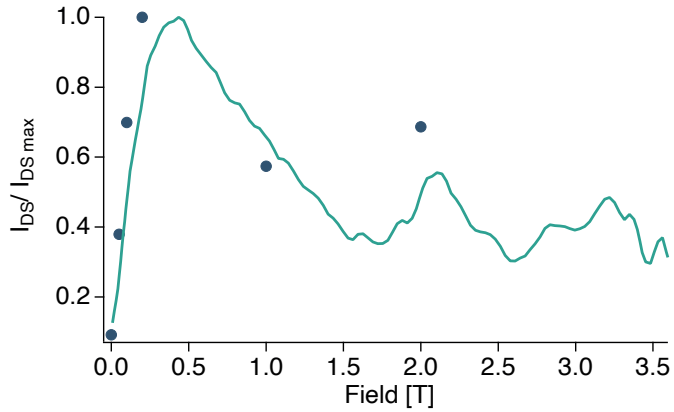

FIG. 6.11: Comparison of our data (dark blue dots) and the data from Rossella et al. (light blue line). The few measurements we have for this sample follow the same behaviour, as expected since they are different samples from the same growth batch. Data obtained from sample 1.

this section focuses on results obtained on sample 1 (batch A) and sample 3 (batch B).

	InP 1	InAs 1	InP 2	InAs 2	InP 3	Diameter	
Batch A	5	20	5	22.5	5	70	nm
Batch B	5.2	17.5	6.8	17.6	5.4	50	nm

TABLE 6.1: DQD size features of the two batches studied in this work.

Figure 6.10 shows two maps of the spin blockade current triangles of sample 1, at zero and finite magnetic field. The suppression of the current in the first case is clear and consistent with what is expected for strong inter-dot coupling: the current is blocked the most at low magnetic fields [193]. Figure 6.11 shows the current for selected field values, and the comparison with the results from [56]. The published results were obtained from another nanowire from the same nanowire growth batch: the result obtained in the two devices are consistent.

The oscillatory pattern is explained in [56] as the result of inter-dot coupling, since the exchange energy splitting is proportional to the square of tunnelling amplitude. The field modulates the exchange energy via the oscillation of inter-dot coupling. In less coupled QDs this effect is expected to be suppressed. This is consistent with what we observe in figure 6.12: sample 3, which belongs to batch B, was grown with a thicker interdot barrier, which leads to lower inter-dot coupling. This effect highlights the extreme control over the fine quantum dynamics of the DQD energy levels though precise manipulation of the growth parameters.

6.3.1 *Spin Blockade under MW illumination*

In this section we further discuss the resilience of the phenomena observed in chapter 6.2, also in the Spin Blockade triangles. Figure 6.13 shows all combinations MW on and of and with the presence of a magnetic field. The magnetic field value was chosen such that the measured current at the triangle base was the greatest: in this configuration the spin blockade is completely lifted. The MW illumination leads a partial SB lifting: an increase in the current magnitude along the triangle base is clearly visible. This effect can be compared with the SB lifting provided by applying a magnetic field. The two mechanisms are qualitatively distinct in that SB lifting does not lead to any polarity change or increase in the current triangle's size. Furthermore if we apply a magnetic field when the microwave drive is turned on we can clearly distinguish an increase in the current magnitude. Therefore the magnetic field enhances the lifting provided by the microwave radiation.

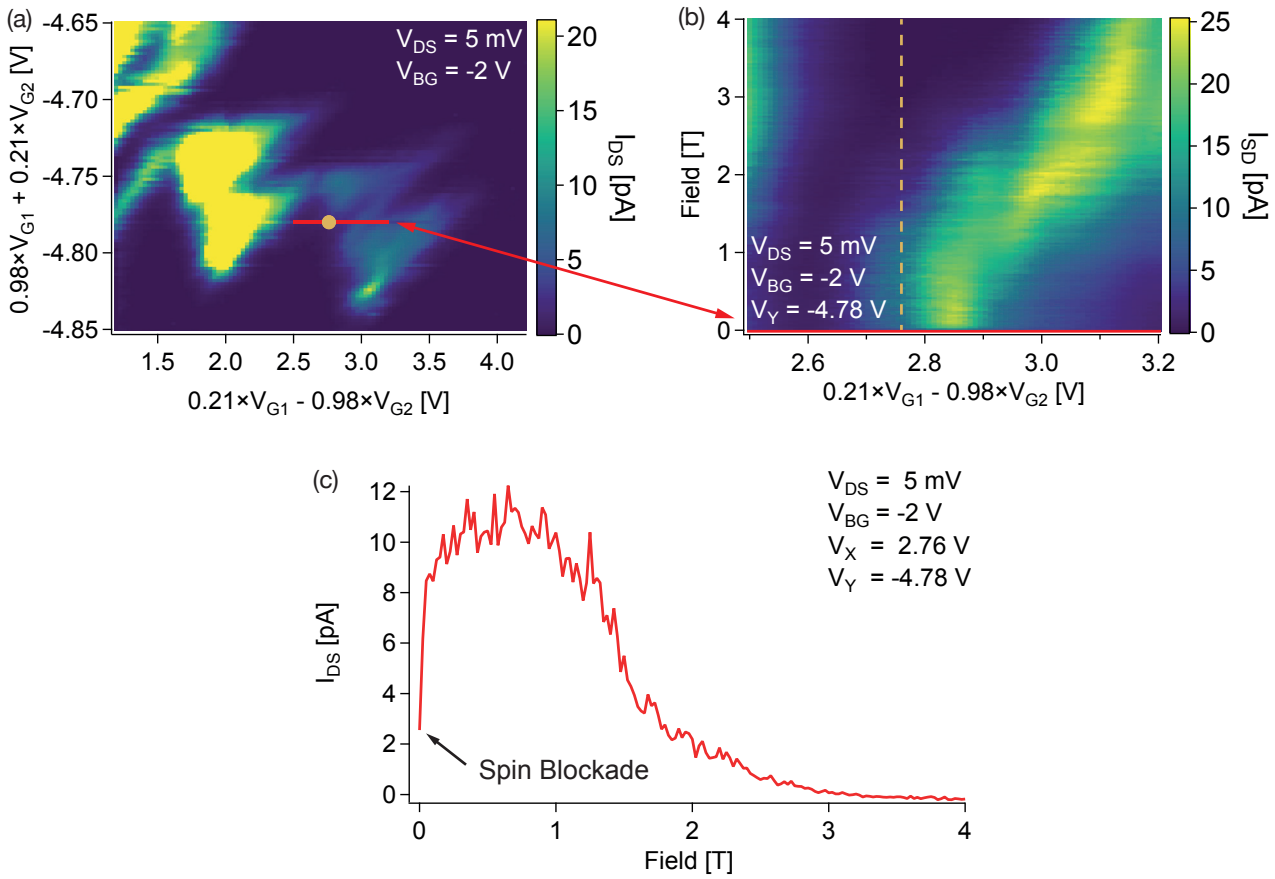

FIG. 6.12: (a) Reference triangles. (b) scan along the red curve as a function of the field. (c) curve obtained along the dotted line, corresponding to the single dot in (a) of the current as a function of the field. Data obtained from sample 3.

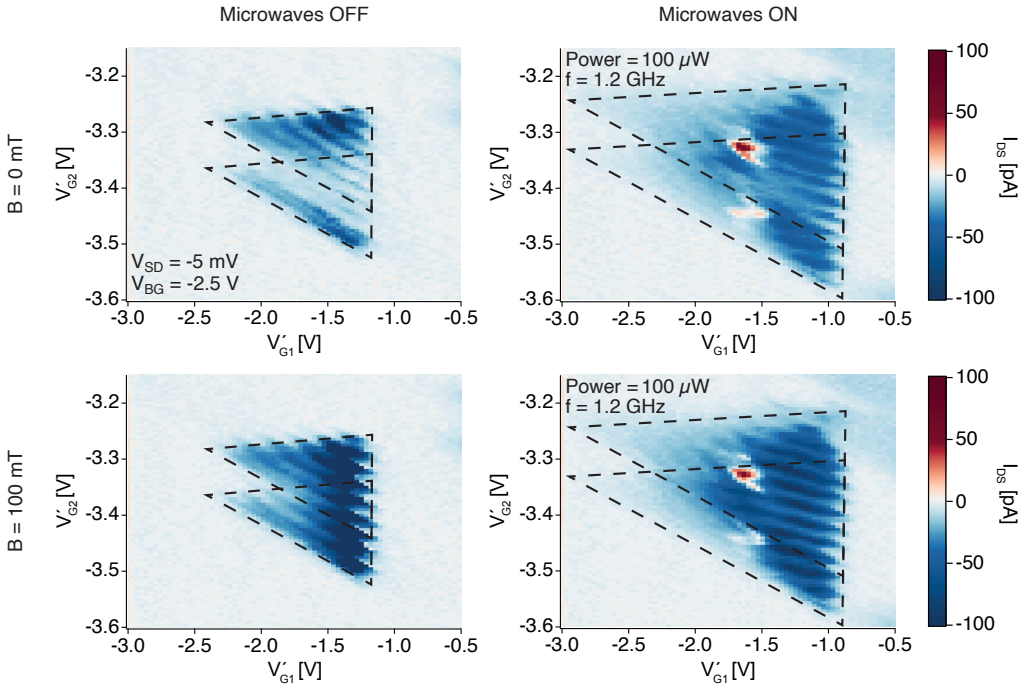

FIG. 6.13: Spin blockade current triangles at zero and 100 mT magnetic field, with MW excitation ON and OFF respectively.

6.4 CONCLUSIONS

Microwaves are efficiently detected by probing their impact on the transport properties of electrons tunnelling across a triple energy barrier implemented in InAs/InP nanowire double quantum dots. The nanodevices, equipped with source and drain electrodes and three independently biased gates, were exposed to microwave radiation in the range 1-10 GHz, and the changes induced by the microwaves in the charge stability diagram at zero and finite source-drain bias were mapped as function of the MW intensity and frequency. The results at zero bias show that our devices act as power law MW detectors, and allow to extract lower thresholds for the figure of merits - responsivity R and quantum efficiency η - and the NEP. The results at finite V_{DS} show current triangle magnification along filling and detuning directions together with the emergence of current spots with sign reversal. The experimental outcomes at both vanishing and finite bias are rationalized with a phenomenological model invoking an effective AC bias to account for the coupling between the microwaves and the NW-DQDs. Combining zero and finite-bias results with the model we envision that our devices are capable of microwave detection with impressively high figures of merit - $R \sim 2000$ A/W, $\eta = 0.04$ - and low NEP $\sim 10^{-16}$ W/$\sqrt{\text{Hz}}$. The present study demonstrates that NW-DQD devices allow to measure the amplitude of the local MW field with an absolute reference - the equivalent source-drain

bias - without requiring any calibration process. The peculiar transport features allowing for absolute MW detection, together with the high sensitivity and the nanometre-scale resolution, make InAs/InP NW DQDs a class of nanomaterials with the potentiality to act as game-changer for future MW detection platforms and applications.

Part IV

CONCLUSIONS

7

DISCUSSION AND OUTLOOK

In this work I systematically studied microwave detection by InAs low dimensional devices such as bare nanowires, single quantum dots coupled to microwave resonators and double quantum dots. All of these systems display robust microwave responses that was studied in detail in order to understand the optimal working conditions, to measure the relevant figures of merit and to rationalize the physical mechanism from which they originate.

Nanowires

Bare InAs nanowire devices display broadband rectification in the 1-10 GHz range in two architectures of direct and microstrip mediated coupling. Their response was characterized in terms of the relevant parameters such as temperature, radiation frequency and gate voltage. Two alternative regimes of operation were analysed: current detection and voltage detection. The origin of the rectification was determined through careful considerations on the relevant theoretical models, which allowed us to exclude certain modes of interaction. The use of different microwave feeding mechanisms, coupled with the gate mediated tunability of the device, allowed us to distinguish two regimes with distinct phenomenology. At low carrier densities $n \sim 10^{16}$ cm^{-3} we expect the bolometric effect to be the dominant rectification mechanism, while at high concentration ($n > 10^{17}$ cm^{-3}) damped plasma waves are expected to be active.

Quantum dots

The transport characteristics of InAs/InP nanowire QDs capacitively coupled to microwave resonators were then investigated. When sufficient power is provided, the MW field induces a broadening of the current peak and a current polarity reversal. The broadened current signal increases linearly with the microwave power and represents therefore a viable detection strategy. These results were rationalized as a shaking of the leads and simulations were performed to confirm the validity of this model, finding excellent agreement. These effects are relevant for microwave-assisted tunnelling processes in the many-photon regime and reflect the discrete nature of QDs excited states. These experiments demonstrate that a suitable choice of the working configuration, as well as of the electron wavefunction, enables the control of the tunnelling current in strongly confined NW QD systems under external MW excitation.

Double quantum dots

Finally we investigated MW detection through InAs/InP DQDs. Finite and zero bias transport measurements without MW excitation were used to characterize the devices and extract its energetics. Then, the impact of 1-10 GHz radiation on the transport features was probed at zero and finite bias, leading to unique insights. The results at zero bias show that our devices act as power law MW detectors,

and allow the determination of lower thresholds for the figure of merits: responsivity R, quantum efficiency η and NEP. The results at finite V_{DS} show current triangle magnification along filling and detuning directions together with the emergence of current spots with sign reversal. The experimental outcomes at both vanishing and finite bias are rationalized with a phenomenological model invoking an effective AC bias to account for the coupling between the microwaves and the NW-DQDs. The physical properties extracted with the transport measurements without MW were used to link the features observed in the two regimes. Through optimal MW coupling we envision that our devices are capable of microwave detection with impressively high figures of merit - $R \sim 2000$ A/W, η= 0.04 - and low NEP $\sim 10^{-16}$ W/$\sqrt{\text{Hz}}$. This work demonstrates that NW-DQD devices can measure the amplitude of the local MW field with an absolute reference - the equivalent source-drain bias - without requiring any calibration process. The peculiar transport features allowing for absolute MW detection, together with the high sensitivity and the nanometre-scale resolution, make InAs/InP NW DQDs a class of nanomaterials with the potentiality to act as game-changer for future MW detection platforms and applications.

Performance comparison

The same procedure discussed in chapter 6.2.3 can be applied to the bare nanowire and QDs. Namely, the device impedance can be calculated at the optimal detection condition. The dissipated power at the device can be compared to the nominal input power in order to estimate the power losses due to non-optimal coupling of the MW line to the detector. This allows the calculation of the limit figures of merit for the devices, in the case of optimal MW coupling.

	Coupling	Measured R_I	Attenuation	Potential R_I	Potential η	Potential NEP
NW	direct	1.8 mA/W	2×10^{-4}	10 A/W	10^{-5}	1×10^{-10} $\frac{\text{W}}{\sqrt{\text{Hz}}}$
QD	indirect, resonator	1.4 mA/W	10^{-6}	1000 A/W	4%	3×10^{-16} $\frac{\text{W}}{\sqrt{\text{Hz}}}$
DQD	indirect	250 nA/W	10^{-10}	2000 A/W	4%	1.5×10^{-16} $\frac{\text{W}}{\sqrt{\text{Hz}}}$

TABLE 7.1: Coupling method, measured responsivity and estimated potential figures of merit for the three architectures studied: nanowires, quantum dots and double quantum dots.

Table 7.1 shows a comparison of the figures of merit obtained and estimated in the three devices discussed. The estimated attenuation, as well as the measured responsivities R_I, highlight the importance of the MW feeding mechanism. Between the direct and indirect connection of the detector to the MW feed we estimate a 6 orders of magnitude difference in the attenuation. In the direct case the MW feed line is connected directly to one of the nanowire extremes though wire bonding. In the indirect case the wire bonding is used as a radiating antenna in the vicinity of the detector. The QD case, which exploits the superconducting resonator for enhanced coupling but

that is connected indirectly, shows an intermediate value of attenuation: the focusing effect of the resonator is strong but significant losses are still present because of the indirect coupling. QD and DQD show similar potential in terms of figures of merit, with the QD being simpler to fine tune towards the high sensitivity region, since it requires the optimization of just one gate voltage against the two of the DQD. Yet the DQD might be more appealing in certain applications thanks to the calibration free operation. The NW shows the worst figures of merit out of the three but is significantly simpler to configure, since the response is stable in a wide range of gate values, has two modes of detection, current and voltage, as well as the advantage of working in a wide temperature range (20-300 K).

Future perspectives

The results of this work provide the foundation for the application of nanowire devices for microwave detection. The investigation of the physical mechanisms at play in the detection is essential in order to provide the necessary tools for the optimization of future devices. For example, nanowire devices can be gate tuned close to the pinch-off in order to use them as bolometric sensors, while at high gate voltages current measurements become a viable detection strategy. The sharp features of QD result in narrow voltage windows for MW detection, therefore the strong responsivity is obtained only through careful control or the device configuration. In DQD we showed remarkable calibration free detection. Since the photocurrent depends on the DQD impedance, optimization of this parameter might lead to an increase of the responsivity. The measurements performed in all configurations underscore the importance of the MW feeding mechanism. Impedance matching a nanowire to the microwave circuitry, while not an easy task, is fundamental in order to fully exploit the detection characteristics of the nanowire devices discussed here. Through proper MW feeding many orders of magnitude can be gained in the figures of merit, making this kind of device competitive with state of the art solutions.

Part V

APPENDIX

A

APPENDIX

A.1 FABRICATION PROTOCOLS ADOPTED

A.1.1 *Optical Lithography: etch 330 nm YBCO + 200 Au*

- Clean sample with acetone and isopropyl alcohol (IPA)
- Deposit resist Shipley S1813
- Spin (6000 rpm/s, 4000 rpm, 46 s)
- Soft bake 115° C, 60 s
- Expose (9 mW/cm^2), 20 s * + 2 × 40 s edge bead)
- Develop AZ 726 MIF 30 sec
- Optional hard bake Soft bake 115° C, 60-90 s
- Etch RIE: Pressure 20 mTorr, Radio frequency power = 250 W, Argon flux = 20 sccm, time=(180 s, + 20 s stop)× 23
- Clean sample with acetone and isopropyl alcohol in ultrasound bath

A.1.1.1 *Optical Lithography: etch 200 Au*

- Clean sample with acetone and IPA
- Deposit resist Shipley S1813
- Spin (6000 rpm/s, 4000 rpm, 46 s)
- Soft bake 115° C, 60 s
- Expose (9 mW/cm^2), 20 s * + 2 × 40 s edge bead)
- Develop AZ 726 MIF 30 sec
- Etch RIE: Pressure 20 mTorr, Radio frequency power = 250 W, Argon flux = 20 sccm, time=(120 s, + 20 s stop)× 4
- Clean sample with acetone and isopropyl alcohol in ultrasound bath

A.1.1.2 *Optical Lithography: negative photoresist*

- Clean sample with acetone and IPA
- Optional bake 100° C, 5 minutes to completely dry and improve adhesion.
- Deposit resist ma-N1420
- Spin (500 rpm/s, 3000 rpm, 60 s)
- Soft bake 100° C, 120 s
- Expose (4.5 mW/cm^2 at 365 nm, 20 s
- Develop in ma-D 533/ S 80 sec
- If used for lift-off, do it in hot acetone. Use a syringe to create an acetone jet on the device, this should lift all of the excess gold. Check under the optical microscope without removing from the liquid (once dried the excess gold sticks to the surface). Depending on the adhesion strength of the deposited materials, ultrasounds can be used to aid lift-off (for example Au/Cr/SiO_2 is very strong, Au/Ti/sapphire not so much).

A.1.1.3 *Optical Lithography: lift-off with positive photoresist*

- Bake 120°C, 5 minutes
- Deposit LOR 3A, sacrificial layer
- Spin (3000 rpm, 60 s)
- Bake 150°C, 5 minutes
- Deposit resist Shipley S1813
- Spin (6000 rpm/s, 4000 rpm, 46 s)
- Soft bake 115° C, 60 s
- Expose (9 mW/cm^2), 20 s
- Develop AZ 726 MIF, 60 sec
- Evaporate 10 nm Cr/Ti and 100 nm Au.
- Lift-off in acetone as described above.
- Remove LOR 3A with AZ 726 MIF or other TMAH based developer. O_2 plasma might work too.

A.1.1.4 *EBL: deposit contacts*

- Clean sample with acetone and IPA
- Bake 120°C, 5 minutes
- Deposit resist PMMA AR679.04 (950K, 4%)
- Spin (4000 rpm, 60 s)
- Bake 120°C, 5 minutes
- Expose (30 kV, 500 $\mu C/cm^2$, step size 8 nm, working area 200 $\times$ 200 μm, 7.5 or 30 μm aperture)
- Develop: AR600-56 2 min, stop IPA 30 s)
- Dry N_2
- Evaporate 10/90 nm Ti(Cr)/Au
- Lift-off in acetone
- Clean sample with acetone and IPA

A.1.1.5 *Passivating solution*

- mix 1.12 g sulphur and 6 ml ammonium sulphide
- Leave in magnetic agitator for one night
- Add 54 ml H_2O
- Mix for 2 h
- leave in opaque bottle with N_2 atmosphere

A.1.1.6 *Cleaning of sapphire substrates*

Modified RCA procedure[194]:

- Ethanol soak overnight (tot 24h)
- Sonication in H_2O and glassware detergent (1 h)
- SPM: H_2SO_4 + H_2O_2 (3:1) 20 minutes at 80°C
- HNO_3 5 minutes
- SC1: NH_4OH + H_2O_2 (1:1) 20 minutes at 80°C
- SC2: HCl + H_2O_2 (1:1) 20 minutes at 80°C

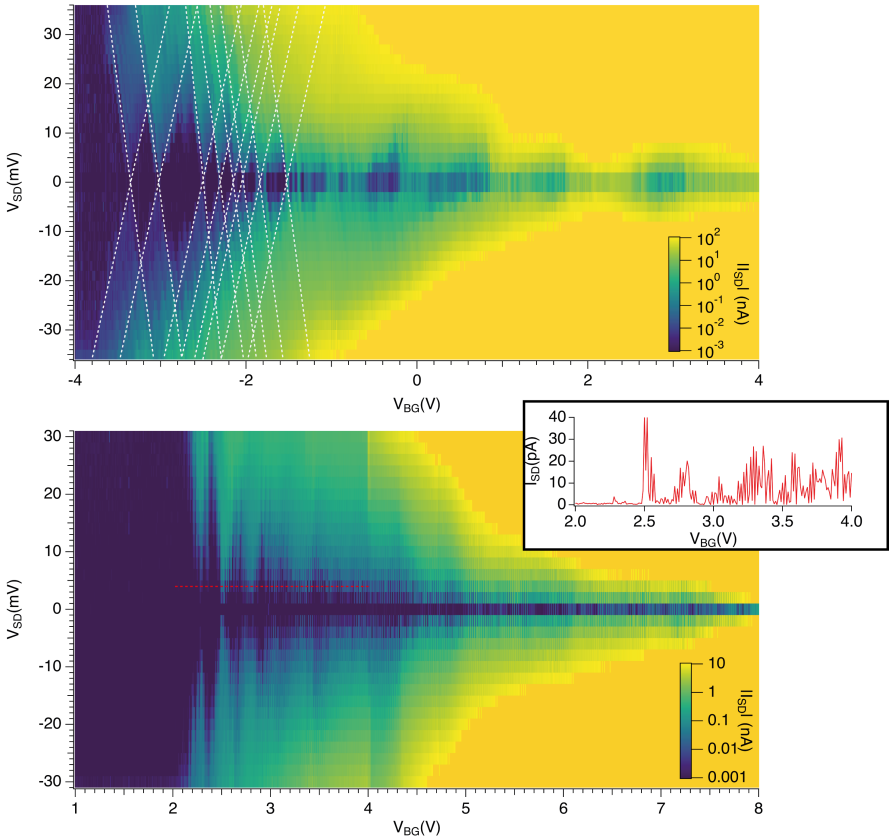

FIG. A.1: Current modulus map as a function of source-drain bias (V_{SD}) and backgate (V_{BG}). Results from two representative samples are shown. These samples belong to the same growth batch, but were contacted at different times and on different samples. In the top graph, white dashed lines show the edges of the coulomb blockade diamonds.In the bottom graph, the red dashed lines corresponds to the scan shown in the inset, which is shown here to highlight the presence of main current peaks, each modulated by finer oscillations.

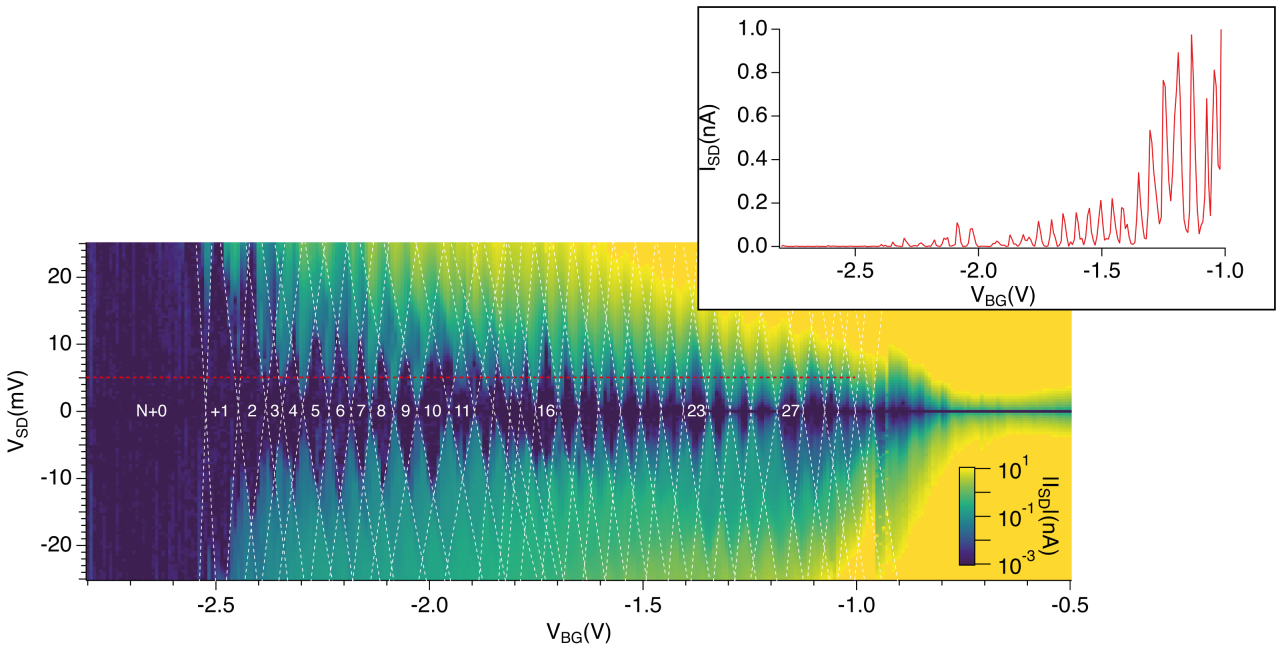

FIG. A.2: Current map for crystal phase quantum dot with high number of Coulomb blockade diamonds visible. The dashed lines mark diamonds' edges. The insert shows a cut of the current map along the red dotted line.

A.2 CRYSTAL PHASE QUANTUM DOTS

InAs nanowires grown at the NEST laboratory in Pisa were used to study the behaviour of nanowire devices. In this section the transport characterization of a growth batch with colloidal Au nano-particles size of 30 nm, nanowire diameter of 50-60 nm and length of $\sim$2.5 μm. Low temperature (2 K) transport measurements (Fig. A.1) revealed for all of the nanowires of this batch Quantum Dot like features, that were mapped by sweeping bias and backgate potentials to reveal Coulomb Blockade diamonds with energy level separation and charging in the range between 5 and 15 meV, as measured from the height of the diamonds. In one case a high quality QD was observed (Fig. A.2), with up to 30 diamonds clearly visible.

Since these nanowires are nominally pure InAs, the most likely explanation for the formation of a QD is the presence of stacking faults during the growth process. These planar defects lead to a change in the crystal phase, between wurtzite and zincblende structures. Because of the different band gap alignment [195] the different crystal structures provide a barrier of $\sim$100 meV [196, 197]. Control over the parameters during the growth process of the nanowires allows the choice of the crystal phase. This has been extensively used as a tool to define QD inside nanowires [190, 198, 199].

One of the most important steps in the fabrication process is the sulphur passivation [169]. In this process a solution is used to etch the nanowire surface oxide in the exposed area. If this step is properly

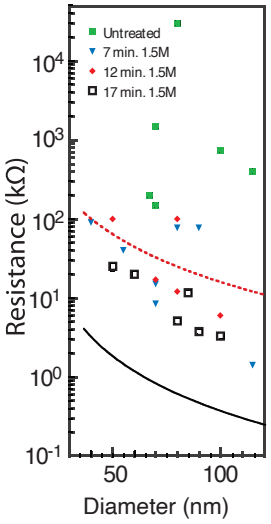

FIG. A.3: Room temperature resistance of InAs nanowires passivated with a $(NH_4)S_x$ solution like the one used in this work for different treatment times and nanowire diameter. The solid curve indicates the lowest theoretical limit of the resistance for fully ballistic transport in the nanowire, the dotted red line marks the transition between the ohmic (below it) and non ohmic regime. Taken from [169].

done an Ohmic contact is formed with the gold contacts that are thermally evaporated on the nanowire. If this process is not performed, or not performed properly, the surface oxide acts as a Schottky barrier. This has been exploited to obtain large quantum dots from the whole nanowire [200–202], with the size mostly determined by the distance between the source and drain contacts thanks to the screening effect they provide from the external gates. The formation of an ohmic contact is usually determined by two point resistance measurement at room temperature. Here the results of the measurements of two cases (Fig. A.1), one having a 25 $k\Omega$ resistance (top map) and one having a 230 $k\Omega$ resistance (bottom map). The higher resistance of the second case is already over the ohmic threshold (Fig. A.3). This is confirmed by the low temperature measurements, where an oscillating modulation of the main peaks is visible. A crystal phase QD, similar to the ones present in the other devices, provides the main confinement, with larger energy spacing and therefore smaller QD size. The additional modulation is due to a shallow confinement between the main QD and the Au leads. The close spacing of the energy levels, and possibly the broadening of the transitions due to the non-zero tunnelling rate, mean that these energy levels are never able to provide true Coulomb blockade and stop the sequential tunnelling in the main QD. The oscillations therefore emerge as the density of states of the secondary QD is probed by the shift induced by the backgate. In order to further confirm this hypothesis we estimate the charging energies for the main and secondary QDs in Fig A.1. The charging energy of the main QD is $\frac{e^2}{C} = 12 + 2$ meV, which is the same as similar devices, with QDs 20 nm long in nanowires of 50 nm radius. The charging energy of the secondary QD is ten times smaller $\sim$ 1 meV. This estimate is obtained trough the backgate's lever arm α =480 meV/V, calculated thanks to charging energy of the main QD. In a device like this, the backgate capacitance per unit length is given by [172]:

$$\frac{C}{L} = \frac{2\pi\epsilon_0\epsilon_r}{\cosh^{-1}(t/R)} \tag{A.1}$$

where ϵ_r is the dielectric constant of the dielectric substrate, t is the distance between the backgate and the center of the nanowire, R is the radius of the nanowire. Since all of these quantities are constant for the two QDs in the same nanowire, the ratio between the charging energies in inversely proportional to the lengths of the QDs. From this we obtain a back of the envelope estimate of the secondary QD's length of 200 nm, which is consistent with the nominal distance of the source and drain contacts (400 nm), considering that we are not able to observe the exact location of the main QD.

A.3 DOUBLE QUANTUM DOT

A.3.1 *Additional devices statistics and energetics*

In this chapter are reported the characterization of three total devices: one already presented in chapter 6 (called here sample 1) and two more. These devices were fabricated starting from two distinct growth batches. we briefly describe their control scheme, and report the results of their characterization. The heterostructures' sizes in the two batches are detailed in table A.1. The main difference between the two is the interdot barrier thickness: batch 2 has a significantly thicker barrier, which should decrease the wavefunction overlap in the two dots, reducing the tunnel coupling. Most of the results reported here were obtained from samples 1 and 3. In table A.2 we report the measured energetics for all four devices: the two batches have consistent energetics and are comparable with the results in the literature for these device[56].

	InP 1	InAs 1	InP 2	InAs 2	InP 3	Diameter	
Batch A	5	20	5	22.5	5	70	nm
Batch B	5.2	17.5	6.8	17.6	5.4	50	nm

TABLE A.1: DQD size features of the two batches studied in this work.

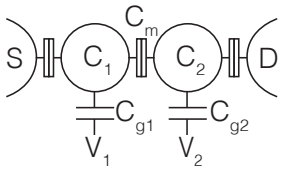

FIG. A.4: Classical capacitance model of a DQD

Device	Sample 1	Sample 2	Sample 3	Units
Batch	1	1	2	
Identifier	B1d2	C2d2	Jod5	
α_{G1}	20±3	17±3	70±10	meV/V
α_{G2}	18±3	14±2	17±2	meV/V
C_1	23±3	24±3	13±2	aF
C_2	22±3	15±2	28±3	aF
C_m	9±2	4.5±1	6±2	aF
E_{C1}	8.1±1	7.1±1.5	13±2	meV
E_{C2}	8.7±1.3	11±2	7±2	meV
E_{Cm}	3.3±0.2	2±0.3	3.3±1	meV
ΔE	15-20	>15	5	meV

TABLE A.2: Energetics of the three reported samples.

Here we comment briefly on the features observed in the figures A.6 and A.7. Some of the current triangles of sample 1 are not closed: two current lines extend away towards the right. This is likely due to an imperfect blocking from one of the external (meaning not inter-dots) barriers: some current flow is possible even if it should be

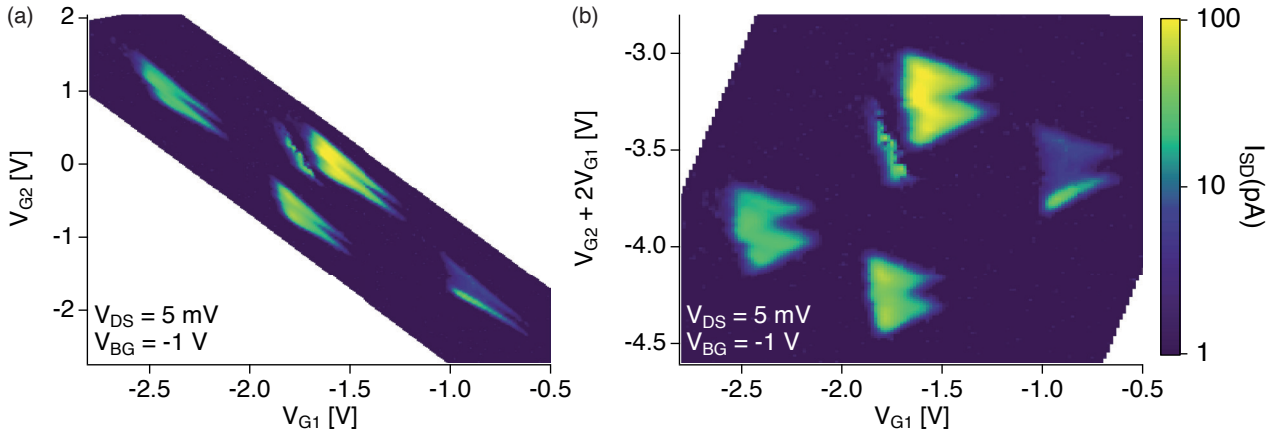

FIG. A.5: Comparison of the same current map as acquired as a function of (a) original V_{G1}, V_{G2} and (b) combined gate voltages V_{G1}, $V_{G2} + 2 \times V_{G2}$. The current triangles, characteristic of DQD transport, are much more distinguishable in the second approach. Results from sample 2.

prohibited by the gate configuration. This effect is energy level dependent: other triangles in the stability diagram are not affected. We understand this as being the result of different eigenstates having different wavefunctions and therefore different tunnelling probabilities. Another effect we notice on this device is the current modulation inside the QD itself, visible also in the next chapter, in figure 6.10. This is a characteristic often observed also in single QD devices. We understand this as a result of imperfect passivation and/or the presence of crystalline defects in the lead section of the nanowires. The resulting confinement leads to a QD like confinement, with an oscillating density of states. This is also affected by the external gates and modulates the tunnelling in the main DQD features.

A.3.2 *DQD control scheme*

Figure A.8(c) shows a SEM picture of the typical device geometry used for this experiment. Three gates are available to tune the device: a backgate V_{BG} and two sidegates V_{G1}, V_{G2}. They all concur to determine the electron filling in the device by shifting the addition energy. In addition to that, any asymmetry in the gate voltages will determine the presence of transverse fields that affect the electronic wave function. These wave functions are differently affected by the electric field, because of both the asymmetry in the QDs sizes and the intrinsic differences in their shapes, similarly to what happens for atomic orbitals. The squeezing of the orbital shapes will determine distinct evolution addition energies of the two QDs, allowing control over their configuration comparable to having two distinct electrodes controlling each QD[56]. In first approximation we could consider the QDs filling and detuning to be controlled by the gate voltages average and difference respectively. In practice this is rarely the case:

asymmetries between the gates and the indirect detuning mechanism are such that the most efficient gate combination must be experimentally determined for each device. This is done to avoid mapping extensively gate configurations where no signal can be observed, and to highlight the transport features. A comparison of a current map as acquired and using a gate combination is shown in figure A.5. In order to simplify operation of finding an appropriate gate combination, two "geometrical" transformations were used: rotation and shear. They are described by the following matrix operations:

$$R(\theta): \quad \begin{bmatrix} x' \\ y' \end{bmatrix} = \begin{bmatrix} \cos\theta & -\sin\theta \\ \sin\theta & \cos\theta \end{bmatrix} \begin{bmatrix} x \\ y \end{bmatrix} \tag{A.2}$$

$$S_x(\lambda): \quad \begin{bmatrix} x' \\ y' \end{bmatrix} = \begin{bmatrix} 1 & \lambda \\ 0 & 1 \end{bmatrix} \begin{bmatrix} x \\ y \end{bmatrix} \tag{A.3}$$

$$S_y(\xi): \quad \begin{bmatrix} x' \\ y' \end{bmatrix} = \begin{bmatrix} 1 & 0 \\ \xi & 1 \end{bmatrix} \begin{bmatrix} x \\ y \end{bmatrix} \tag{A.4}$$

Where $R(\theta)$ represents a rotation by an angle θ, and S_x, S_y represent a shear parallel to the x and y axis respectively. (x, y) and (x', y') are the original and transformed set of coordinates. The translation between the combined set and the actually applied voltages is all handled by the software I wrote, simply reversing the previous transformations. The transformation is therefore reversible and can be identified simply by the three parameters θ, λ, ξ. As previously stated, in most of the tested DQD devices two sidegates and one backgate are available. If one of them is disconnected, two are still sufficient to characterize the devices. If only one works, it is not possible to tune the transverse field independently. When all three gates work, one of them is fixed in order to reduce the parameter space. The approach typically used is the following: all gates are driven in parallel with a finite bias applied ($V_{DS} = 1 - 15$ mV) performing a scan. The lowest visible current peak is chosen as the fixed value for the backgate voltage V_{BG}, after that the two sidegates are driven independently to map the device. The employed gate combinations in the reported devices are:

	Sample 1	Sample 2	Sample 3
$V'_{G1} =$	$\frac{1}{\sqrt{2}}(V_{G2} - V_{G1})$	V_{G1}	$0.21 \times V_{G1} - 0.98 \times V_{G2}$
$V'_{G2} =$	$\frac{1}{\sqrt{2}}(V_{G1} + V_{G2})$	$V_{G2} + 2V_{G1}$	$0.98 \times V_{G1} + 0.21 \times V_{G2}$

Microwave feeding to the device is done by connecting one of the available coaxial lines (see chapter 3) to a bonding pad on the chip, but not directly to one of the device electrodes.

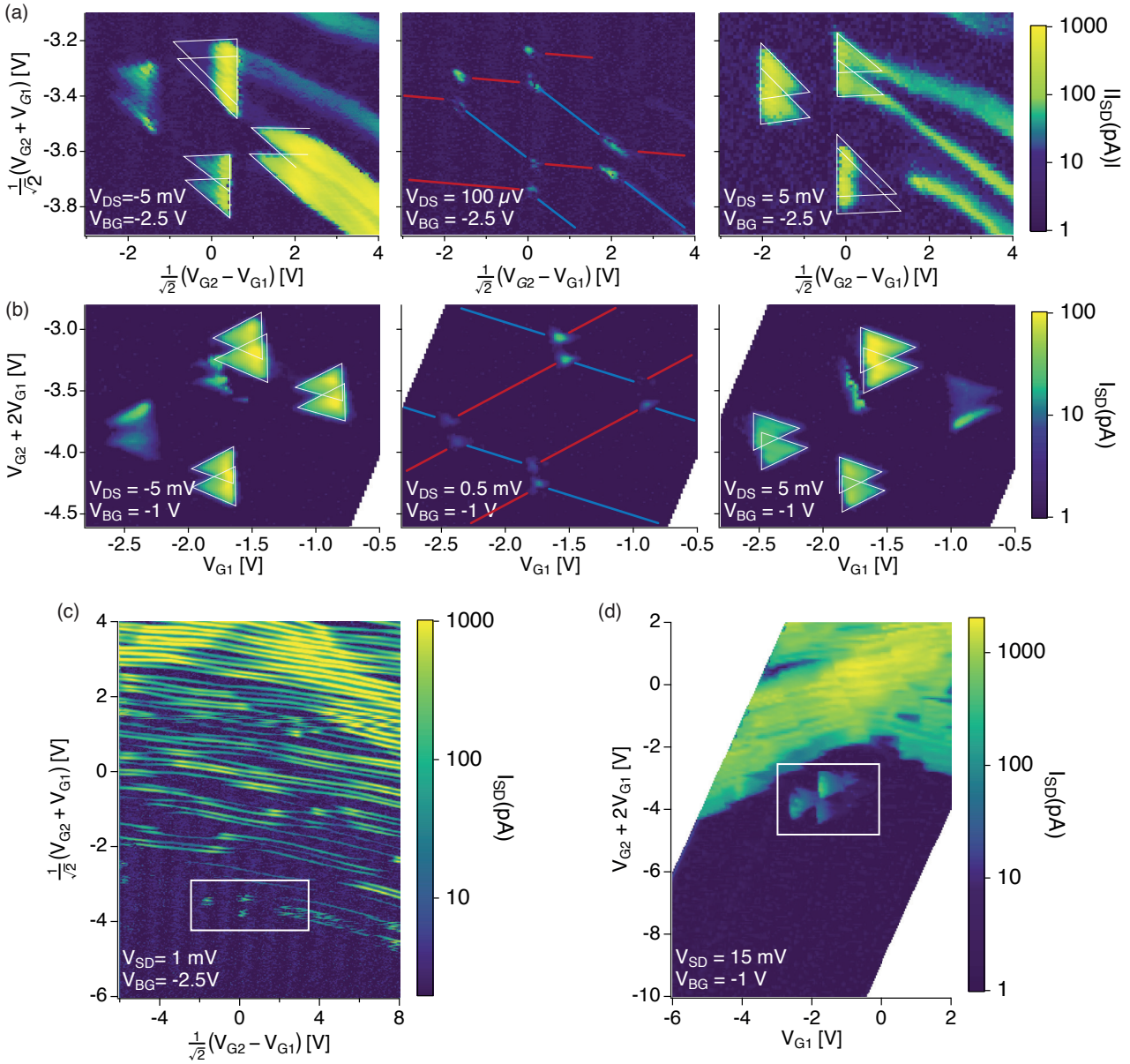

FIG. A.6: (a) Bias series of sample 1. (b) Bias series of sample 2. (c,d) Survey of sample 1 and 2 respectively, with the white square marking the range in which the bias series were taken.

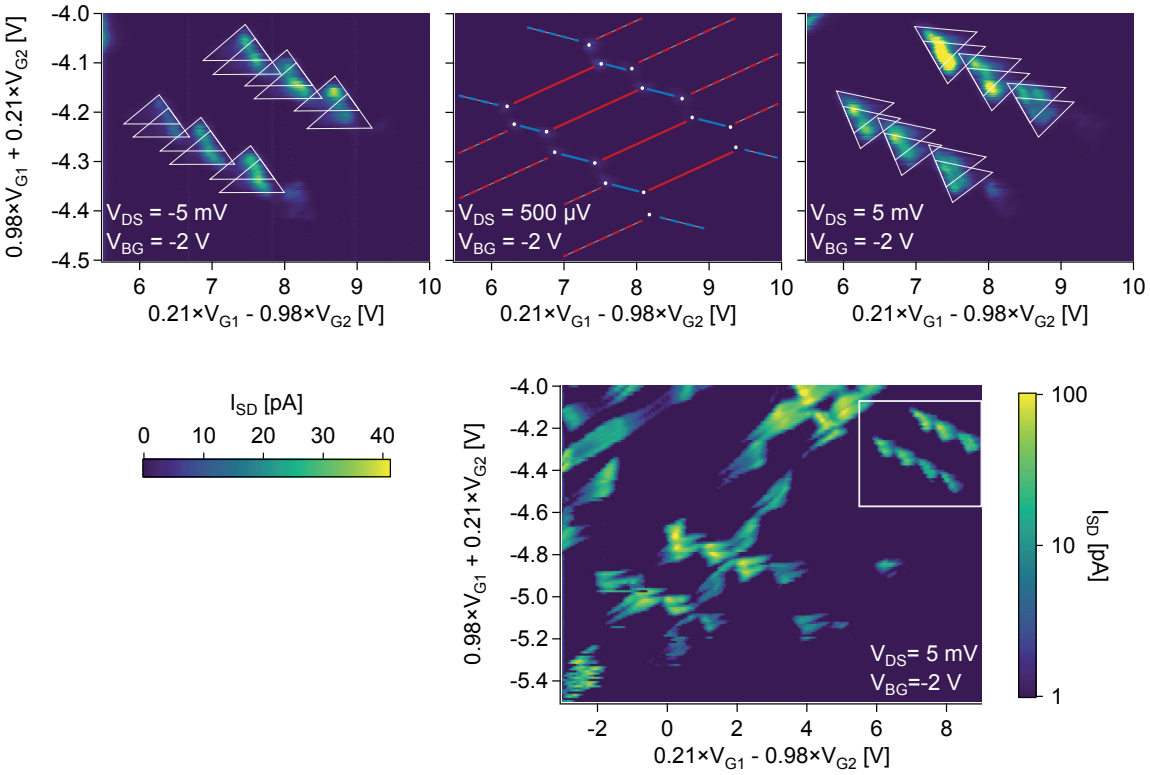

FIG. A.7: Bias series of sample 3, bottom right graph shows a wider survey of said sample.

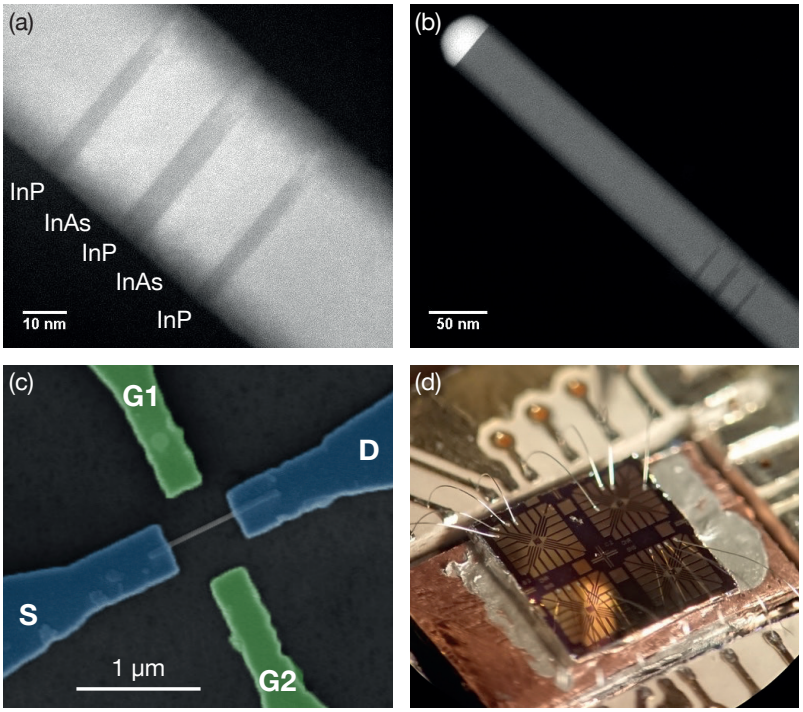

FIG. A.8: (a) TEM image of a DQD defined by alternating layers of InAs/InP along an InAs nanowire. (b) Wider view of the same nanowire. (c) Example of one of the characterized device, composed of source (S), drain (D) and gate (G1,G2) electrodes. A backgate electrode, not shown here, was also used to control the devices. (d) picture of one of the measured devices as bonded on the sample-holder.

BIBLIOGRAPHY

[1] K. Grainge et al. "Square Kilometre Array: The Radio Telescope of the XXI Century." In: *Astronomy Reports* 61.4 (Apr. 2017), pp. 288–296. ISSN: 1562-6881. DOI: 10.1134/S1063772917040059.

[2] Xiu Gu, Anton Frisk Kockum, Adam Miranowicz, Yu-xi Liu, and Franco Nori. "Microwave Photonics with Superconducting Quantum Circuits." In: *Physics Reports* 718–719 (Nov. 2017), pp. 1–102. ISSN: 03701573. DOI: 10.1016/j.physrep.2017.10.002.

[3] Samuele Cornia, Francesco Rossella, Valeria Demontis, Valentina Zannier, Fabio Beltram, Lucia Sorba, Marco Affronte, and Alberto Ghirri. "Microwave-Assisted Tunneling in Hard-Wall InAs/InP Nanowire Quantum Dots." In: *Scientific Reports* 9.1 (Dec. 2019), p. 19523. ISSN: 2045-2322. DOI: 10.1038/s41598-019-56053-2.

[4] S. K. Lamoreaux, K. A. van Bibber, K. W. Lehnert, and G. Carosi. "Analysis of Single-Photon and Linear Amplifier Detectors for Microwave Cavity Dark Matter Axion Searches." In: *Physical Review D* 88.3 (Aug. 2013), p. 035020. DOI: 10.1103/PhysRevD.88.035020.

[5] B. M. Brubaker et al. "First Results from a Microwave Cavity Axion Search at $24\text{ }\text{ }\ensuremath{\mu}\mathrm{eV}$." In: *Physical Review Letters* 118.6 (Feb. 2017), p. 061302. DOI: 10.1103/PhysRevLett.118.061302.

[6] ADMX Collaboration et al. "Search for Invisible Axion Dark Matter with the Axion Dark Matter Experiment." In: *Physical Review Letters* 120.15 (Apr. 2018), p. 151301. DOI: 10.1103/PhysRevLett.120.151301.

[7] L. Zhong et al. "Results from Phase 1 of the HAYSTAC Microwave Cavity Axion Experiment." In: *Physical Review D* 97.9 (May 2018), p. 092001. DOI: 10.1103/PhysRevD.97.092001.

[8] M. D. Eisaman, J. Fan, A. Migdall, and S. V. Polyakov. "Invited Review Article: Single-photon Sources and Detectors." In: *Review of Scientific Instruments* 82.7 (July 2011), p. 071101. ISSN: 0034-6748. DOI: 10.1063/1.3610677.

[9] D. I. Schuster et al. "Resolving Photon Number States in a Superconducting Circuit." In: *Nature* 445.7127 (Feb. 2007), pp. 515–518. ISSN: 1476-4687. DOI: 10.1038/nature05461.

[10] B. R. Johnson et al. "Quantum Non-Demolition Detection of Single Microwave Photons in a Circuit." In: *Nature Physics* 6.9 (Sept. 2010), pp. 663–667. ISSN: 1745-2481. DOI: 10.1038/nphys1710.

[11] Y.-F. Chen, D. Hover, S. Sendelbach, L. Maurer, S. T. Merkel, E. J. Pritchett, F. K. Wilhelm, and R. McDermott. "Microwave Photon Counter Based on Josephson Junctions." In: *Physical Review Letters* 107.21 (Nov. 2011), p. 217401. DOI: 10.1103/PhysRevLett.107.217401.

[12] C. Eichler, C. Lang, J. M. Fink, J. Govenius, S. Filipp, and A. Wallraff. "Observation of Entanglement between Itinerant Microwave Photons and a Superconducting Qubit." In: *Physical Review Letters* 109.24 (Dec. 2012), p. 240501. DOI: 10.1103/PhysRevLett.109.240501.

[13] Kunihiro Inomata, Zhirong Lin, Kazuki Koshino, William D. Oliver, Jaw-Shen Tsai, Tsuyoshi Yamamoto, and Yasunobu Nakamura. "Single Microwave-Photon Detector Using an Artificial Λ-type Three-Level System." In: *Nature Communications* 7.1 (July 2016), p. 12303. ISSN: 2041-1723. DOI: 10.1038/ncomms12303.

[14] A. Narla et al. "Robust Concurrent Remote Entanglement Between Two Superconducting Qubits." In: *Physical Review X* 6.3 (Sept. 2016), p. 031036. DOI: 10.1103/PhysRevX.6.031036.

[15] S. Kono, K. Koshino, Y. Tabuchi, A. Noguchi, and Y. Nakamura. "Quantum Non-Demolition Detection of an Itinerant Microwave Photon." In: *Nature Physics* 14.6 (June 2018), pp. 546–549. ISSN: 1745-2481. DOI: 10.1038/s41567-018-0066-3.

[16] Jean-Claude Besse, Simone Gasparinetti, Michele C. Collodo, Theo Walter, Philipp Kurpiers, Marek Pechal, Christopher Eichler, and Andreas Wallraff. "Single-Shot Quantum Nondemolition Detection of Individual Itinerant Microwave Photons." In: *Physical Review X* 8.2 (Apr. 2018), p. 021003. ISSN: 2160-3308. DOI: 10.1103/PhysRevX.8.021003.

[17] Fernando Patolsky and Charles M. Lieber. "Nanowire Nanosensors." In: *Materials Today* 8.4 (Apr. 2005), pp. 20–28. ISSN: 1369-7021. DOI: 10.1016/S1369-7021(05)00791-1.

[18] Mahdi Asgari, Leonardo Viti, Valentina Zannier, Lucia Sorba, and Miriam Serena Vitiello. "Semiconductor Nanowire Field-Effect Transistors as Sensitive Detectors in the Far-Infrared." In: *Nanomaterials* 11.12 (Dec. 2021), p. 3378. ISSN: 2079-4991. DOI: 10.3390/nano11123378.

[19] Kun Peng and Michael B. Johnston. "The Application of One-Dimensional Nanostructures in Terahertz Frequency Devices." In: *Applied Physics Reviews* 8.4 (Nov. 2021), p. 041314. DOI: 10.1063/5.0060797.

[20] Ali Emre Kaplan, Valerio Vitali, Valeria Demontis, Francesco Rossella, Andrea Fontana, Samuele Cornia, Periklis Petropoulos, Vittorio Bellani, Cosimo Lacava, and Ilaria Cristiani. "Polarization Control in Integrated Silicon Waveguides Using Semiconductor Nanowires." In: (2022), p. 11.

[21] Ch. Blömers, T. Grap, M. I. Lepsa, J. Moers, St. Trellenkamp, D. Grützmacher, H. Lüth, and Th. Schäpers. "Hall Effect Measurements on InAs Nanowires." In: *Applied Physics Letters* 101.15 (Oct. 2012), p. 152106. ISSN: 0003-6951, 1077-3118. DOI: 10.1063/1.4759124.

[22] Steven Chuang, Qun Gao, Rehan Kapadia, Alexandra C. Ford, Jing Guo, and Ali Javey. "Ballistic InAs Nanowire Transistors." In: *Nano Letters* 13.2 (Feb. 2013), pp. 555–558. ISSN: 1530-6984, 1530-6992. DOI: 10.1021/nl3040674.

[23] J. Gooth, V. Schaller, S. Wirths, H. Schmid, M. Borg, N. Bologna, S. Karg, and H. Riel. "Ballistic One-Dimensional Transport in InAs Nanowires Monolithically Integrated on Silicon." In: *Applied Physics Letters* 110.8 (Feb. 2017), p. 083105. ISSN: 0003-6951, 1077-3118. DOI: 10.1063/1.4977031.

[24] S. Estévez Hernández, M. Akabori, K. Sladek, Ch. Volk, S. Alagha, H. Hardtdegen, M. G. Pala, N. Demarina, D. Grützmacher, and Th. Schäpers. "Spin-Orbit Coupling and Phase Coherence in InAs Nanowires." In: *Physical Review B* 82.23 (Dec. 2010), p. 235303. ISSN: 1098-0121, 1550-235X. DOI: 10.1103/PhysRevB.82.235303.

[25] Sven Dorsch, In-Pyo Yeo, Sebastian Lehmann, Kimberly Dick, Claes Thelander, and Adam Burke. "Gate Control, g-Factors and Spin Orbit Energy of p-Type GaSb Nanowire Quantum Dot Devices." In: *Physical Review B* 103.24 (June 2021), p. L241411. ISSN: 2469-9950, 2469-9969. DOI: 10.1103/PhysRevB.103.L241411. arXiv: 2103.15700.

[26] Zoltán Scherübl, Gergő Fülöp, Morten H. Madsen, Jesper Nygård, and Szabolcs Csonka. "Electrical Tuning of Rashba Spin-Orbit Interaction in Multigated InAs Nanowires." In: *Physical Review B* 94.3 (July 2016), p. 035444. ISSN: 2469-9950, 2469-9969. DOI: 10.1103/PhysRevB.94.035444.

[27] Paweł Wójcik, Andrea Bertoni, and Guido Goldoni. "Enhanced Rashba Spin-Orbit Coupling in Core-Shell Nanowires by the Interfacial Effect." In: *Applied Physics Letters* 114.7 (Feb. 2019), p. 073102. ISSN: 0003-6951, 1077-3118. DOI: 10.1063/1.5082602.

[28] A. Iorio, M. Rocci, L. Bours, M. Carrega, V. Zannier, L. Sorba, S. Roddaro, F. Giazotto, and E. Strambini. "Vectorial Control of the Spin–Orbit Interaction in Suspended InAs Nanowires." In: *Nano Letters* 19.2 (Feb. 2019), pp. 652–657. ISSN: 1530-6984, 1530-6992. DOI: 10.1021/acs.nanolett.8b02828.

[29] J Salfi, S Roddaro, D Ercolani, L Sorba, I Savelyev, M Blumin, H E Ruda, and F Beltram. "Electronic Properties of Quantum Dot Systems Realized in Semiconductor Nanowires." In: *Semiconductor Science and Technology* 25.2 (Feb. 2010), p. 024007. ISSN: 0268-1242, 1361-6641. DOI: 10.1088/0268-1242/25/2/024007.

[30] P. L. Richards. "Bolometers for Infrared and Millimeter Waves." In: *Journal of Applied Physics* 76.1 (July 1994), pp. 1–24. ISSN: 0021-8979, 1089-7550. DOI: 10.1063/1.357128.

[31] Roope Kokkoniemi et al. "Nanobolometer with Ultralow Noise Equivalent Power." In: *Communications Physics* 2.1 (Dec. 2019), p. 124. ISSN: 2399-3650. DOI: 10.1038/s42005-019-0225-6.

[32] D. Gray, C. Enss, A. Fleischmann, L. Gastaldo, C. Hassel, D. Hengstler, S. Kempf, M. Loidl, X. F. Navick, and M. Rodrigues. "The First Tests of a Large-Area Light Detector Equipped with Metallic Magnetic Calorimeters for Scintillating Bolometers for the LUMINEU Neutrinoless Double Beta Decay Search." In: *Journal of Low Temperature Physics* 184.3 (Aug. 2016), pp. 904–909. ISSN: 1573-7357. DOI: 10.1007/s10909-016-1535-7.

[33] Stefano Roddaro, Daniele Ercolani, Mian Akif Safeen, Soile Suomalainen, Francesco Rossella, Francesco Giazotto, Lucia Sorba, and Fabio Beltram. "Giant Thermovoltage in Single InAs Nanowire Field-Effect Transistors." In: *Nano Lett.* (2013), p. 5.

[34] Mirko Rocci, Valeria Demontis, Domenic Prete, Daniele Ercolani, Lucia Sorba, Fabio Beltram, Giovanni Pennelli, Stefano Roddaro, and Francesco Rossella. "Suspended InAs Nanowire-Based Devices for Thermal Conductivity Measurement Using the 3ω Method." In: *Journal of Materials Engineering and Performance* 27.12 (Dec. 2018), pp. 6299–6305. ISSN: 1059-9495, 1544-1024. DOI: 10.1007/s11665-018-3715-x.

[35] Domenic Prete, Paolo Andrea Erdman, Valeria Demontis, Valentina Zannier, Daniele Ercolani, Lucia Sorba, Fabio Beltram, Francesco Rossella, Fabio Taddei, and Stefano Roddaro. "Thermoelectric Conversion at 30 K in InAs/InP Nanowire Quantum Dots." In: *Nano Letters* 19.5 (May 2019), pp. 3033–3039. ISSN: 1530-6984, 1530-6992. DOI: 10.1021/acs.nanolett.9b00276.

[36] Sven Dorsch, Artis Svilans, Martin Josefsson, Bahareh Goldozian, Mukesh Kumar, Claes Thelander, Andreas Wacker, and Adam Burke. "Heat Driven Transport in Serial Double Quantum Dot Devices." In: *Nano Letters* 21.2 (Jan. 2021), pp. 988–994. ISSN: 1530-6984, 1530-6992. DOI: 10.1021/acs.nanolett.0c04017.

[37] Mahdi Asgari, Dominique Coquillat, Guido Menichetti, Valentina Zannier, Nina Diakonova, Wojciech Knap, Lucia Sorba, Leonardo Viti, and Miriam Serena Vitiello. "Quantum-Dot Single-Electron Transistors as Thermoelectric Quantum Detectors at Terahertz Frequencies." In: *Nano Letters* 21.20 (Oct. 2021), pp. 8587–8594. ISSN: 1530-6984, 1530-6992. DOI: 10.1021/acs.nanolett.1c02022.

[38] Seongjae Cho, Kyung Rok Kim, Byung-Gook Park, and In Man Kang. "RF Performance and Small-Signal Parameter Extraction of Junctionless Silicon Nanowire MOSFETs." In: *IEEE Transactions on Electron Devices* 58.5 (May 2011), pp. 1388–1396. ISSN: 1557-9646. DOI: 10.1109/TED.2011.2109724.

[39] Zhen Zhan, Enrique Colomés, and Xavier Oriols. "Limitations of the Intrinsic Cut-off Frequency to Correctly Quantify the Speed of Nanoscale Transistors." In: *IEEE Transactions on Electron Devices* 64.6 (June 2017), pp. 2617–2624. ISSN: 0018-9383, 1557-9646. DOI: 10.1109/TED.2017.2691400. arXiv: 1611.03856.

[40] Michael Dyakonov and Michael Shur. "Shallow Water Analogy for a Ballistic Field Effect Transistor: New Mechanism of Plasma Wave Generation by Dc Current." In: *Physical Review Letters* 71.15 (Oct. 1993), pp. 2465–2468. ISSN: 0031-9007. DOI: 10.1103/PhysRevLett.71.2465.

[41] Michael S Shur and Victor Ryzhii. "Plasma Wave Electronics." In: 13ù.2 (2003), pp. 575–600.

[42] Leonardo Viti, Dominique Coquillat, Daniele Ercolani, Lucia Sorba, and Miriam S Vitiello. "Nanowire Terahertz Detectors with a Resonant Four-Leaf-Clover-Shaped Antenna." In: (2014), p. 8.

[43] R. Weikle, J.-Q. Lü, M.S. Shur, and M.I. Dyakonov. "Detection of Microwave Radiation by Electronic Fluid in High Electron Mobility Transistors." In: *Electronics Letters* 32.23 (1996), p. 2148. ISSN: 00135194. DOI: 10.1049/el:19961410.

[44] Wojciech Knap et al. "Field Effect Transistors for Terahertz Detection: Physics and First Imaging Applications." In: *Journal of Infrared, Millimeter, and Terahertz Waves* (Aug. 2009). ISSN: 1866-6892, 1866-6906. DOI: 10.1007/s10762-009-9564-9.

[45] M. Dyakonov and M. Shur. "Detection, Mixing, and Frequency Multiplication of Terahertz Radiation by Two-Dimensional Electronic Fluid." In: *IEEE Transactions on Electron Devices* 43.3 (Mar. 1996), pp. 380–387. ISSN: 1557-9646. DOI: 10.1109/16.485650.

[46] S. Tarucha, D. G. Austing, T. Honda, R. J. van der Hage, and L. P. Kouwenhoven. "Shell Filling and Spin Effects in a Few Electron Quantum Dot." In: *Physical Review Letters* 77.17 (Oct. 1996), pp. 3613–3616. ISSN: 0031-9007, 1079-7114. DOI: 10.1103/PhysRevLett.77.3613.

[47] L. P. Kouwenhoven, T. H. Oosterkamp, M. W. S. Danoesastro, M. Eto, D. G. Austing, T. Honda, and S. Tarucha. "Excitation Spectra of Circular, Few-Electron Quantum Dots." In: *Science (New York, N.Y.)* 278.5344 (1997), pp. 1788–1792. ISSN: 0036-8075. DOI: 10.1126/science.278.5344.1788. eprint: https://science.sciencemag.org/content/278/5344/1788.full.pdf.

[48] Mikael T. Björk, Claes Thelander, Adam E. Hansen, Linus E. Jensen, Magnus W. Larsson, L. Reine Wallenberg, and Lars Samuelson. "Few-Electron Quantum Dots in Nanowires." In: *Nano Letters* 4.9 (Sept. 2004), pp. 1621–1625. ISSN: 1530-6984, 1530-6992. DOI: 10.1021/nl049230s.

[49] C. W. J. Beenakker. "Theory of Coulomb-blockade Oscillations in the Conductance of a Quantum Dot." In: *Physical Review B* 44.4 (July 1991), pp. 1646–1656. ISSN: 0163-1829, 1095-3795. DOI: 10.1103/PhysRevB.44.1646.

[50] R. Hanson, L. P. Kouwenhoven, J. R. Petta, S. Tarucha, and L. M. K. Vandersypen. "Spins in Few-Electron Quantum Dots." In: *Reviews of Modern Physics* 79.4 (Oct. 2007), pp. 1217–1265. ISSN: 0034-6861, 1539-0756. DOI: 10.1103/RevModPhys.79.1217.

[51] Lorenzo Romeo, Stefano Roddaro, Alessandro Pitanti, Daniele Ercolani, Lucia Sorba, and Fabio Beltram. "Electrostatic Spin Control in InAs/InP Nanowire Quantum Dots." In: *Nano Letters* 12.9 (Sept. 2012), pp. 4490–4494. ISSN: 1530-6984, 1530-6992. DOI: 10.1021/nl301497j.

[52] Zahra Sadre Momtaz, Stefano Servino, Valeria Demontis, Valentina Zannier, Daniele Ercolani, Francesca Rossi, Francesco Rossella, Lucia Sorba, Fabio Beltram, and Stefano Roddaro. "Orbital Tuning of Tunnel Coupling in InAs/InP Nanowire Quantum Dots." In: *Nano Letters* 20.3 (Mar. 2020), pp. 1693–1699. ISSN: 1530-6984, 1530-6992. DOI: 10.1021/acs.nanolett.9b04850. arXiv: 1911.10264.

[53] Stefano Roddaro, Andrea Pescaglini, Daniele Ercolani, Lucia Sorba, and Fabio Beltram. "Manipulation of Electron Orbitals in Hard-Wall InAs/InP Nanowire Quantum Dots." In: *Nano Letters* 11.4 (Apr. 2011), pp. 1695–1699. ISSN: 1530-6984, 1530-6992. DOI: 10.1021/nl200209m.

[54] C. Fasth, A. Fuhrer, L. Samuelson, Vitaly N. Golovach, and Daniel Loss. "Direct Measurement of the Spin-Orbit Interaction in a Two-Electron InAs Nanowire Quantum Dot." In: *Physical Review Letters* 98.26 (June 2007), p. 266801. ISSN: 0031-9007, 1079-7114. DOI: 10.1103/PhysRevLett.98.266801.

[55] Andreas Fuhrer, Linus E. Fröberg, Jonas Nyvold Pedersen, Magnus W. Larsson, Andreas Wacker, Mats-Erik Pistol, and Lars Samuelson. "Few Electron Double Quantum Dots in InAs/InP Nanowire Heterostructures." In: *Nano Letters* 7.2 (Feb. 2007), pp. 243–246. ISSN: 1530-6984, 1530-6992. DOI: 10.1021/nl061913f.

[56] Francesco Rossella, Andrea Bertoni, Daniele Ercolani, Massimo Rontani, Lucia Sorba, Fabio Beltram, and Stefano Roddaro. "Nanoscale Spin Rectifiers Controlled by the Stark Effect." In: *Nature Nanotechnology* 9.12 (Dec. 2014), pp. 997–1001. ISSN: 1748-3387, 1748-3395. DOI: 10.1038/nnano.2014.251.

[57] Mircea Trif, Vitaly N. Golovach, and Daniel Loss. "Spin Dynamics in InAs Nanowire Quantum Dots Coupled to a Transmission Line." In: *Physical Review B* 77.4 (Jan. 2008), p. 045434. ISSN: 1098-0121, 1550-235X. DOI: 10.1103/PhysRevB.77.045434.

[58] S. Nadj-Perge, S. M. Frolov, E. P. A. M. Bakkers, and L. P. Kouwenhoven. "Spin–Orbit Qubit in a Semiconductor Nanowire." In: *Nature* 468.7327 (Dec. 2010), pp. 1084–1087. ISSN: 0028-0836, 1476-4687. DOI: 10.1038/nature09682.

[59] David D. Awschalom, Lee C. Bassett, Andrew S. Dzurak, Evelyn L. Hu, and Jason R. Petta. "Quantum Spintronics: Engineering and Manipulating Atom-Like Spins in Semiconductors." In: *Science* 339.6124 (Mar. 2013), pp. 1174–1179. ISSN: 0036-8075, 1095-9203. DOI: 10.1126/science.1231364.

[60] X. Mi, J. V. Cady, D. M. Zajac, P. W. Deelman, and J. R. Petta. "Strong Coupling of a Single Electron in Silicon to a Microwave Photon." In: *Science* 355.6321 (Jan. 2017), p. 156. DOI: 10.1126/science.aal2469.

[61] A. Stockklauser, P. Scarlino, J. V. Koski, S. Gasparinetti, C. K. Andersen, C. Reichl, W. Wegscheider, T. Ihn, K. Ensslin, and A. Wallraff. "Strong Coupling Cavity QED with Gate-Defined Double Quantum Dots Enabled by a High Impedance Resonator." In: *Physical Review X* 7.1 (Mar. 2017), p. 011030. ISSN: 2160-3308. DOI: 10.1103/PhysRevX.7.011030.

[62] N. Samkharadze, G. Zheng, N. Kalhor, D. Brousse, A. Sammak, U. C. Mendes, A. Blais, G. Scappucci, and L. M. K. Vandersypen. "Strong Spin-Photon Coupling in Silicon." In: *Science* 359.6380 (Mar. 2018), pp. 1123–1127. ISSN: 0036-8075, 1095-9203. DOI: 10.1126/science.aar4054.

[63] X. Mi, M. Benito, S. Putz, D. M. Zajac, J. M. Taylor, Guido Burkard, and J. R. Petta. "A Coherent Spin–Photon Interface in Silicon." In: *Nature* 555.7698 (Mar. 2018), pp. 599–603. ISSN: 0028-0836, 1476-4687. DOI: 10.1038/nature25769.

[64] Takashi Nakajima et al. "Quantum Non-Demolition Measurement of an Electron Spin Qubit." In: *Nature Nanotechnology* 14.6 (June 2019), pp. 555–560. ISSN: 1748-3387, 1748-3395. DOI: 10.1038/s41565-019-0426-x.

[65] Neill Lambert, Franco Nori, and Christian Flindt. "Bistable Photon Emission from a Solid-State Single-Atom Laser." In: *Physical Review Letters* 115.21 (Nov. 2015), p. 216803. ISSN: 0031-9007, 1079-7114. DOI: 10.1103/PhysRevLett.115.216803.

[66] Y.-Y. Liu, J. Stehlik, C. Eichler, X. Mi, T. R. Hartke, M. J. Gullans, J. M. Taylor, and J. R. Petta. "Threshold Dynamics of a Semiconductor Single Atom Maser." In: *Physical Review Letters* 119.9 (Aug. 2017), p. 097702. ISSN: 0031-9007, 1079-7114. DOI: 10.1103/PhysRevLett.119.097702.

[67] Mattia Mantovani, Andrew D. Armour, Wolfgang Belzig, and Gianluca Rastelli. "Dynamical Multistability in a Quantum-Dot Laser." In: *Physical Review B* 99.4 (Jan. 2019), p. 045442. ISSN: 2469-9950, 2469-9969. DOI: 10.1103/PhysRevB.99.045442. arXiv: 1808.04884.

[68] Clement H. Wong and Maxim G. Vavilov. "Quantum Efficiency of a Single Microwave Photon Detector Based on a Semiconductor Double Quantum Dot." In: *Physical Review A* 95.1 (Jan. 2017), p. 012325. ISSN: 2469-9926, 2469-9934. DOI: 10.1103/PhysRevA.95.012325.

[69] Stefano Barbieri, Francesco Mango, Fabio Beltram, Marco Lazzarino, and Lucia Sorba. "Hot-electron Multiquantum Well Microwave Detector Operating at Room Temperature." In: *Applied Physics Letters* 67.2 (July 1995), pp. 250–252. ISSN: 0003-6951, 1077-3118. DOI: 10.1063/1.114683.

[70] P L McEuen, L P Kouwenhoven, S Jauhar, J Orenstein, K McCormick, D Dixon, Yu V Nazarov, N C van der Vaart, and C T Foxon. "Microwave-Assisted Transport through a Quantum Dot." In: *Nanotechnology* 7.4 (Dec. 1996), pp. 406–408. ISSN: 0957-4484, 1361-6528. DOI: 10.1088/0957-4484/7/4/018.

[71] W. G. van der Wiel, T. H. Oosterkamp, S. de Franceschi, C. J. P. M. Harmans, and L. P. Kouwenhoven. "Photon Assisted Tunneling in Quantum Dots." In: *Strongly Correlated Fermions and Bosons in Low-Dimensional Disordered Systems*. Ed. by I. V. Lerner, B. L. Althsuler, V. I. Fal'ko, and T. Giamarchi. Dordrecht: Springer Netherlands, 2002, pp. 43–68. ISBN: 978-94-010-0530-2. DOI: 10.1007/978-94-010-0530-2{_}3.

[72] T. Frey, P. J. Leek, M. Beck, J. Faist, A. Wallraff, K. Ensslin, T. Ihn, and M. Büttiker. "Quantum Dot Admittance Probed at Microwave Frequencies with an On-Chip Resonator." In: *Physical Review B* 86.11 (Sept. 2012), p. 115303. ISSN: 1098-0121, 1550-235X. DOI: 10.1103/PhysRevB.86.115303.

[73] K. Ishibashi and Y. Aoyagi. "Interaction of Electromagnetic Wave with Quantum Dots." In: *Physica B: Condensed Matter* 314.1-4 (Mar. 2002), pp. 437–443. ISSN: 09214526. DOI: 10.1016/S0921-4526(01)01441-7.

[74] M.R. Delbecq, L.E. Bruhat, J.J. Viennot, S. Datta, A. Cottet, and T. Kontos. "Photon-Mediated Interaction between Distant Quantum Dot Circuits." In: *Nature Communications* 4.1 (June 2013), p. 1400. ISSN: 2041-1723. DOI: 10.1038/ncomms2407.

[75] P. K. Tien and J. P. Gordon. "Multiphoton Process Observed in the Interaction of Microwave Fields with the Tunneling between Superconductor Films." In: *Physical Review* 129.2 (Jan. 1963), pp. 647–651. ISSN: 0031-899X. DOI: 10.1103/PhysRev.129.647.

[76] L. P. Kouwenhoven, S. Jauhar, K. McCormick, D. Dixon, P. L. McEuen, Yu. V. Nazarov, N. C. van der Vaart, and C. T. Foxon. "Photon-Assisted Tunneling through a Quantum Dot." In: *Physical Review B* 50.3 (July 1994), pp. 2019–2022. ISSN: 0163-1829, 1095-3795. DOI: 10.1103/PhysRevB.50.2019.

[77] W. G. van der Wiel, S. De Franceschi, J. M. Elzerman, T. Fujisawa, S. Tarucha, and L. P. Kouwenhoven. "Electron Transport through Double Quantum Dots." In: *Reviews of Modern Physics* 75.1 (Dec. 2002), pp. 1–22. ISSN: 0034-6861, 1539-0756. DOI: 10.1103/RevModPhys.75.1.

[78] Arunav Bordoloi, Valentina Zannier, Lucia Sorba, Christian Schönenberger, and Andreas Baumgartner. "A Double Quantum Dot Spin Valve." In: *Communications Physics* 3.1 (Dec. 2020), p. 135. ISSN: 2399-3650. DOI: 10.1038/s42005-020-00405-2.

[79] J. R. Petta, A. C. Johnson, J. M. Taylor, E. A. Laird, A. Yacoby, M. D. Lukin, C. M. Marcus, M. P. Hanson, and A. C. Gossard. "Coherent Manipulation of Coupled Electron Spins in Semiconductor Quantum Dots." In: *Science* 309.5744 (Sept. 2005), pp. 2180–2184. DOI: 10.1126/science.1116955.

[80] C. Barthel, M. Kjærgaard, J. Medford, M. Stopa, C. M. Marcus, M. P. Hanson, and A. C. Gossard. "Fast Sensing of Double-Dot Charge Arrangement and Spin State with a Radio-Frequency Sensor Quantum Dot." In: *Physical Review B* 81.16 (Apr. 2010), p. 161308. DOI: 10.1103/PhysRevB.81.161308.

[81] Alberto Ghirri, Samuele Cornia, and Marco Affronte. "Microwave Photon Detectors Based on Semiconducting Double Quantum Dots." In: *Sensors* 20.14 (July 2020), p. 4010. ISSN: 1424-8220. DOI: 10.3390/s20144010.

[82] G. Romero, J. J. García-Ripoll, and E. Solano. "Microwave Photon Detector in Circuit QED." In: *Physical Review Letters* 102.17 (Apr. 2009), p. 173602. DOI: 10.1103/PhysRevLett.102.173602.

[83] B. Peropadre, G. Romero, G. Johansson, C. M. Wilson, E. Solano, and J. J. García-Ripoll. "Approaching Perfect Microwave Photodetection in Circuit QED." In: *Physical Review A* 84.6 (Dec. 2011), p. 063834. DOI: 10.1103/PhysRevA.84.063834.

[84] A. Poudel, R. McDermott, and M. G. Vavilov. "Quantum Efficiency of a Microwave Photon Detector Based on a Current-Biased Josephson Junction." In: *Physical Review B* 86.17 (Nov. 2012), p. 174506. DOI: 10.1103/PhysRevB.86.174506.

[85] C. Eichler, D. Bozyigit, and A. Wallraff. "Characterizing Quantum Microwave Radiation and Its Entanglement with Superconducting Qubits Using Linear Detectors." In: *Physical Review A* 86.3 (Sept. 2012), p. 032106. DOI: 10.1103/PhysRevA.86.032106.

[86] Kazuki Koshino, Kunihiro Inomata, Tsuyoshi Yamamoto, and Yasunobu Nakamura. "Implementation of an Impedance-Matched $\ensuremath{\Lambda}$ System by Dressed-State Engineering." In: *Physical Review Letters* 111.15 (Oct. 2013), p. 153601. DOI: 10.1103/PhysRevLett.111.153601.

[87] Sankar R. Sathyamoorthy, L. Tornberg, Anton F. Kockum, Ben Q. Baragiola, Joshua Combes, C. M. Wilson, Thomas M. Stace, and G. Johansson. "Quantum Nondemolition Detection of a Propagating Microwave Photon." In: *Physical Review Letters* 112.9 (Mar. 2014), p. 093601. DOI: 10.1103/PhysRevLett.112.093601.

[88] Kazuki Koshino, Kunihiro Inomata, Zhirong Lin, Yasunobu Nakamura, and Tsuyoshi Yamamoto. "Theory of Microwave Single-Photon Detection Using an Impedance-Matched Λ System." In: *Physical Review A* 91.4 (Apr. 2015), p. 043805. ISSN: 1050-2947, 1094-1622. DOI: 10.1103/PhysRevA.91.043805.

[89] Sankar Raman Sathyamoorthy, Thomas M. Stace, and Göran Johansson. "Detecting Itinerant Single Microwave Photons." In: *Comptes Rendus Physique*. Quantum Microwaves / Micro-ondes Quantiques 17.7 (Aug. 2016), pp. 756–765. ISSN: 1631-0705. DOI: 10.1016/j.crhy.2016.07.010.

[90] Oleksandr Kyriienko and Anders S. Sørensen. "Continuous-Wave Single-Photon Transistor Based on a Superconducting Circuit." In: *Physical Review Letters* 117.14 (Sept. 2016), p. 140503. DOI: 10.1103/PhysRevLett.117.140503.

[91] Arne L. Grimsmo, Baptiste Royer, John Mark Kreikebaum, Yufeng Ye, Kevin O'Brien, Irfan Siddiqi, and Alexandre Blais. "Quantum Metamaterial for Broadband Detection of Single Microwave Photons." In: *Physical Review Applied* 15.3 (Mar. 2021), p. 034074. DOI: 10.1103/PhysRevApplied.15.034074.

[92] M. H. Devoret and J M Martinis. *Quantum Entanglement and Information Processing, Volume 79 - 1st Edition*. First. Vol. 79. Les Houches, France: Elsevier: Les Houches, 2014.

[93] D. Alesini et al. "Status of the SIMP Project: Toward the Single Microwave Photon Detection." In: *Journal of Low Temperature Physics* 199.1 (Apr. 2020), pp. 348–354. ISSN: 1573-7357. DOI: 10.1007/s10909-020-02381-x.

[94] Sébastien Gleyzes, Stefan Kuhr, Christine Guerlin, Julien Bernu, Samuel Deléglise, Ulrich Busk Hoff, Michel Brune, Jean-Michel Raimond, and Serge Haroche. "Quantum Jumps of Light Recording the Birth and Death of a Photon in a Cavity." In: *Nature* 446.7133 (Mar. 2007), pp. 297–300. ISSN: 1476-4687. DOI: 10.1038/nature05589.

[95] Giovanni P. Pepe, Roberto Cristiano, and Flavio Gatti. "Superconducting Hot Electron Bolometers and Transition Edge Sensors." In: *Digital Encyclopedia of Applied Physics*. John Wiley & Sons, Ltd, 2016, pp. 1–21. ISBN: 978-3-527-60043-4. DOI: 10.1002/3527600434.eap780.

[96] Shabir Barzanjeh, M. C. de Oliveira, and Stefano Pirandola. "Microwave Photodetection with Electro-Opto-Mechanical Systems." In: *arXiv:1410.4024 [quant-ph]* (Oct. 2014). arXiv: 1410.4024 [quant-ph].

[97] Shabir Barzanjeh, Saikat Guha, Christian Weedbrook, David Vitali, Jeffrey H. Shapiro, and Stefano Pirandola. "Microwave Quantum Illumination." In: *Physical Review Letters* 114.8 (Feb. 2015), p. 080503. DOI: 10.1103/PhysRevLett.114.080503.

[98] Keye Zhang, Francesco Bariani, Ying Dong, Weiping Zhang, and Pierre Meystre. "Proposal for an Optomechanical Microwave Sensor at the Subphoton Level." In: *Physical Review*

Letters 114.11 (Mar. 2015), p. 113601. ISSN: 0031-9007, 1079-7114. DOI: 10.1103/PhysRevLett.114.113601.

[99] Susumu Komiyama. "Single-Photon Detectors in the Terahertz Range." In: *IEEE Journal of Selected Topics in Quantum Electronics* 17.1 (Jan. 2011), pp. 54–66. ISSN: 1077-260X, 1558-4542. DOI: 10.1109/JSTQE.2010.2048893.

[100] S. Komiyama, O. Astafiev, V. Antonov, T. Kutsuwa, and H. Hirai. "A Single-Photon Detector in the Far-Infrared Range." In: *Nature* 403.6768 (Jan. 2000), pp. 405–407. ISSN: 1476-4687. DOI: 10.1038/35000166.

[101] O. Astafiev, S. Komiyama, T. Kutsuwa, V. Antonov, Y. Kawaguchi, and K. Hirakawa. "Single-Photon Detector in the Microwave Range." In: *Applied Physics Letters* 80.22 (June 2002), pp. 4250–4252. ISSN: 0003-6951. DOI: 10.1063/1.1482787.

[102] L. P. Kouwenhoven, S. Jauhar, J. Orenstein, P. L. McEuen, Y. Nagamune, J. Motohisa, and H. Sakaki. "Observation of Photon-Assisted Tunneling through a Quantum Dot." In: *Physical Review Letters* 73.25 (Dec. 1994), pp. 3443–3446. ISSN: 0031-9007. DOI: 10.1103/PhysRevLett.73.3443.

[103] R. H. Blick, R. J. Haug, D. W. van der Weide, K. von Klitzing, and K. Eberl. "Photon-assisted Tunneling through a Quantum Dot at High Microwave Frequencies." In: *Applied Physics Letters* 67.26 (Dec. 1995), pp. 3924–3926. ISSN: 0003-6951, 1077-3118. DOI: 10.1063/1.114406.

[104] J. M. Elzerman, R. Hanson, J. S. Greidanus, L. H. Willems van Beveren, S. De Franceschi, L. M. K. Vandersypen, S. Tarucha, and L. P. Kouwenhoven. "Few-Electron Quantum Dot Circuit with Integrated Charge Read Out." In: *Physical Review B* 67.16 (Apr. 2003), p. 161308. DOI: 10.1103/PhysRevB.67.161308.

[105] Ramón Aguado and Leo P Kouwenhoven. "Double Quantum Dots as Detectors of High-Frequency Quantum Noise in Mesoscopic Conductors." In: *PHYSICAL REVIEW LETTERS* 84.9 (2000), p. 4.

[106] E. Onac, F. Balestro, L. H. Willems van Beveren, U. Hartmann, Y. V. Nazarov, and L. P. Kouwenhoven. "Using a Quantum Dot as a High-Frequency Shot Noise Detector." In: *Physical Review Letters* 96.17 (May 2006), p. 176601. DOI: 10.1103/PhysRevLett.96.176601.

[107] Toshimasa Fujisawa, Toshiaki Hayashi, Ritsuya Tomita, and Yoshiro Hirayama. "Bidirectional Counting of Single Electrons." In: *Science* 312.5780 (June 2006), pp. 1634–1636. DOI: 10.1126/science.1126788.

[108] S. Gustavsson, M. Studer, R. Leturcq, T. Ihn, K. Ensslin, D. C. Driscoll, and A. C. Gossard. "Frequency-Selective Single-Photon Detection Using a Double Quantum Dot." In: *Physical Review Letters* 99.20 (Nov. 2007), p. 206804. ISSN: 0031-9007, 1079-7114. DOI: 10.1103/PhysRevLett.99.206804.

[109] R. Leturcq, S. Gustavsson, M. Studer, T. Ihn, K. Ensslin, D.C. Driscoll, and A.C. Gossard. "Frequency-Selective Single-Photon Detection with a Double Quantum Dot." In: *Physica E: Low-dimensional Systems and Nanostructures* 40.6 (Apr. 2008), pp. 1844–1847. ISSN: 13869477. DOI: 10.1016/j.physe.2007.11.032.

[110] M. Field, C. G. Smith, M. Pepper, D. A. Ritchie, J. E. F. Frost, G. A. C. Jones, and D. G. Hasko. "Measurements of Coulomb Blockade with a Noninvasive Voltage Probe." In: *Physical Review Letters* 70.9 (Mar. 1993), pp. 1311–1314. ISSN: 0031-9007. DOI: 10.1103/PhysRevLett.70.1311.

[111] D. Wallin, A. Fuhrer, L. E. Fröberg, L. Samuelson, H. Q. Xu, S. Hofling, and A. Forchel. "Detection of Charge States in Nanowire Quantum Dots Using a Quantum Point Contact." In: *Applied Physics Letters* 90.17 (Apr. 2007), p. 172112. ISSN: 0003-6951. DOI: 10.1063/1.2732829.

[112] A. P. Higginbotham, T. W. Larsen, J. Yao, H. Yan, C. M. Lieber, C. M. Marcus, and F. Kuemmeth. "Hole Spin Coherence in a Ge/Si Heterostructure Nanowire." In: *Nano Letters* 14.6 (June 2014), pp. 3582–3586. ISSN: 1530-6984. DOI: 10.1021/nl501242b.

[113] R. J. Schoelkopf. "The Radio-Frequency Single-Electron Transistor (RF-SET): A Fast and Ultrasensitive Electrometer." In: *Science* 280.5367 (May 1998), pp. 1238–1242. ISSN: 00368075, 10959203. DOI: 10.1126/science.280.5367.1238.

[114] Wei Lu, Zhongqing Ji, Loren Pfeiffer, K. W. West, and A. J. Rimberg. "Real-Time Detection of Electron Tunnelling in a Quantum Dot." In: *Nature* 423.6938 (May 2003), pp. 422–425. ISSN: 1476-4687. DOI: 10.1038/nature01642.

[115] M. C. Cassidy, A. S. Dzurak, R. G. Clark, K. D. Petersson, I. Farrer, D. A. Ritchie, and C. G. Smith. "Single Shot Charge Detection Using a Radio-Frequency Quantum Point Contact." In: *Applied Physics Letters* 91.22 (Nov. 2007), p. 222104. ISSN: 0003-6951. DOI: 10.1063/1.2809370.

[116] D. J. Reilly, C. M. Marcus, M. P. Hanson, and A. C. Gossard. "Fast Single-Charge Sensing with a Rf Quantum Point Contact." In: *Applied Physics Letters* 91.16 (Oct. 2007), p. 162101. ISSN: 0003-6951. DOI: 10.1063/1.2794995.

[117] T. Müller, B. Küng, S. Hellmüller, P. Studerus, K. Ensslin, T. Ihn, M. Reinwald, and W. Wegscheider. "An *in Situ* Tunable Radio-Frequency Quantum Point Contact." In: *Applied Physics Letters* 97.20 (Nov. 2010), p. 202104. ISSN: 0003-6951, 1077-3118. DOI: 10.1063/1.3517483.

[118] David J. Ibberson, Lisa A. Ibberson, Geoff Smithson, James A. Haigh, Sylvain Barraud, and M. Fernando Gonzalez-Zalba. "Low-Temperature Tunable Radio-Frequency Resonator for Sensitive Dispersive Readout of Nanoelectronic Devices." In: *Applied Physics Letters* 114.12 (Mar. 2019), p. 123501. ISSN: 0003-6951. DOI: 10.1063/1.5082894.

[119] M. Jung, M. D. Schroer, K. D. Petersson, and J. R. Petta. "Radio Frequency Charge Sensing in InAs Nanowire Double Quantum Dots." In: *Applied Physics Letters* 100.25 (June 2012), p. 253508. ISSN: 0003-6951, 1077-3118. DOI: 10.1063/1.4729469.

[120] M. D. Schroer, M. Jung, K. D. Petersson, and J. R. Petta. "Radio Frequency Charge Parity Meter." In: *Physical Review Letters* 109.16 (Oct. 2012), p. 166804. DOI: 10.1103/PhysRevLett.109.166804.

[121] Deividas Sabonis, Eoin C. T. O'Farrell, Davydas Razmadze, David M. T. van Zanten, Judith Suter, Peter Krogstrup, and Charles M. Marcus. "Dispersive Sensing in Hybrid InAs/Al Nanowires." In: *Applied Physics Letters* 115.10 (Sept. 2019), p. 102601. ISSN: 0003-6951, 1077-3118. DOI: 10.1063/1.5116377. arXiv: 1906.10659.

[122] N. Ares et al. "Sensitive Radio-Frequency Measurements of a Quantum Dot by Tuning to Perfect Impedance Matching." In: *Physical Review Applied* 5.3 (Mar. 2016), p. 034011. DOI: 10.1103/PhysRevApplied.5.034011.

[123] Akito Noiri, Kenta Takeda, Jun Yoneda, Takashi Nakajima, Tetsuo Kodera, and Seigo Tarucha. "Radio-Frequency-Detected Fast Charge Sensing in Undoped Silicon Quantum Dots." In: *Nano Letters* 20.2 (Feb. 2020), pp. 947–952. ISSN: 1530-6984. DOI: 10.1021/acs.nanolett.9b03847.

[124] T. Duty, G. Johansson, K. Bladh, D. Gunnarsson, C. Wilson, and P. Delsing. "Observation of Quantum Capacitance in the Cooper-Pair Transistor." In: *Physical Review Letters* 95.20 (Nov. 2005), p. 206807. DOI: 10.1103/PhysRevLett.95.206807.

[125] V. Ranjan, G. Puebla-Hellmann, M. Jung, T. Hasler, A. Nunnenkamp, M. Muoth, C. Hierold, A. Wallraff, and C. Schönenberger. "Clean Carbon Nanotubes Coupled to Superconducting Impedance-Matching Circuits." In: *Nature Communications* 6.1 (May 2015), p. 7165. ISSN: 2041-1723. DOI: 10.1038/ncomms8165.

[126] Imtiaz Ahmed et al. "Radio-Frequency Capacitive Gate-Based Sensing." In: *Physical Review Applied* 10.1 (July 2018), p. 014018. ISSN: 2331-7019. DOI: 10.1103/PhysRevApplied.10.014018. arXiv: 1801.09759.

[127] Damaz de Jong, Jasper van Veen, Luca Binci, Amrita Singh, Peter Krogstrup, Leo P. Kouwenhoven, Wolfgang Pfaff, and John D. Watson. "Rapid Detection of Coherent Tunneling in an In As Nanowire Quantum Dot through Dispersive Gate Sensing." In: *Physical Review Applied* 11.4 (Apr. 2019), p. 044061. ISSN: 2331-7019. DOI: 10.1103/PhysRevApplied.11.044061.

[128] R. Mizuta, R. M. Otxoa, A. C. Betz, and M. F. Gonzalez-Zalba. "Quantum and Tunneling Capacitance in Charge and Spin Qubits." In: *Physical Review B* 95.4 (Jan. 2017), p. 045414. ISSN: 2469-9950, 2469-9969. DOI: 10.1103/PhysRevB.95.045414.

[129] Anderson West et al. "Gate-Based Single-Shot Readout of Spins in Silicon." In: *Nature Nanotechnology* 14.5 (May 2019), pp. 437–441. ISSN: 1748-3387, 1748-3395. DOI: 10.1038/s41565-019-0400-7.

[130] K. D. Petersson, L. W. McFaul, M. D. Schroer, M. Jung, J. M. Taylor, A. A. Houck, and J. R. Petta. "Circuit Quantum Electrodynamics with a Spin Qubit." In: *Nature* 490.7420 (Oct. 2012), pp. 380–383. ISSN: 0028-0836, 1476-4687. DOI: 10.1038/nature11559.

[131] T. Frey, P. J. Leek, M. Beck, A. Blais, T. Ihn, K. Ensslin, and A. Wallraff. "Dipole Coupling of a Double Quantum Dot to a Microwave Resonator." In: *Physical Review Letters* 108.4 (Jan. 2012), p. 046807. ISSN: 0031-9007, 1079-7114. DOI: 10.1103/PhysRevLett.108.046807.

[132] P. Scarlino et al. "All-Microwave Control and Dispersive Readout of Gate-Defined Quantum Dot Qubits in Circuit Quantum Electrodynamics." In: *Physical Review Letters* 122.20 (May 2019), p. 206802. ISSN: 0031-9007, 1079-7114. DOI: 10.1103/PhysRevLett.122.206802.

[133] A. J. Landig, J. V. Koski, P. Scarlino, U. C. Mendes, A. Blais, C. Reichl, W. Wegscheider, A. Wallraff, K. Ensslin, and T. Ihn. "Coherent Spin–Photon Coupling Using a Resonant Exchange Qubit." In: *Nature* 560.7717 (Aug. 2018), pp. 179–184. ISSN: 0028-0836, 1476-4687. DOI: 10.1038/s41586-018-0365-y.

[134] A. Pfund, I. Shorubalko, R. Leturcq, and K. Ensslin. "Top-Gate Defined Double Quantum Dots in InAs Nanowires." In: *Applied Physics Letters* 89.25 (Dec. 2006), p. 252106. ISSN: 0003-6951, 1077-3118. DOI: 10.1063/1.2409625.

[135] Malin Nilsson, I-Ju Chen, Sebastian Lehmann, Vendula Maulerova, Kimberly A. Dick, and Claes Thelander. "Parallel-Coupled Quantum Dots in InAs Nanowires." In: *Nano Letters* 17.12 (Dec. 2017), pp. 7847–7852. ISSN: 1530-6984, 1530-6992. DOI: 10.1021/acs.nanolett.7b04090.

[136] K. Wang, C. Payette, Y. Dovzhenko, P. W. Deelman, and J. R. Petta. "Charge Relaxation in a Single-Electron $\mathrm{Si}/\mathrm{SiGe}$ Double Quantum Dot." In: *Physical Review Letters* 111.4 (July 2013), p. 046801. DOI: 10.1103/PhysRevLett.111.046801.

[137] Toshimasa Fujisawa, Tjerk H. Oosterkamp, Wilfred G. van der Wiel, Benno W. Broer, Ramón Aguado, Seigo Tarucha, and Leo P. Kouwenhoven. "Spontaneous Emission Spectrum in Double Quantum Dot Devices." In: *Science* 282.5390 (Oct. 1998), pp. 932–935. DOI: 10.1126/science.282.5390.932.

[138] C. Weber, A. Fuhrer, C. Fasth, G. Lindwall, L. Samuelson, and A. Wacker. "Probing Confined Phonon Modes by Transport through a Nanowire Double Quantum Dot." In: *Physical Review Letters* 104.3 (Jan. 2010), p. 036801. DOI: 10.1103/PhysRevLett.104.036801.

[139] P. Roulleau, S. Baer, T. Choi, F. Molitor, J. Güttinger, T. Müller, S. Dröscher, K. Ensslin, and T. Ihn. "Coherent Electron–Phonon Coupling in Tailored Quantum Systems." In: *Nature Communications* 2.1 (Mar. 2011), p. 239. ISSN: 2041-1723. DOI: 10.1038/ncomms1241.

[140] Guido Burkard, Michael J. Gullans, Xiao Mi, and Jason R. Petta. "Superconductor–Semiconductor Hybrid-Circuit Quantum Electrodynamics." In: *Nature Reviews Physics* 2.3 (Mar. 2020), pp. 129–140. ISSN: 2522-5820. DOI: 10.1038/s42254-019-0135-2.

[141] A. Wallraff, D. I. Schuster, A. Blais, L. Frunzio, R.-S. Huang, J. Majer, S. Kumar, S. M. Girvin, and R. J. Schoelkopf. "Strong Coupling of a Single Photon to a Superconducting Qubit Using Circuit Quantum Electrodynamics." In: *Nature* 431.7005 (Sept. 2004), pp. 162–167. ISSN: 0028-0836, 1476-4687. DOI: 10.1038/nature02851.

[142] A. Megrant et al. "Planar Superconducting Resonators with Internal Quality Factors above One Million." In: *Applied Physics Letters* 100.11 (Mar. 2012), p. 113510. ISSN: 0003-6951, 1077-3118. DOI: 10.1063/1.3693409.

[143] C. M. Quintana et al. "Characterization and Reduction of Microfabrication-Induced Decoherence in Superconducting Quantum Circuits." In: *Applied Physics Letters* 105.6 (Aug. 2014), p. 062601. ISSN: 0003-6951, 1077-3118. DOI: 10.1063/1.4893297.

[144] M. Göppl, A. Fragner, M. Baur, R. Bianchetti, S. Filipp, J. M. Fink, P. J. Leek, G. Puebla, L. Steffen, and A. Wallraff. "Coplanar Waveguide Resonators for Circuit Quantum Electrodynamics." In: *Journal of Applied Physics* 104.11 (Dec. 2008), p. 113904. ISSN: 0021-8979, 1089-7550. DOI: 10.1063/1.3010859.

[145] X. Mi, J. V. Cady, D. M. Zajac, J. Stehlik, L. F. Edge, and J. R. Petta. "Circuit Quantum Electrodynamics Architecture for Gate-Defined Quantum Dots in Silicon." In: *Applied Physics Letters* 110.4 (Jan. 2017), p. 043502. ISSN: 0003-6951, 1077-3118. DOI: 10.1063/1.4974536.

[146] N. Samkharadze, A. Bruno, P. Scarlino, G. Zheng, D. P. DiVincenzo, L. DiCarlo, and L. M. K. Vandersypen. "High-Kinetic-Inductance Superconducting Nanowire Resonators for Circuit QED in a Magnetic Field." In: *Physical Review Applied* 5.4 (Apr. 2016), p. 044004. ISSN: 2331-7019. DOI: 10.1103/PhysRevApplied.5.044004.

[147] Yasuhiro Tokura, Wilfred G. van der Wiel, Toshiaki Obata, and Seigo Tarucha. "Coherent Single Electron Spin Control in a Slanting Zeeman Field." In: *Physical Review Letters* 96.4 (Jan. 2006), p. 047202. DOI: 10.1103/PhysRevLett.96.047202.

[148] J. J. Viennot, M. C. Dartiailh, A. Cottet, and T. Kontos. "Coherent Coupling of a Single Spin to Microwave Cavity Photons." In: *Science* 349.6246 (July 2015), pp. 408–411. DOI: 10.1126/science.aaa3786.

[149] J. J. Viennot, M. R. Delbecq, M. C. Dartiailh, A. Cottet, and T. Kontos. "Out-of-Equilibrium Charge Dynamics in a Hybrid Circuit Quantum Electrodynamics Architecture." In: *Physical Review B* 89.16 (Apr. 2014), p. 165404. DOI: 10.1103/PhysRevB.89.165404.

[150] Guang-Wei Deng et al. "Charge Number Dependence of the Dephasing Rates of a Graphene Double Quantum Dot in a Circuit QED Architecture." In: *Physical Review Letters* 115.12 (Sept. 2015), p. 126804. DOI: 10.1103/PhysRevLett.115.126804.

[151] A. Stockklauser, V. F. Maisi, J. Basset, K. Cujia, C. Reichl, W. Wegscheider, T. Ihn, A. Wallraff, and K. Ensslin. "Microwave Emission from Hybridized States in a Semiconductor Charge Qubit." In: *Physical Review Letters* 115.4 (July 2015), p. 046802. DOI: 10.1103/PhysRevLett.115.046802.

[152] R. Wang, R. S. Deacon, D. Car, E. P. A. M. Bakkers, and K. Ishibashi. "InSb Nanowire Double Quantum Dots Coupled to a Superconducting Microwave Cavity." In: *Applied Physics Letters* 108.20 (May 2016), p. 203502. ISSN: 0003-6951, 1077-3118. DOI: 10.1063/1.4950764.

[153] T. Hayashi, T. Fujisawa, H. D. Cheong, Y. H. Jeong, and Y. Hirayama. "Coherent Manipulation of Electronic States in a Double Quantum Dot." In: *Physical Review Letters* 91.22 (Nov. 2003), p. 226804. DOI: 10.1103/PhysRevLett.91.226804.

[154] K. D. Petersson, J. R. Petta, H. Lu, and A. C. Gossard. "Quantum Coherence in a One-Electron Semiconductor Charge Qubit." In: *Physical Review Letters* 105.24 (Dec. 2010), p. 246804. DOI: 10.1103/PhysRevLett.105.246804.

[155] E. Paladino, Y. M. Galperin, G. Falci, and B. L. Altshuler. "$\mathbsf{1}/\mathbsfit{f}$ Noise: Implications for Solid-State Quantum Information." In: *Reviews of Modern Physics* 86.2 (Apr. 2014), pp. 361–418. DOI: 10.1103/RevModPhys.86.361.

[156] J. Q. You, Xuedong Hu, and Franco Nori. "Correlation-Induced Suppression of Decoherence in Capacitively Coupled Cooper-pair Boxes." In: *Physical Review B* 72.14 (Oct. 2005), p. 144529. DOI: 10.1103/PhysRevB.72.144529.

[157] Waqar Khan, Patrick P. Potts, Sebastian Lehmann, Claes Thelander, Kimberly A. Dick, Peter Samuelsson, and Ville F. Maisi. "Efficient and Continuous Microwave Photoconversion in Hybrid Cavity-Semiconductor Nanowire Double Quantum Dot Diodes." In: *Nature Communications* 12.1 (Dec. 2021), p. 5130. ISSN: 2041-1723. DOI: 10.1038/s41467-021-25446-1.

[158] M Schöndorf, L C G Govia, M G Vavilov, R McDermott, and F K Wilhelm. "Optimizing Microwave Photodetection: Input–Output Theory." In: *Quantum Science and Technology* 3.2 (Apr. 2018), p. 024009. ISSN: 2058-9565. DOI: 10.1088/2058-9565/aaa7f7.

[159] Perrin Walker and William H. Tarn, eds. *CRC Handbook of Metal Etchants*. Boca Raton: CRC Press, 1991. ISBN: 978-0-8493-3623-2.

[160] Zhuoxing Luo and A Dissertation. "RF PLASMA ETCHING WITH A DC BIAS." In: (), p. 135.

[161] C. Hedlund, H.-O. Blom, and S. Berg. "Microloading Effect in Reactive Ion Etching." In: *Journal of Vacuum Science & Technology A: Vacuum, Surfaces, and Films* 12.4 (July 1994), pp. 1962–1965. ISSN: 0734-2101, 1520-8559. DOI: 10.1116/1.578990.

[162] Nasim Mahmoodi, Abduljabbar I. Rushdi, James Bowen, Aydin Sabouri, Carl J. Anthony, Paula M. Mendes, and Jon A. Preece. "Room Temperature Thermally Evaporated Thin Au Film on Si Suitable for Application of Thiol Self-Assembled Monolayers in Micro/Nano-Electro-Mechanical-Systems Sensors." In: *Journal of Vacuum Science & Technology A: Vacuum, Surfaces, and Films* 35.4 (July 2017), p. 041514. ISSN: 0734-2101, 1520-8559. DOI: 10.1116/1.4990026.

[163] Wenchuang (Walter) Hu, Koshala Sarveswaran, Marya Lieberman, and Gary H. Bernstein. "Sub-10 Nm Electron Beam Lithography Using Cold Development of Poly(Methylmethacrylate)." In: *Journal of Vacuum Science & Technology B: Microelectronics and Nanometer Structures* 22.4 (2004), p. 1711. ISSN: 0734211X. DOI: 10.1116/1.1763897.

[164] Akio Misaka, Kenji Harafuji, and Noboru Nomura. "Determination of Proximity Effect Parameters in Electron-beam Lithography." In: *Journal of Applied Physics* 68.12 (Dec. 1990), pp. 6472–6479. ISSN: 0021-8979, 1089-7550. DOI: 10.1063/1.346846.

[165] T. H. P. Chang. "Proximity Effect in Electron-beam Lithography." In: *Journal of Vacuum Science and Technology* 12.6 (Nov. 1975), pp. 1271–1275. ISSN: 0022-5355. DOI: 10.1116/1.568515.

[166] M. Hauptmann, K.-H. Choi, P. Jaschinsky, C. Hohle, J. Kretz, and L.M. Eng. "Determination of Proximity Effect Parameters by Means of CD-linearity in Sub 100nm Electron Beam Lithography." In: *Microelectronic Engineering* 86.4-6 (Apr. 2009), pp. 539–543. ISSN: 01679317. DOI: 10.1016/j.mee.2008.12.053.

[167] D. F. Kyser and N. S. Viswanathan. "Monte Carlo Simulation of Spatially Distributed Beams in Electron-beam Lithography." In: *Journal of Vacuum Science and Technology* 12.6 (Nov. 1975), pp. 1305–1308. ISSN: 0022-5355. DOI: 10.1116/1.568524.

[168] Kilian Flöhr et al. "Manipulating InAs Nanowires with Submicrometer Precision." In: *Review of Scientific Instruments* 82.11 (Nov. 2011), p. 113705. ISSN: 0034-6748, 1089-7623. DOI: 10.1063/1.3657135.

[169] D B Suyatin, C Thelander, M T Björk, I Maximov, and L Samuelson. "Sulfur Passivation for Ohmic Contact Formation to InAs Nanowires." In: *Nanotechnology* 18.10 (Mar. 2007), p. 105307. ISSN: 0957-4484, 1361-6528. DOI: 10.1088/0957-4484/18/10/105307.

[170] A. Ghirri, C. Bonizzoni, D. Gerace, S. Sanna, A. Cassinese, and M. Affronte. "YBa2CuO7 Microwave Resonators for Strong Collective Coupling with Spin Ensembles." In: *Applied Physics Letters* 106.18 (May 2015), p. 184101. ISSN: 0003-6951, 1077-3118. DOI: 10.1063/1.4920930.

[171] *QCoDeS/Qcodes*. QCoDeS. June 2022.

[172] Olaf Wunnicke. "Gate Capacitance of Back-Gated Nanowire Field-Effect Transistors." In: *Applied Physics Letters* 89.8 (Aug. 2006), p. 083102. ISSN: 0003-6951, 1077-3118. DOI: 10.1063/1.2337853.

[173] Changyong Lan, SenPo Yip, Xiaolin Kang, You Meng, Xiuming Bu, and Johnny C. Ho. "Gate Bias Stress Instability and Hysteresis Characteristics of InAs Nanowire Field-Effect Transistors." In: *ACS Applied Materials & Interfaces* 12.50 (Dec. 2020), pp. 56330–56337. ISSN: 1944-8244, 1944-8252. DOI: 10.1021/acsami.0c17317.

[174] M Rinzan, G Jenkins, H D Drew, S Shafranjuk, and P Barbara. "Carbon Nanotube Quantum Dots As Highly Sensitive Terahertz- Cooled Spectrometers." In: *Nano Lett.* (2012), p. 4.

[175] Hehai Fang and Weida Hu. "Photogating in Low Dimensional Photodetectors." In: *Advanced Science* 4.12 (2017), p. 1700323. ISSN: 2198-3844. DOI: 10.1002/advs.201700323.

[176] Gregory Auton et al. "Terahertz Detection and Imaging Using Graphene Ballistic Rectifiers." In: *Nano Lett.* (2017), p. 6.

[177] H van Houten, C W J Beenakker, and A A M Staring. "Coulomb-Blockade Oscillations in Semiconductor Nanostructures." In: (), p. 28.

[178] Jeremy M. Sage, Vladimir Bolkhovsky, William D. Oliver, Benjamin Turek, and Paul B. Welander. "Study of Loss in Superconducting Coplanar Waveguide Resonators." In: *Journal of Applied Physics* 109.6 (Mar. 2011), p. 063915. ISSN: 0021-8979, 1089-7550. DOI: 10.1063/1.3552890.

[179] M. J. Lancaster. *Passive Microwave Device Applications of High-Temperature Superconductors*. Cambridge: Cambridge University Press, 1997. ISBN: 978-0-521-03417-3. DOI: 10.1017/CBO9780511526688.

[180] Francesco Rossella, Vincenzo Piazza, Mirko Rocci, Daniele Ercolani, Lucia Sorba, Fabio Beltram, and Stefano Roddaro. "GHz Electroluminescence Modulation in Nanoscale Subwavelength Emitters." In: *Nano Letters* 16.9 (Sept. 2016), pp. 5521–5527. ISSN: 1530-6984, 1530-6992. DOI: 10.1021/acs.nanolett.6b02020.

[181] Y.-Y. Liu, J. Stehlik, C. Eichler, M. J. Gullans, J. M. Taylor, and J. R. Petta. "Semiconductor Double Quantum Dot Micromaser." In: *Science* 347.6219 (Jan. 2015), pp. 285–287. ISSN: 0036-8075, 1095-9203. DOI: 10.1126/science.aaa2501.

[182] Tsuyoshi Takahashi, Kenichi Kawaguchi, Masaru Sato, Michihiko Suhara, and Naoya Okamoto. "Improved Microwave Sensitivity to 706 kV/W by Using *p* -GaAsSb/ *n* -InAs Nanowire Backward Diodes for Low-Power Energy Harvesting at Zero Bias." In: *AIP Advances* 10.8 (Aug. 2020), p. 085218. ISSN: 2158-3226. DOI: 10.1063/5.0006061.

[183] Erik Lind. "High Frequency III–V Nanowire MOSFETs." In: *Semiconductor Science and Technology* 31.9 (Sept. 2016), p. 093005. ISSN: 0268-1242, 1361-6641. DOI: 10.1088/0268-1242/31/9/093005.

[184] L P Kouwenhoven, D G Austing, and S Tarucha. "Few-Electron Quantum Dots." In: *Reports on Progress in Physics* 64.6 (June 2001), pp. 701–736. ISSN: 0034-4885, 1361-6633. DOI: 10.1088/0034-4885/64/6/201.

[185] T. R. Hartke, Y.-Y. Liu, M. J. Gullans, and J. R. Petta. "Microwave Detection of Electron-Phonon Interactions in a Cavity-Coupled Double Quantum Dot." In: *Physical Review Letters* 120.9 (Feb. 2018), p. 097701. ISSN: 0031-9007, 1079-7114. DOI: 10.1103/PhysRevLett.120.097701.

[186] Damaz de Jong, Christian G. Prosko, Daan M. A. Waardenburg, Lin Han, Filip K. Malinowski, Peter Krogstrup, Leo P. Kouwenhoven, Jonne V. Koski, and Wolfgang Pfaff. "Rapid Microwave-Only Characterization and Readout of Quantum Dots Using Multiplexed Gigahertz-Frequency Resonators." In: *Physical Review Applied* 16.1 (July 2021), p. 014007. ISSN: 2331-7019. DOI: 10.1103/PhysRevApplied.16.014007.

[187] Y.-Y. Liu, K. D. Petersson, J. Stehlik, J. M. Taylor, and J. R. Petta. "Photon Emission from a Cavity-Coupled Double Quantum Dot." In: *Physical Review Letters* 113.3 (July 2014), p. 036801. ISSN: 0031-9007, 1079-7114. DOI: 10.1103/PhysRevLett.113.036801. arXiv: 1401.7730.

[188] Valentina Zannier, Francesca Rossi, Daniele Ercolani, and Lucia Sorba. "Growth Dynamics of InAs/InP Nanowire Heterostructures by Au-assisted Chemical Beam Epitaxy." In: *Nanotechnology* 30.9 (Mar. 2019), p. 094003. ISSN: 0957-4484, 1361-6528. DOI: 10.1088/1361-6528/aaf7ab.

[189] Frederick S Thomas, Andreas Baumgartner, Lukas Gubser, Christian Jünger, Gergő Fülöp, Malin Nilsson, Francesca Rossi, Valentina Zannier, Lucia Sorba, and Christian Schönenberger. "Highly Symmetric and Tunable Tunnel Couplings in InAs/InP Nanowire Heterostructure Quantum Dots." In: *Nanotechnology* 31.13 (Mar. 2020), p. 135003. ISSN: 0957-4484, 1361-6528. DOI: 10.1088/1361-6528/ab5ce6.

[190] D. Barker, S. Lehmann, L. Namazi, M. Nilsson, C. Thelander, K. A. Dick, and V. F. Maisi. "Individually Addressable Double Quantum Dots Formed with Nanowire Polytypes and Identified by Epitaxial Markers." In: *Applied Physics Letters* 114.18 (May 2019), p. 183502. ISSN: 0003-6951, 1077-3118. DOI: 10.1063/1.5089275.

[191] *Detectors: Figures of Merit*. CRC Press, Sept. 2015, pp. 1–9. ISBN: 978-1-351-24718-4. DOI: 10.1081/E-EOE2-120009723.

[192] H Thierschmann, M Henke, J Knorr, L Maier, C Heyn, W Hansen, H Buhmann, and L W Molenkamp. "Diffusion Thermopower of a Serial Double Quantum Dot." In: *New Journal of Physics* 15.12 (Dec. 2013), p. 123010. ISSN: 1367-2630. DOI: 10.1088/1367-2630/15/12/123010.

[193] A. Pfund, I. Shorubalko, K. Ensslin, and R. Leturcq. "Suppression of Spin Relaxation in an InAs Nanowire Double Quantum Dot." In: *Physical Review Letters* 99.3 (July 2007), p. 036801. ISSN: 0031-9007, 1079-7114. DOI: 10.1103/PhysRevLett.99.036801.

[194] Dan Zhang and Gan Yang. "Recent Progress on Critical Cleaning of Sapphire Single-Crystal Substrates: A Mini-Review." In: *Recent Patents on Chemical Engineering* 6.3 (2013), pp. 161–166. ISSN: 211-3347/1874-4788. DOI: 10.2174/22113347079991403311217 52.

[195] Malin Nilsson. "Charge and Spin Transport in Parallel-Coupled Quantum Dots in Nanowires." PhD thesis. Lund University, 2018.

[196] Abderrezak Belabbes, Christian Panse, Jürgen Furthmüller, and Friedhelm Bechstedt. "Electronic Bands of III-V Semiconductor Polytypes and Their Alignment." In: *Physical Review B* 86.7 (Aug. 2012), p. 075208. ISSN: 1098-0121, 1550-235X. DOI: 10.1103/PhysRevB.86.075208.

[197] Z. Zanolli, F. Fuchs, J. Furthmüller, U. von Barth, and F. Bechstedt. "Model GW Band Structure of InAs and GaAs in the Wurtzite Phase." In: *Physical Review B* 75.24 (June 2007), p. 245121. ISSN: 1098-0121, 1550-235X. DOI: 10.1103/PhysRevB.75.245121.

[198] H. Potts, I.–J. Chen, A. Tsintzis, M. Nilsson, S. Lehmann, K. A. Dick, M. Leijnse, and C. Thelander. "Electrical Control of Spins and Giant G-Factors in Ring-like Coupled Quantum Dots." In: *Nature Communications* 10.1 (Dec. 2019), p. 5740. ISSN: 2041-1723. DOI: 10.1038/s41467-019-13583-7.

[199] Christian Jünger, Andreas Baumgartner, Raphaëlle Delagrange, Denis Chevallier, Sebastian Lehmann, Malin Nilsson, Kimberly A. Dick, Claes Thelander, and Christian Schönenberger. "Spectroscopy of the Superconducting Proximity Effect in Nanowires Using Integrated Quantum Dots." In: *Communications Physics* 2.1 (Dec. 2019), p. 76. ISSN: 2399-3650. DOI: 10.1038/s42005-019-0162-4.

[200] Andrey V. Kretinin, Ronit Popovitz-Biro, Diana Mahalu, and Hadas Shtrikman. "Multimode Fabry-Pérot Conductance Oscillations in Suspended Stacking-Faults-Free InAs Nanowires." In: *Nano Letters* 10.9 (Sept. 2010), pp. 3439–3445. ISSN: 1530-6984, 1530-6992. DOI: 10.1021/nl101522j.

[201] Andrey V. Kretinin, Hadas Shtrikman, David Goldhaber-Gordon, Markus Hanl, Andreas Weichselbaum, Jan von Delft, Theo Costi, and Diana Mahalu. "Spin- 1 2 Kondo Effect in an InAs Nanowire Quantum Dot: Unitary Limit, Conductance Scaling, and Zeeman Splitting." In: *Physical Review B* 84.24 (Dec. 2011), p. 245316. ISSN: 1098-0121, 1550-235X. DOI: 10.1103/PhysRevB.84.245316.

[202] S. Baba, S. Matsuo, H. Kamata, R. S. Deacon, A. Oiwa, K. Li, S. Jeppesen, L. Samuelson, H. Q. Xu, and S. Tarucha. "Gate Tunable Parallel Double Quantum Dots in InAs Double-Nanowire Devices." In: *Applied Physics Letters* 111.23 (Dec. 2017), p. 233513. ISSN: 0003-6951, 1077-3118. DOI: 10.1063/1.4997646.